STRUCTURED LASER WAVEFRONTS FOR RAMAN SPECTROSCOPY AND SINGLE MOLECULE SPECTROSCOPY

A Dissertation

by

MARIIA SHUTOVA

Submitted to the Office of Graduate and Professional Studies of
Texas A&M University
in partial fulfillment of the requirements for the degree of

DOCTOR OF PHILOSOPHY

Chair of Committee,	Alexei V. Sokolov
Committee Members,	Marlan O. Scully
	Olga Kocharovskaya
	Philip Hemmer
Head of Department,	Grigory Rogachev

August 2020

Major Subject: Physics

ABSTRACT

Wavefront shaping is a powerful technique that revolutionized many aspects of our lives. It allowed us to see farther galaxies and smaller objects better than ever. It drastically changed the field of optics in general and imaging in particular, providing the possibility to focus light through highly scattering media and restore a light beam profile after major distortions. Automatization of wavefront shaping with adaptive algorithms sped up the process and added the flexibility of changing beam wavefront parameters “on the go”. At the same time, with the advancement of nanotechnologies we gain a privilege to study how macroscopic changes in a laser beam shape affect single atoms on the nanoscale.

Our research focuses on extending the applications of laser wavefront shaping in the area of linear and nonlinear optics, spectroscopy, imaging and light-matter interactions. We aim to push limits of existing spectroscopic techniques (e.g. Raman spectroscopy) and develop fundamentally new applications for shaped laser beams. Optical vortices - structured light modes - are another type of shaped beams, rapidly gaining popularity and being used, for example, for encoding quantum information onto the light beam. The studies on how optical vortex modes pass their quantum properties (such as orbital angular momentum) to a single molecule or an atom, is an intriguing question that is still underexplored. Moreover, left- or right-handedness of an optical vortex makes it an efficient tool for studying molecular chirality on a single-molecule scale. Experiments in this field are highly multidisciplinary and require the combination of robust chemical sample preparation, precise optical alignment and manufacturing of complex nanostructures. In this dissertation we gather all the necessary technologies and procedures, conduct optical simulations and build the experimental setup that allows us to probe the chirality or the dipole-forbidden transition of a single molecule with the help of shaped laser beams and nanostructures.

DEDICATION

To my Mom, who believes in me.

To my Dad, who was always proud of me.

To my sister, who shows that everything in the world is possible.

And, of course, to Anton, who makes my life reach, meaningful and purposeful.

ACKNOWLEDGMENTS

I would like to express my deepest appreciation to my scientific advisor Prof. Alexei Sokolov, who introduced me to the world of experimental optics and who lead and supported me through the years in graduate school. I would like to extend my sincere thanks to my dissertation committee members - Olga Kocharovskaya, Marlan O. Scully and Philip Hemmer - for the valuable guidance along my Ph.D. career.

The completion of my dissertation would not have been possible without the experience, knowledge and leadership of Alexander Goltsov, Alexander Sinyukov, Alexandra Zhdanova, Alexei Belyanin, Grigory Rogachev, Rafael Quintero-Torres, Volker Deckert, Zhenrong Zhang, Jonathan Hu, Suhail Zubairy, Valery Pokrovsky, Robert Nevels, Jonathan Thompson, Rick Trebino, Anatoli Morozov, Narangerel Altangerel, Zehua Han, Zhe He, Zack Liege, Blake Birmingham, Kim Chapin, Veronica Rodriguez, Heather Walker, RaéChel Superville.

I'm extremely grateful to Tatiana Erukhimova, who provided me with encouragement and support throughout my Ph.D. journey. Tatiana together with Dawson Nodurft and John Mason were the ones, who taught me that it is not enough to know Physics until you can teach it to somebody else.

I cannot be thankful enough to Aleksandr Fedorov, Yuri Temis, Yuri Shvyd'ko and Natasha Shvydko for the encouragement in pursuing Ph.D. degree at Texas A&M graduate school.

Special thanks to Hanna Hlushko and Chelsea Ebert for patiently doing a vast job proofreading this manuscript. ALso, I'd like to recognize the assistance I received from Mrunal Kamble when writing this dissertation.

I would like to extend my sincere thanks to Mariya Khmelenko, Anton Classen, Ricardo Gutierrez-Jauregui, Patrick McColgan, Gavriil Shchedrin for being equally wonderful as both friends and colleagues.

I would like to extend my deepest gratitude to my dearest friends Varvara Andreevna Kirienko, Elena Vakhitova & Cyprien Karolak, Artyom Golyzhbin & Vika Kumyzarova, Nikol Galiakberova

& Vera & Marika Osborne, Marianna Tanska & Oleks Tanski, Ira Shatruk, Raman Hlushko, Anastasiia Alikimovich, Nataliia Sviazinska, Eugene Lykhovyd, Mauricio Martignon, who make my life joyful and provide constant emotional support.

Last, but not least, I am deeply indebted to my family: Nina Elfimova, Natalia, Alexei, Arina, Vanya, Misha, Ilya Rogoznikov, Alla, Alexei & Alexei Jr. Pulkin and Svetlana Kozlova for all their love and support. I am greatful to my dearest husband Anton Shutov, whose endless patience and help on each aspect of this dissertation cannot be overestimated; and whose love and support made me believe in myself.

CONTRIBUTORS AND FUNDING SOURCES

Contributors

This work was supported by a dissertation committee consisting of Professors Alexei V. Sokolov, Marlan O. Scully, and Olga Kocharovskaya of the Department of Physics and Astronomy, Texas A&M University and Professor Philip Hemmer of the Department of Electrical Engineering, Texas A&M University.

The data analyzed for Chapter 8, Section 8.2, Fig. 8.12 was provided by Professor Jonathan Hu of the Department of Electrical Engineering, Baylor University and Wei Zhang, Baylor University. The data analyzed for Chapter 6, Section 6.3 was provided by Zack Liege and Dr. Alexander Goltsov of the Department of Physics, Baylor University.

The data analyzed in Chapter 8, Section 8.1.1 was provided by Professor Rafael Quintero-Torres, Department of Nanotechnologies, National Autonomous University of Mexico.

The data analyzed in Chapter 8 Section 8.3, Fig. 8.16 was provided by Volker Deckert, Friedrich Schiller University Jena.

All other work conducted for the dissertation was completed by the student independently.

Funding Sources

Graduate study was supported by the Herman F. Heep and Minnie Belle Heep Texas A&M University Endowed Fund held/administered by the Texas A&M Foundation in 2014-2017; "T3: Triads for transformation", Texas A&M University in 2019; the College of Science Strategic Transformative Research Program FY18B, Texas A&M University in 2018; and Welch Foundation (A-1547).

NOMENCLATURE

OV	Optical Vortex
TC	Topological Charge
OAM	Orbital Angular Momentum
SAM	Spin Angular Momentum
FROG	Frequency Resolved Optical Gating
LCOS SLM	Liquid Crystal on Silicon Spatial Light Modulator
FWHM	Full Width Half Maximum
BBO	Beta Barium Borate
CuPc	Copper(II) Phthalocyanine
$PbWO_4$	Lead Tungstate
BS	Beam Splitter
HWP	Half-wave Plate
QWP	Quarter-wave Plate
CGH	Computer-generated Hologram
SRS	Stimulated Raman Scattering
FWM	Four-wave Mixing

TABLE OF CONTENTS

Page

LIST OF FIGURES

FIGURE Page

LIST OF TABLES

1. INTRODUCTION AND LITERATURE REVIEW

After the adaptive wavefront shaping techniques were invented, they quickly became popular among astronomers, for their exceptional ability to improve image quality by reducing the distortion and deterioration caused by turbulent atmosphere layers [1]. The first successful tests of adaptive optics systems were carried out in 1989 by a group of Merkle *et al.* [2]. The main reason for these approach's popularity is the invention of digital micromirror devices (DMDs), which were constructed by Dr. Larry Hornbeck in 1987, as an evolution of a deformable mirror, and liquid crystal spatial light modulators (SLMs)[3]. Both devices have many degrees of freedom (pixels) with small pixel size to ensure high quality wavefront correction. In addition, DMD has a high speed response ($\sim$ 100 MHz), which is enough to control the image in real time in a feedback loop.

Image distortion and aberrations caused huge problems not only in astronomy, but in other fields too. Microscopy field adopted the adaptive shaping techniques quickly, although the reasons behind the aberrations in microscopy are different: the difference in the indices of refraction, complex structure of the sample, and defects in optical components matter much more than turbulent air. Wavefront correction algorithms have solved these problems and improved the resolution and contrast of microscopic images [4].

Along with optical microscopes and telescopes, wavefront correction has become popular to use for shaping laser beam wavefront [5, 6]. In 2007, Vellekoop and Mosk invented a new way for adaptive laser wavefront shaping [7], that allows laser light to focus into a small spot after a laser beam passes through highly scattering media. Highly scattering media completely smears out laser mode, making it impossible for a laser beam to be focused. However, adaptive algorithms can restore the information about the laser mode after it gets distorted. The same group of authors developed and improved this algorithm to focus a laser beam anywhere inside the highly scattering object [8]. They showed that focusing in highly scattering media is possible without any knowledge about optical properties of this media. Their idea is based on considering various "scattering channels" and demixing them with the help of adaptive optics.

Nowadays, various adaptive optics algorithms appeared and evolved [9, 10, 11], and as a result, they push limits of many linear and nonlinear optical processes. For instance, Zhdanova *et al.* in their work used adaptive wavefront correction to shape spectra of supercontinuum generated in a sapphire plate [12]. Thompson *et al.* proved that with the adaptive optics it is possible to enhance Raman scattering signal [13]. Moreover, in their later works Thompson *et al.* [14] showed experimentally and proved theoretically that the fundamental limit of second harmonic generation process can be increased by wavefront correction algorithms. In the work of Tzang *et al.* [15] authors demonstrated the ability of adaptive optics to control the stimulated Raman scattering (SRS) and four wave mixing (FWM) processes in multimode fiber. They used wavefront shaping of input beams to control the superposition of modes coupled into the fiber. As a result they could manipulate the output spectra and tailor the generated sidebands. Xu *et al.* [16] in their work invented a technique, called time-reversed ultrasonically encoded (TRUE) focusing, which combines ultrasonic modulation of diffused coherent light with optical phase conjugation to achieve dynamic focusing of light into a highly scattering media. In the field of time-resolved 2D spectroscopy, group of Wright *et al.* [17] carried out a work, where they improved contrast of coherent anti-Stokes Raman scattering (CARS) microscopy by correcting both sample and system aberrations using adaptive algorithms.

This research is directed toward extending the application of wavefront shaping in general and adaptive algorithms in particular to ultrafast nonlinear optics, spectroscopy and light-matter interactions. We study the effect of adaptive optics wavefront correction onto the bandwidth of coherent Raman generation to open possibilities for the synthesis of shorter light pulses. In this case, adaptive wavefront control affects phase matching conditions. In a proof of principle experiment we generate cascaded Raman sidebands in $PbWO_4$, with the pump beam being optimized through an iterative closed-loop algorithm, which can change the beam profile dynamically and maximize the intensity of the Raman sidebands. The algorithm controls the SLM, which applies beam profile modulation, and a calibrated spectrometer, which measures the output sideband intensity. We observe a substantial increase of the total spectral width and the intensity of the higher-order sidebands, as a result of optimized Raman generation. We obtain wider Raman spectra, extended into the blue wavelength range, as well as the intensity and power increase of Raman sidebands.

We note that similar experiments employing adaptive optics algorithms can push limits of various spectroscopic techniques, such as spontaneous Raman scattering spectroscopy. Here, we consider Surface enhanced Raman scattering (SERS) [18], which is proved to be capable of detecting very small concentrations of molecules on rough nanostructured surfaces. Raman signal from the probed molecule is greatly enhanced by a localized surface plasmon, induced by the laser field on such a surface. The experimental signal enhancement achieved might be as large as 10^{14} [19], however, the quantitative theory explaining SERS enhancement is still a subject of debates [19, 20, 21, 22]. Signal enhancement can be observed if the molecule is localized in a so-called hot spot. SERS with colloids and nanostructures relies on random distribution of hot spots within the illuminated area. In this dissertation, we demonstrate the ability of wavefront correction to change Raman signal on rough nano-surfaces. By adding adaptive wavefront shaping algorithm with feedback loop to the SERS technique, we open a potential way to improve the enhancement factor. The adaptive optics algorithm tailors phase profile and changes the focal wavefront formation in accordance with surface topography. Therefore we achieve more efficient surface plasmon generation or, in the ideal case, the generation of propagating surface plasmon (so-called surface plasmon polariton). Adaptive optics could potentially improve the sensitivity for measuring low concentrations or single-molecule SERS (SMSERS) [23].

In addition to adaptive wavefront shaping we study other type of shaping: spatial shaping of laser beams, which are propagating modes of light by themselves. We take a specific example of such beams - optical vortices - that are exact solutions of wave equation in paraxial approximation. Optical vortices can be obtained experimentally either by DMDs and SLMs [24, 25, 26, 27] or with specially designed optical components [28, 29] and computer generated holograms [30]. An optical vortex beam has a characteristic donut-shaped beam profile with a zero on-axis intensity, spiral wavefront, and a light-wave phase singularity [31]. Optical vortices are well known for their defined amount of orbital angular momentum (OAM) [32], characterized by its quantum number - topological charge (TC). Applications of optical vortices include micromanipulation of particles [33]; nonlinear interactions in atomic vapors [34]; optical tweezers for biological specimens [35, 36, 37]; super resolution imaging techniques - stimulated-emission-depletion (STED) microscopy [38, 39]; vortex coronagraph for faint exoplanet detection [40, 41]. Other interesting applications of optical vortices include quantum communications and quantum computing computing [42, 43].

The intriguing property of an optical vortex is its topological charge, which is a quantum number characterizing a number of wavefront "twists" on the scale of one wavelenght. TC of an optical vortex can be transferred in nonlinear process according to the energy conservation law. In addition, it can also be transferred to a particle in so-called light-matter interactions, which makes it attractive for many of optical votrices applications. Therefore, it is very important to have a reliable and robust method to precisely measure TC in the experiment. The classical method that was proposed by Guo *et al.* [44] relies on diffraction pattern, created by propagating optical vortex through an annular aperture. Using cylindrical lens, proposed by Peng *et al.* [45], one can add the aberrations to the optical vortex, so that it will decompose onto multiple spots at the focal point of the lens, corresponding to its topological charge. Interferometric methods are very popular, because they give complete information about OAM of a vortex [46], including 2D optical field distribution along the beam. We employed many of these methods for our experiments [28, 29]. The method we are studying in detail in this dissertation was proposed by P. Vaity *et al.* [47] and used by many other researchers, i.e. in Ref. [48]. The essence of this method is to focus a vortex with a convex lens that is a little bit tilted, to take advantage of an astigmatic focusing produced by this lens. Along the course of this dissertation we study the tilted lens method for mixed states of vortices. As a result, astigmatic focusing can predict the presence of several components with different OAM. We carefully study the coherent and incoherent combinations of optical vortices with various amounts of OAM and their superpositions, and develop a new experimental technique to detect them [49]. We are focusing on a property of optical vortex to carry OAM as well as TC, and on the ability to preserve the phase singularity during the linear and nonlinear interactions.

We verify the transfer of OAM algebra among Raman anti-Stokes sidebands by using an SLM, and shaping one or both beams incident on the Raman-active crystal [50]. In this work we study femtosecond optical vortices and their properties.

Another intriguing property of optical vortices is their left- or right-handed screw dislocations of phase fronts, which is a consequence of their OAM. Optical vortices can be called chiral in the same sense as chiral molecules. If we can preserve the chirality of the vortex, while confining it into a nanometer-sized volume containing some chiral molecule, we can induce dipole-forbidden optical transitions as efficient as allowed transitions, and as a result, study molecules' chiral properties. To do this, the nano-confined field must also preserve the characteristics of the optical vortex, such as its ring of light (of a size, that is less than diffraction limit) and phase singularity in the center (zero intensity). Having chiral properties, optical vortices provide a bridge between optical physics and bioscience and can help to gain insight into the chiral properties of enantiomers. To the best of our knowledge, there is no efficient tool that exists to study chirality and the effect of OAM light on chiral molecules. The question is: how can we preserve the chirality of structured light on the nanosized scale if the light's smallest size is determined by the diffraction limit? Diffraction limits focusing of spatial light features to micron sizes, while the molecules are approximately nanometers in size. With this size mismatch, dipole-forbidden transitions (magnetic and electric quadrupole) are orders of magnitude weaker than electric dipoles. We address this question in our work [51], by developing theoretical fundmentials and building an experimental environment. The advantage of nanotechnologies gives an ability to use nano-sized plasmonic antennas to concentrate laser light into subwavelength volumes. This promotes the imaging of biological structures with ultra-high resolution. We use this advantage to design plasmonic nanoantenna for focusing of light with orbital angular momentum in a subwavelength regime ($\sim$100 nm) while preserving its chiral properties and structure. Current theoretical works demonstrate the design of such antennas [52] and experimental works show that similar designs work for THz light [53]. It is possible to optimize a working design for visible wavelengths due to scalability of plasmonic nanoantennas, and to test the system with quantum dot samples. We develop an optimal multi-element antenna design for visible (532 nm) light carrying various amounts of OAM with the COMSOL optical package software. We manufacture the designed antenna with EBL and confirm the electromagnetic field's phase, and intensity confinement, inside the subwavelength region. After that we detect the presence of OAM with the use of near-field scanning microscopy. We propose to apply the nano-strucutured OAM beams for studying two systems. First, we propose to use quantum dots as a test sample for probing forbidden transitions. Second, we study the interaction of OAM beams and double strand DNA molecules to determine their chirality. In this dissertation we aim to gain the knowledge of light-matter interactions in atoms, molecules, and biological samples beyond the dipole-dipole approximation. We see in the experiment how these systems respond to light with changing gradients on the size comparable to the size of the single molecule. We also develop techniques for optical control over the processes involved.

The dissertation is structured as follows.

Chapter 1 describes the current state of the field in detail, gives a literature review, and the reasoning as well as motivation to do current research. Chapter 2 gives all the necessary theoretical information and formulas, all basic principles and concepts that will be used in the subsequent chapters.

The work described in Chapter 3 gives the details on femtosecond optical vortices interactions with nonlinear Raman crystal. This chapter explores orbital angular momentum transfer into Raman-generated vortex sidebands. In particular, this chapter focuses on describing SLM as a tool to create optical vortices and two-dimensional spectral trace to determine the laser pulse duration with frequency resolved optical gating portable setup. In addition, we investigate the possibility to use light modulator for simultaneous two-beam modulation.

Chapter 4 describes an experiment where we investigate the possibility of using a tilted convex lens to detect the mixed OAM state and measure its topological charge. This experiment demonstrates that the OAM state of the vortex can contain several components with different OAM states and is not necessarily a pure state with a single TC value across the whole beam. These states are amplified through any nonlinear process and, as a result, can interfere with the experimental results. We develop a procedure on how to detect whether the given state is mixed and how to deal with the mixed states.

In Chapter 5 we move on to dynamical wavefront shaping algorithms. We show that an adaptive algorithm based on wavefront shaping can be applied to extend the spectra of coherent Raman generation in Raman-active crystals. Mutual coherence of Raman sidebands allows to compress the generated Raman spectra into an ultrashort pulse by overlapping the generated sidebands in space and time and adjusting their relative phases. Extending spectra into the blue region will enable synthesis of shorter, more energetic optical pulses. We build an experimental setup and discuss the algorithm, which is capable to achieve the enhancement.

In Chapter 6 we use wavefront shaping to develop a novel experimental tool for the formation of non-diffracting hollow beam structures using the combination of an axicon lens and a binary multi-sector phase plate (PP), called PP-A converter [54]. The phase plate provides an azimuthal π-modulation of the phase of the transmitted wave front. The proposed technique forms a spatial intensity pattern with a maximal intensity that is two times higher than maximal intensity of similar techniques, such as spiral phase plates. In this chapter we present in-depth simulation results along with the algorithm of manufacturing the proposed converter and its usage for high intensity laser beams.

In Chapter 7 we revisit the classic SERS experiment with rough metallic surfaces covered with thin layer of copper phthalocyanine molecules and apply an adaptive wavefront correction of laser beam profile. As a result we demonstrate the increase in brightness of local SERS hot spots and redistribution of Raman signal over the sample area. We show that the proposed adaptive-SERS modification does not depend on a surface roughness and topography, but rather works with any surface and gives more Raman signal in comparison with conventional SERS measurement. We prove that the adaptive-SERS is a powerful instrument for improving SERS sensitivity.

In Chapter 8 we propose a novel spectroscopic tool for studying chiral molecules. We describe the experiment on subwavelength focusing of light with OAM using plasmonic nanoantennas. We design and optimize the nanoantenna for OAM beam, and use focused ion beam microscope to manufacture this antenna. Then, we build an experimental setup that is capable to achieve subwavelengths focusing and detect spatial electric field distribution. In this chapter we are aiming to achieve efficient OAM light-matter transfer, that is of use for measurements chirality of molecules and probing internal atomic transitions, which are forbidden by selection rules with dipole approximation.

In Chapter 9 we summarize all obtained results and give an outlook for all the work done.

Appendix A contains Matlab code on simulation of various OAM mixed states focused with tilted lens.

Appendix B presents Matlab realization of LCOS SLM phase masks for OVs automated generator.

Appendix C presents Matlab code for generating LCOS SLM phase masks for binary phase plates.

Appendix D describes the procedure of making rough gold surfaces with nano-relief done by nanoparticle aggregations.

2. BASIC CONCEPTS AND THEORY

In this chapter we will describe all the basic concepts that we rely on in this dissertation and give the formulas that will help to understand the concepts and interpret the results given later in this dissertation. These include the derivation of the theory of optical vortices and the proof that it carries orbital angular momenta as well as descriptions of different mathematical representations of optical vortices. We will also develop the mathematical description of light's angular momenta, its components, and their roles in current research. We will briefly describe current theoretical considerations about chiral light-matter interactions with optical vortices and the modification of the internal state of a single atom during these interactions. In addition, we will briefly touch on the concepts behind coherent Raman generation and its phase-matching.

2.1 The theory of optical vortices

An optical vortex is a light beam with so-called "phase imperfection" or phase singularity. Unlike flat-phased light beams represented by flat wavefronts (e.g. Gaussian beams), the optical vortex wavefront consists of a combination of slightly inclined wavefronts, that creates a phase defect in the center. This defect causes the parts of the same wavefront to interfere destructively, and, as a result, it has zero intensity in the center of this beam. This phase defect was first studied and explained by Berry *et al.* [31], and the corresponding beams with spiral wavefront quickly became popular in optics [55], see Fig. 2.1. Not long after that, it was shown that the beams with spiral wavefront are an analytical solution of wave equation in a paraxial approximation [56, 57, 58].

Let's derive the electric field of the optical vortex, following the book "Optical Vortices" by M. Vasnetsov and K. Staliunas [58]. Scalar electromagnetic wave in Cartesian coordinates can be written as follows:

$$\left(\frac{\partial^2}{\partial x^2}+\frac{\partial^2}{\partial y^2}+\frac{\partial^2}{\partial z^2}\right)\vec{E}=\frac{1}{c^2}\frac{\partial^2\vec{E}}{\partial t^2}; \tag{2.1}$$

where $E = E(x, y, z, t)$ is an electric field; c is a speed of light.

We look for a solution of this equation, that propagates along z-axis:

$$\vec{E} = E(x, y, z)cos\Big[A(x, y, z) + kz - \omega t\Big]; \tag{2.2}$$

were $E = E(x, y, z)$ is an electric field amplitude; $k = 2\pi/\lambda$ is a wave vector; ω is a frequency of oscillations; λ - wavelengths; ω,k, and c are connected by the ratio $c = \omega/k$; the function $A(x, y, z)$ should describe the wavefront of the solution. It is more convenient for future derivation to represent *cos* factor of the Eq.2.2 in the exponential form:

$$cos\Big[A(x, y, z) + kz - \omega t\Big] = \frac{1}{2} \exp i\Big[A(x, y, z) + kz - \omega t\Big] + c.c. \tag{2.3}$$

Plugging this factor back to Eq.2.2 we get:

$$\vec{E} = E(x, y, z) \exp i\Big[A(x, y, z)\Big] \exp i\Big[kz - \omega t\Big] = \tilde{E}(x, y, z) \exp i\Big[kz - \omega t\Big]. \tag{2.4}$$

where $E(x, y, z) \exp i\Big[A(x, y, z)\Big]$ is a complex amplitude, which can be denoted as $\tilde{E}(x, y, z)$.

We note that laser radiation is a monochromatic light which spreads along one axis (*z*), and electric field amplitude does not spread in the transverse directions. Therefore, we simplify the wave equation Eq.2.1 accordingly; keeping in mind that the *z*-component of the field gradient is small, if compared to *x* and *y* components. In the following expression we neglect $\partial^2\tilde{E}/\partial z^2$, and rewrite everything in cylindrical coordinates:

$$\frac{1}{\rho}\frac{\partial}{\partial\rho}\Big(\rho\frac{\partial\tilde{E}}{\delta\rho}\Big) + \frac{1}{\rho^2}\frac{\partial^2\tilde{E}}{\partial\phi^2} + 2ik\frac{\partial\tilde{E}}{\partial z} = 0; \tag{2.5}$$

where ρ and ϕ are cylindrical coordinates. For a Gaussian solution we find:

$$\vec{E}(\rho, z, t) = E_0\frac{w_0}{w} \exp\left[\frac{-\rho^2}{w^2}\right] \times \exp i\Big[\frac{k\rho^2}{2R(z)} - \arctan\frac{z}{z_R} + kz - wt\Big] \tag{2.6}$$

where E_0 is an amplitude, w_0 is a beam waist; $R(z) = z\Big(1 + \frac{z^2{}_R}{z^2}\Big)$ - wavefront curvature. z_R

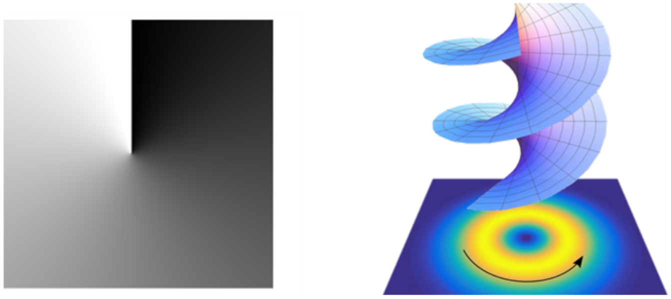

Figure 2.1: Left: schematic phase spatial profile of the optical vortex. Gray colormap depicts phase retardation along the beam profile. Black - no retardation; white - 2π phase retardation. Right: Schematic wavefront of the optical vortex. Radial black lines on spiral are equal phase lines; the yellow circle shows the transverse intensity profile of the vortex. The black curved arrow shows the direction of corkscrew wavefront rotation.

is the Rayleigh range, where the beam waist at a certain z coordinate from the beam waist $\omega = \omega_0\left(1 + \frac{z^2}{z^2{}_R}\right)^{\frac{1}{2}}$ becomes $\sqrt{2}$ larger than $z_R = \frac{k{\omega_0}^2}{2}$. $\arctan\frac{z}{z_R}$ is a Gouy phase.

From the previous equation we see that this solution does not have any azimuthal features. We can find the azimuthally dependent solutions using a Gaussian function modulated by Laguerre polynomials:

$$E(\rho,\phi,z,t) = E_0\frac{w_0\rho^{|l|}}{w^{|l|+1}}\exp\left[\frac{-\rho^2}{w^2}\right]\times\exp[-i(|l|+1)\arctan\frac{z}{z_R}+\frac{ik\rho^2}{2R(z)}+i(l\phi+kz-wt)] \quad (2.7)$$

where l is the parameter, describing the number of 0-2π phase rotations around the beam axis. This parameter is usually called topological charge (TC) of an optical vortex and is attributed to the helical wavefront of the optical vortex. In theory this parameter can be arbitrarily large; however, there are some experimental limitations on getting high order optical vortices that play a significant role in the course of this dissertation. Instability of the phase singularity point in the middle of the optical vortex is the main reason why it is not possible to get large $|l|$. When we try to push the limits, the high order singularity always tends to break into several first order singularities, which distorts an optical vortex structure. The positive l stands for the optical vortex with a right twist, and negative l stands for a left twist.

Keeping in mind that the complex amplitude contains the function $A(x, y, z)$ or in cylindrical coordinates $A(\rho, \phi, z)$, we can write down the wavefront of the resultant optical vortex field:

$$A(\rho, \phi, z) = -(|l| + 1) \arctan \frac{z}{z_R} + \frac{k\rho^2}{2R(z)} + l\phi \tag{2.8}$$

As we can see, the wafefront has a zero amplitude on a beam axis (when $\rho = 0$) and maximum at the $\omega = \omega_0$:

$$E_{max} = E_0 (\frac{|l|}{2e})^{|l|/2} \tag{2.9}$$

Radius of an optical vortex at its beam waist can be determined by:

$$\rho_{max} = \omega_0 (\frac{|l|}{2})^{1/2} \tag{2.10}$$

2.2 Angular momentum of light

As we learned in the previous section, optical vortex is an azimuthally dependent solution of the wave equation in the paraxial approximation. Its phase varies across the azimuthal angle giving it helical geometry. In this section we consider the angular momentum (AM) of optical vortex in general, and its components (SAM, OAM) in details. We will be following the book "The Orbital Angular Momentum Of Light" by L. Allen *et al.* [59] and the Refs.[60, 61]

It is known that if the entity possesses linear momentum, then we can calculate its angular momentum with respect to the origin:

$$\vec{r} \times \vec{p}, \tag{2.11}$$

where $\vec{p}$ is a linear momentum and $\vec{r}$ is the coordinate with respect to the origin.

Then, following the same logic, if electromagnetic field has some linear momentum density $\vec{\Pi} = \vec{S}/c^2$, where S is the magnitude of the Poynting vector and c is the speed of light in free space, then the total angular momentum of light can be written as follows:

$$\vec{L} = \int dr\ \vec{r} \times \vec{\Pi}, \tag{2.12}$$

where $d\vec{r}$ is an elementary volume and S is equal to

$$\vec{S} = \frac{c}{4\pi}\left[\vec{E} \times \vec{H}\right]. \tag{2.13}$$

As a result, we can rewrite the expression for angular momentum as follows:

$$\vec{L} = \frac{1}{c^2}\int dr\ \left[\vec{r} \times \vec{S}\right]. \tag{2.14}$$

In a paraxial approximation we deal with the beams that propagate along z axis, and their transverse coordinates can be written using 2 dimensional radius vector $z = \binom{x}{y}$, neglecting the change of transverse coordinates associated with z propagation. For these beams, AM along z axis is of interest:

$$\vec{L} = \vec{e}_z\mathcal{L} = \int dr\ \left[\vec{r} \times \vec{\Pi}\right] = \frac{1}{c^2}\int dr\ \left[\vec{r} \times \vec{S}\right] \tag{2.15}$$

where $dr \equiv dxdy$. A scalar $\mathcal{L}$ from previous expression can be written:

$$\mathcal{L} = \frac{1}{c^2}\int dxdy\ \left(xS_y - yS_x\right) = \frac{1}{c^2}\int drd\phi\ rS_\phi \tag{2.16}$$

where r and ϕ are polar coordinates; S_ϕ - is an azimuthal component of $\vec{S}$. We see from the Eq. 2.16, the azimuthal component of the Poynting vector defines the angular momentum with respect to z axis (S_ϕ); and the radial component S_r has no effect on AM of light.

Next, we define the components of the AM of light from Eqs. 2.15 and 2.16. For this we need to write down the expressions for the electromagnetic field of light as a superposition orthogonally polarized components:

$$\vec{E} = \vec{E}_X + \vec{E}_Y,\ \vec{H} = \vec{H}_X + \vec{H}_Y, \tag{2.17}$$

here we define $\vec{H}_X, \vec{E}_X$ components lies in yz plane and $\vec{H}_Y, \vec{E}_Y$ in xz plane. We use the Eq. 2.3 to write the components of the field:

$$\vec{E}_j(\vec{r}, z, t) = Re\Big[\vec{E}_j(\vec{r}, z)\exp(-i\omega t)\Big], \tag{2.18}$$

$$\vec{H}_j(\vec{r}, z, t) = Re\Big[\vec{H}_j(\vec{r}, z)\exp(-i\omega t)\Big]; \tag{2.19}$$

where $j = X, Y$. In the paraxial approximation, the field components can be written as follows:

$$\begin{Bmatrix}\vec{E}_X \\ \vec{H}_X\end{Bmatrix} = \exp(ikz)\left(\begin{Bmatrix}\vec{e}_x \\ \vec{e}_y\end{Bmatrix}u_X + \frac{1}{k}\vec{e}_z\begin{Bmatrix}\partial/\partial x \\ \partial/\partial y\end{Bmatrix}u_X\right), \tag{2.20}$$

$$\begin{Bmatrix}\vec{E}_Y \\ \vec{H}_Y\end{Bmatrix} = \exp(ikz)\left(\begin{Bmatrix}\vec{e}_y \\ -\vec{e}_x\end{Bmatrix}u_Y + \frac{1}{k}\vec{e}_z\begin{Bmatrix}\partial/\partial y \\ -\partial/\partial x\end{Bmatrix}u_Y\right); \tag{2.21}$$

where $\vec{e}_x$ and $\vec{e}_y$ are unit vectors of transverse coordinates; u_j are slowly varying complex amplitudes, that should satisfy the following equation:

$$i\frac{\partial u_j}{\partial z} = -\frac{1}{2k}\nabla^2 u_j; \tag{2.22}$$

where $\nabla \equiv \binom{\partial/\partial x}{\partial/\partial y}$ is a transverse gradient. Slowly varying complex amplitudes can be represented in terms of amplitude A and phase ϕ as follows:

$$u_j(\vec{r}, z) = A_j(\vec{r}.z)\exp\big[ik\phi_j(\vec{r}, z)\big]. \tag{2.23}$$

Combining derived expressions we can average Poynting vector over light oscillation period:

$$\vec{S} = \frac{c}{8\pi}Re\big(\big[\vec{E}_X \times \vec{H}_Y{}^*\big] + \big[\vec{E}_Y \times \vec{H}_X{}^*\big] + \big[\vec{E}_X \times \vec{H}_X{}^*\big] + \big[\vec{E}_Y \times \vec{H}_Y{}^*\big]\big) \tag{2.24}$$

This equation contains four terms. The first two terms can be considered combinations of various orthogonal polarization states (purely transverse). Therefore, we can write down the transverse term of $\vec{S}$

$$\vec{S}_{SAM} = -\frac{ic}{16\pi k}\left[\vec{e}_z \times \nabla\left(u_X {u_Y}^* - {u_X}^* u_Y\right)\right]. \tag{2.25}$$

Plugging this equation to Eq. 2.15 we get the following expression which is called spin angular momentum (SAM) of light:

$$\vec{L}_{SAM} = \vec{e}_z \mathcal{L}_{SAM} = \frac{1}{c^2}\int dr \left[\vec{r} \times \vec{S}_{SAM}\right]. \tag{2.26}$$

SAM of light is responsible for the polarization of light, or, in other words, SAM is responsible for the electric field component rotation around the wave vector along the beam propagation. SAM is called an intrinsic angular momentum - it exists and can be measured in any point of the light beam. It can be transferred to the matter (an atom, molecule, nanoparticle, quantum dot, etc.) in two ways: to intrinsic degrees of freedom and to extrinsic degrees of freedom. Transfer to intrinsic degrees of freedom leads to a transition of electrons from one energy level of the object to another. Transfer of SAM to the chiral molecules can rotate the light's polarization plane, which is called circular dichroism. Circular dichroism is extensively studied and relatively easy to observe because of intrinsic properties of SAM (it exists in every point of the light field). SAM can also be transferred to a mechanical degrees of freedom, which causes a micro- or nano- particle to spin around its axis. The polarization state of light and SAM considerations are out of the scope of this dissertation, however, they are essential for the derivation of orbital angular momentum of light that will be covered in the next chapters.

The last two terms in the expression Eq. 2.24 defining the polarization contributions can be separated and written as follows:

$$\vec{S}_O = \vec{e}_z S_{\parallel} + S_{\perp X} + S_{\perp Y}; \tag{2.27}$$

where the parallel component of Poynting vector represent natural energy flow (beam intensity):

$$\vec{S}_{\|} = \frac{c}{8\pi}(A^2{}_X + A^2{}_Y). \tag{2.28}$$

Perpendicular component represents combination of transverse flow and polarization states:

$$\vec{S}_{\perp j} = \frac{ic}{16\pi k}(u_j \nabla + u_j{}^* - u_j{}^* \nabla u_j); \tag{2.29}$$

which, if plugged in the Eq. 2.15, represents orbital angular momentum (OAM) of light:

$$\vec{L}_{OAM} = \vec{e}_z \mathcal{L}_{OAM} = \frac{1}{c^2}(u_j \int dr \left[\vec{r} \times \left(\vec{S}_{\perp X} + \vec{S}_{\perp Y} \right) \right]. \tag{2.30}$$

OAM of light possesses a helical wavefront and is responsible for the helicity of the light, meaning the azimuthal phase change across the beam axis. This phase change has quantum nature, which will be discussed in the later chapters. OAM is extrinsic - it exists and can be measured only on the beam axis. One can transfer OAM to the mechanical degrees of freedom of an object, which will make it spin around the beam's axis. However, it is very challenging to transfer OAM to the internal (electronic) degrees of freedom of the particle because this transfer can only happen at the beam axis, when the particle is perfectly aligned with the beam. This is challenging to achieve experimentally for many reasons, this will be discussed in later chapters. Developing the efficient way to transfer OAM to the internal degrees of freedom is the main topic of this dissertation.

As a results of the derivation above, it is clear, that AM of light is a physical quantity that has defined properties and obeys the energy and moment conservation laws. On the other hand, the two components of AM: SAM and AOM are derived as a convenient mathematical expressions, and in this sense, they do not necessarily possess well-defined properties, and do not have defined conservation laws [62]. However, in some cases (for instance, in the case of optical vortices), both SAM and OAM are considered entities with well-defined quantitative characteristics.

2.3 Bessel modes of optical vortices

Laguerre-Gaussian optical vortex mode is not the only way to realize optical vortices in both theory and the experiment, as in Section 2.1. They can be "built-in" to the other fundamental modes of light. In this section we derive optical vortices in Bessel beam carriers. Bessel beams are interesting for different research areas because they are non diffractive, and when combined to the optical vortices, Bessel beams transfer this property to optical vortices.

We derive Bessel beams with OAM as a solution of the wave equation Eq. 2.1, following the article "Bessel beams", by K. T. McDonald [63] in cylindrical coordinates:

$$\left(\frac{\partial^2}{\partial x^2}+\frac{\partial^2}{\partial y^2}+\frac{\partial^2}{\partial z^2}\right)\vec{E}-\frac{1}{c^2}\frac{\partial^2\vec{E}}{\partial t^2}=\left[\frac{\partial^2 E_z}{\partial\rho^2}+\frac{1}{\rho}\frac{\partial E_z}{\partial\rho}+\frac{1}{\rho^2}\frac{\partial^2 E_z}{\partial\phi^2}+\frac{\partial^2 E_z}{\partial z^2}-\frac{1}{c^2}\frac{\partial^2 E_z}{\partial t^2}\right]\vec{e}_z=0 \tag{2.31}$$

where E_ϕ, E_ρ and E_z are in the following form:

$$E_j(\rho,\phi,z,t)=f(\rho)\exp i(k_z z-\omega t\pm l\phi), \tag{2.32}$$

where l is a TC, derived above. For the case that $E_\phi=E_\rho=0$ and $E_z=\psi$ we derive:

$$\frac{d^2 f}{d\rho^2}+\frac{1}{\rho}\frac{df}{d\rho}+\left(k_f^2-k_z^2-\frac{l^2}{\rho^2}\right)f=0. \tag{2.33}$$

The expression above represent Bessel equations, therefore the solution of this equation is a Bessel function of the l^{th} order:

$$f(\rho)=J_l(\rho'). \tag{2.34}$$

The one set of the Bessel beams generated with the vector potential $E_\phi=E_\rho=0$ can be written as follows:

$$E_z(\rho,\phi,z,t)=J_l(\rho')\exp i(k_z z-\omega t\pm l\phi); \tag{2.35}$$

where $k_z = k_f \cos\alpha$ and $\rho' = \rho k_f \sin\alpha$. The Eq. 2.35 shows that the Bessel beams in this case do not have a flat phase profile. Their phase front is represented by azimuthal phase change similar to Laguerre-Gaussian beams. The wave vector of Bessel beam can be written as follows:

$$\vec{k} = \vec{\nabla}(k_z z \pm l\phi) = k_z \vec{e}_z \pm \frac{m}{\rho}\vec{e}_\phi, \tag{2.36}$$

that is perpendicular to the wavefront of the beam (surfaces with constant phase) and makes a circle in time of radius ρ. Therefore, the angle, that $\vec{k}$ makes with the propagation axis can be expressed:

$$\beta = \arctan\big(\pm \frac{l}{k_z \rho}\big) \tag{2.37}$$

2.4 Allowed and forbidden electronic transitions in molecules

Transfer of light to the internal degrees of freedom during light-matter interactions is highly restrictive process. In order to be able to modify the internal states of matter (i.e. atom) one needs to tailor electromagnetic field to satisfy selection rules of the particular atom. The electromagnetic field modifications include frequency, polarization state, and angular momentum. By satisfying selection rules we can efficiently drive any transition we want. The thorough derivation of how the electromagnetic field in paraxial approximation affects the internal state and center of mass motion of an atomic system can be found in Refs. [64], [65],[66] and [67], that we will follow in this section. The mentioned references investigate theoretical aspect of light matter interactions in full, which is out of the scope of this dissertation. Therefore, we would like to avoid extensively repeating the authors, and only highlight the key findings. The work of R. Jauregui [64] analyzes the effect of Bessel photon on the atomic system beyond the dipole approximation; moreover, it proves that for the efficient OAM light-atom transition, the beam axis should be aligned with the atom. A. Alexandrescu *et. al* in their work [65] theoretically show the exchange of angular momentum between Laguerre-Gauss light beam and atomic system. R. Jauregui in her work [67] presents systematic analysis of modifying transition rates in atomic system by tailoring the electromagnetic field. They consider various modes of light and derive both the internal state transition rates and the conditions for their enhancement or inhibition. In this section, we highlight the selection rules modification that is happening inside an atom illuminated by the light with OAM.

The electromagnetic radiation-hydrogenlike atom interaction is described by the Hamiltonian, following the work of R. Jauregui [64]:

$$\hat{H} = \hat{H}_P + \hat{H}_R + \hat{H}_I, \tag{2.38}$$

where

$$\hat{H}_P = \frac{p_e^2}{2M_e} + \frac{p_N^2}{2M_N} + V_r + V_R, \tag{2.39}$$

$$\hat{H}_R = \sum \int dk_\perp dk_z \hbar\omega \frac{1}{2}\left(\hat{a}_l^{(i)\dagger}\hat{a}_l^{(i)} + \hat{a}_l^{(i)}\hat{a}_l^{(i)\dagger}\right), \tag{2.40}$$

M_e, M_N are masses of opposite sign charges in hydrogenlike atom, $\vec{r}_e$, $\vec{r}_N$ are their coordinates, V_r, V_R - internal and external potentials, that depend on $\vec{r} = \vec{r}_e - r_N$ and R_{CM} coordinates correspondingly, where CM stands for center of mass; $\hat{a}_l^{(i)}$, $\hat{a}_l^{(i)\dagger}$ are annihilation and creation operators; l - is a TC of the electromagnetic field; and $\hat{H}_I$ is interaction Hamiltonian.

$$\hat{H}_I = \hat{H}_{I1} + \hat{H}_{I2} + \hat{H}_{I3}, \tag{2.41}$$

We will consider the interaction with H_{I1} part of interaction Hamiltonian:

$$\hat{H}_{I1} = -\sum_{i=1}^{2} \frac{q_i}{M_i} \vec{p}_i \cdot \hat{A}(\vec{r}_i). \tag{2.42}$$

When the atom makes a transition from initial $\vec{\Psi}_0$ to final $\vec{\Psi}_F$ state, we can write this as follows:

$$
\begin{aligned}
\langle F, 1_{\kappa}^{(i)}|H_{I1}|0;0\rangle = {} & \frac{1}{i\hbar}(E_{CM}^{(0)} - E_{CM}^{(F)}) \int d^3r d^3R[\vec{\Psi}_F^*(\vec{r},\vec{R})\vec{R}\vec{r}\vec{\Psi}_0^*(\vec{r},\vec{R})]\times \\
& \times\left[q_e\vec{A}_{\kappa}^{(i)}\left(\vec{R}+\frac{\mu}{M_e}\vec{r}\right)+q_N\vec{A}_{\kappa}^{(i)}\left(\vec{R}+\frac{\mu}{M_N}\vec{r}\right)\right]+ \\
& +\frac{1}{i\hbar}(E_{rel}^{(0)} - E_{rel}^{(F)}) \int d^3r d^3R[\vec{\Psi}_F^*(\vec{r},\vec{R})\vec{R}\vec{r}\vec{\Psi}_0^*(\vec{r},\vec{R})]\times \\
& \times\left[q_e\frac{\mu}{M_e}\vec{A}_{\kappa}^{(i)}\left(\vec{R}+\frac{\mu}{M_e}\vec{r}\right)+q_N\frac{\mu}{M_e}\vec{A}_{\kappa}^{(i)}\left(\vec{R}+\frac{\mu}{M_N}\vec{r}\right)\right]
\end{aligned}
\tag{2.43}
$$

For optical Bessel beams and standard atomic systems:

$$
{}_l(\rho,\phi;k_\perp) = J_l(k_\perp\rho)e^{il\phi} \tag{2.44}
$$

The transition rate can be approximated as follows:

$$
\langle F, 1_{K}^{(i)}|H_{I1}|0;0\rangle \sim \frac{q_e}{i\hbar}(E_{rel}^{(0)} - E_{rel}^{(F)}) \int d^3R\Phi_0^*(\vec{R})\vec{A}_K^{(i)*}(\vec{R})\Phi_F(\vec{R}) \int d^3r\phi_F^*(\vec{r})\vec{r}\phi_0(\vec{r}). \tag{2.45}
$$

This expression has the standard dipole matrix element for the relative coordinates. If we go beyond this approximation, following the derivation in the Ref. [64] we will see that the energy involved in the center of mass motion is much smaller than the energy that goes to internal state change. Therefore, the term proportional to $E_{rel}^{(0)} - E_{rel}^{(F)}$ in Eq. 2.43 will be important. Additionally, in the quadrupole approximation we have:

$$
e^{ik_z(z_R+q_z)} \sim e^{ik_z z_R(1+ik_z q_z)} \tag{2.46}
$$

If we plug the expression above to the probability ampltudes Eq. 2.43, the terms that are proportional to $r_\perp$ and z will lead to a quadrupole matrix element of relative motion $x_i x_j$. Therefore, the standard selection rules will be:

$$\delta l_z^{rel} = \pm 2\hbar, \pm 1\hbar, 0. \tag{2.47}$$

These modified selection rules were proved and tested experimentally [68, 69], where authors excited an atomic transition with a diffraction limited optical vortex and demonstrated the transfer of optical orbital angular momentum to the valence electron of a single trapped $^{40}\mathrm{Ca}^{+}$ ion.

2.5 Chiral light-matter interactions, OAM transfer to chiral molecules

As it was mentioned before, an optical vortex (OV) has a helical profile, that can be right-handed or left-handed. There is no developed theory or proof of concept experiments on the spectral discrimination of oppositely handed molecules induced by OAM light, nor is there a clear understanding on what should happen on a fundamental level with a chiral molecule, illuminated by the right- or left-handed light. Does the OAM of light play any role in chiral light-matter interactions [70]? Can any piece of matter discriminate between right handed light and left handed light [71]? In earlier theories and experiments, it was assumed that OAM cannot be transferred to light [72, 73]. However, the discussion continued over the years, and researchers have started to find evidence of the opposite [74]. It is known, that with OAM light the phase singularity in the middle plays a significant role in OAM light-matter transfer. For this transfer to occur, a chiral molecule should be located on the beam axis, and the beam should be tightly focused. Otherwise, the molecule will only see the vortex dark center, which means that the particle will not interact with light. This brings us to the conclusion, that a robust experimental tool needs to be developed to reduce the optical vortex diameter and to optimize the optical axis-molecule alignment. Moreover, the theoretical concepts to support this problem need be developed as well. In this section we will be following the work of Forbes and Andrews [71], where they derive all existing theoretical instrumentation to study OAM chiral interactions.

We assume that the interaction Hamiltonian is derived, and the electronic transition probabilities in multipole approximation are calculated in the previous sections. We also assume that if chiral molecule enantiomers cannot be superimposed, then the chiral molecule can only be non-centrosymmetric. We need to make a connection between the dipole electric (E1), dipole magnetic (M1) and quadrupole electric (E2) transitions (the terms in quadrupole approximation) and a chirality (or absence of centrosymmetry) of a molecule. At this point the selection rules of a molecule/atom come into play. Selection rules for chiral light-matter interactions will depend on the "spatial parity signature" of E1 (odd), M1 and E2 (even). We know, that for any electronic transition, the multiplication of electronic symmetries of the initial state and final state must contain irreducible terms in multipole approximation (in a rate equation). For example, for a non-chiral molecule, both odd- and even-parity moments transitions cannot be allowed. The same exclusion rule applies for chiral media. For chiral media (noncentrosymmetric molecule) the transition can be allowed with E1M1 (or E1E2) moment products simultaneously, unlike for centrosymmetric molecules. And M1E2/E2E2 moment products can be allowed in both centrosymmetric and non-centrosymmetric molecules.

By this logic we can calculate the transition rates for E1E2 (as an example) dipole moments and extract relevant terms, which exhibit a l dependence:

$$\Gamma^{L/R}_{E1E2}(l) = \sigma l \frac{\kappa}{r} \epsilon_{ikm} \hat{k}_m \hat{\phi}_j \mu_k Q_{ij} \tag{2.48}$$

where $\sigma = \pm 1$ is a helicity for left (L) and right (R) handed light; $\kappa = I(\omega) F^2_{l,p}(r)/2c\hbar^2\epsilon_0$; ϕ is azimuthal angle; $\hat{Q}$ is a transition electric quadrupole operator. The expression above is dependent on both spin and orbital angular momenta (SAM and OAM) of light. The other chiral transitions can be derived by analogy.

2.6 Raman scattering

The significant part of this dissertation is dedicated to the Raman scattering. We study two types of Raman scattering in detail: coherent Raman scattering and spontaneous Raman scattering. In this section we will give basics of both types of Raman scattering. Raman scattering is a type of inelastic scattering of photons, that causes the energy transfer between vibrational or rotational

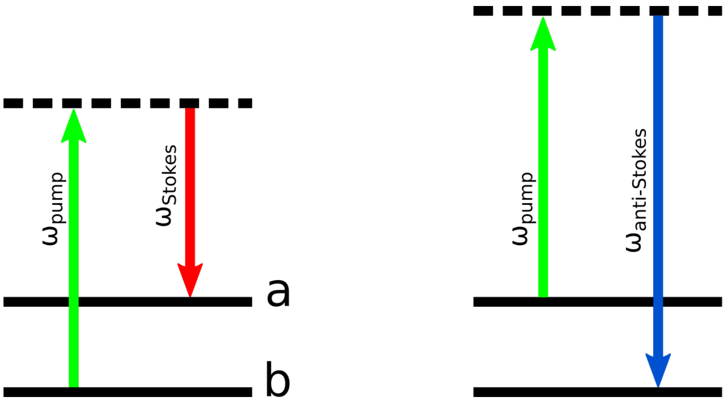

Figure 2.2: Vibrational energy level scheme for Raman scattering process. Left: Stokes scattering happening if pump hits the molecule on the level b, and scattered photon excites the molecule to the vibrational level a. Right: Anti-Stokes scattering happens when pump photon hits the molecule in the excited vibrational state a and the scattered anti-Stokes photon brings the molecule back to the lower vibrational level.

states of matter [75]. Figure 2.2 shows the simplest energy level diagram sufficient to describe Raman scattering. After the scattering, a photon will change its frequency as follows:

$$\begin{aligned} \omega_S &= \omega_{pump} - \omega_{ab} \\ \omega_{AS} &= \omega_{pump} + \omega_{ab}; \end{aligned} \tag{2.49}$$

where ω_{pump} - is a frequency of a photon before scattering; $\omega_{ab} = \omega_R$ is a vibrational (rotational) frequency, so called Raman shift; ω_S - frequency of red-shifted photon after scattering (Stokes) $\omega_A S$ - frequency of blue-shifted photon after scattering (anti-Stokes).

If we prepare molecular coherence inside the Raman medium by two beams - pump and Stokes (or anti-Stokes) - we ensure that all the molecules are in the same state and vibrating in the unison. This process is called coherent Raman scattering, and can be singificantly more efficient than spontaneous Raman scattering.

For the coherent Raman scattering, phase-matching conditions need to be satisfied, Fig. 2.3 [75]:

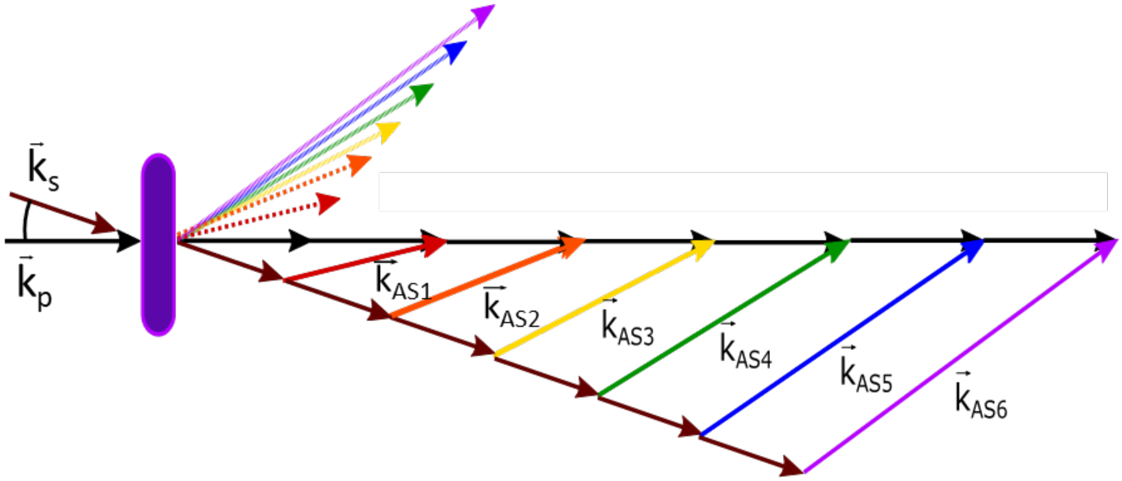

Figure 2.3: Geometrical derivation of the direction of output Raman anti-Stokes sidebands (AS1-AS6). Solid lines are the result of geometrical sum of (n-1) pump photons and n Stokes photons, where n is the order of generated AS sideband; $\vec{k_p}, \vec{k_S}, \vec{k_{ASn}}$ are wave vectors of pump, Stokes and anti-Stokes. Dashed lines are obtained by parallel translation of solid lines and depict the experimental direction of AS sidebands behind the Raman-active crystal.

$$\vec{k}_{AS1} = 2\vec{k}_p - \vec{k}_s. \tag{2.50}$$

If the process goes efficiently, it can cascade, Fig. 2.4. Therefore, phase-matching conditions will be the following:

$$\vec{k}_{AS1} = 2\vec{k}_p - \vec{k}_s,$$

$$\vec{k}_{AS2} = \vec{k}_{AS1} + \vec{k}_p - \vec{k}_s = 3\vec{k}_p - 2\vec{k}_s,$$

$$\vec{k}_{AS3} = \vec{k}_{AS2} + \vec{k}_p - \vec{k}_s = 4\vec{k}_p - 3\vec{k}_s,$$

$$\ldots,$$

$$\vec{k}_{ASn} = (n+1)\vec{k}_p - n\vec{k}_s, \tag{2.51}$$

The same can be derived from a phase relationship among the applied and generated beams: $\phi_n = (n+1)\phi_p - n\phi_s$ (where ϕ_n is the relative phase of the nth field, in the transverse plane) [29].

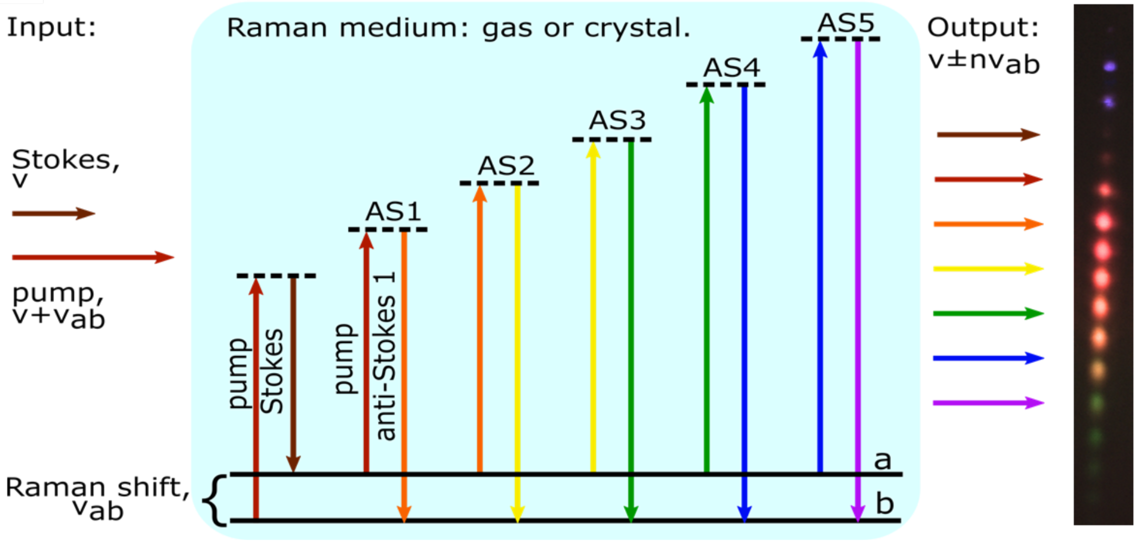

Figure 2.4: Vibrational energy level scheme of cascaded coherent Raman scattering process in crystal with high refractive index. Input pump and Stokes ultrashort beams generate anti-Stokes beam (AS1), that can serve as a pump for the next step of cascading process. As a result - multiple Raman anti-Stokes sidebands, separated by the energy difference between two levels: a and b. The photo on the left shows that output AS beams are spread out in space because of high refraction index of the crystal.

This is analogous to how photon momentum conservation is equivalent to wave vector (k-vector) matching. Therefore, we see from the Fig. 2.3 that the phase matching conditions for *n*-th AS depend on, (*n*-1)-th AS and overall is very complex.

It is interesting how the efficiency of generating AS1 affects generation of AS9 (Fig. 2.5). We can estimate the crossing angle change for the AS1 generation (the simplest case, dependence only on one pump-Stokes beams orientation). The phase-matching conditions can be seen from the equation for the phase mismatch factor for Raman generation:

$$M = sinc^2[(k_R - k_{opt}) \times L/2], \tag{2.52}$$

where $(k_R - k_{opt})$ stands for the wave vector mismatch, $L = 500\mu m$ - the crystal thickness, k_R - the wave vector modulus of the generated Raman sideband, k_{opt} - the wave vector modulus of the generated Raman sideband calculated from the geometrical representation of wave vectors; for

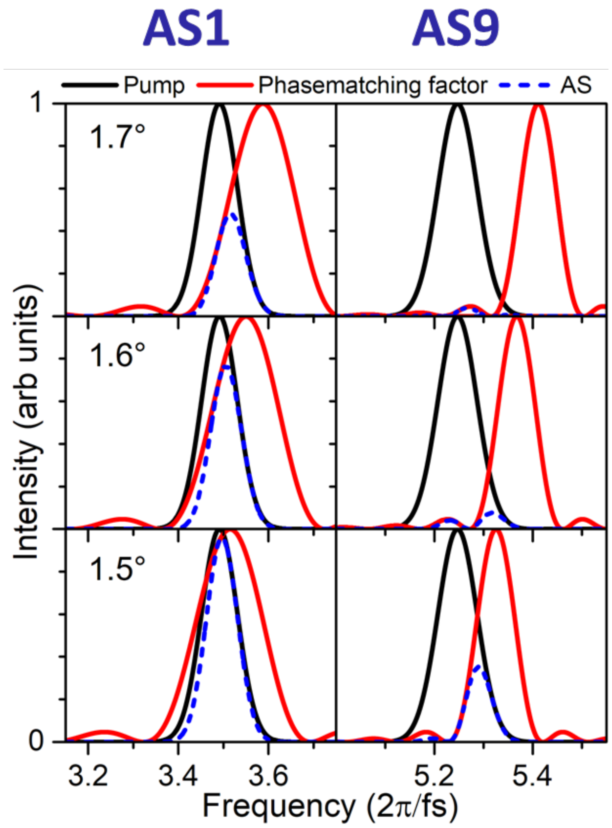

Figure 2.5: A simple example of how phase matching angle affect the phase-matching conditions of cascaded Raman scattering. Upper row: If the phase matching angle is not optimal ($1.7°$), then pump frequency overlap with the optimal phase-matching factor for AS1 generation is poor, and AS1 is being generated less efficiently. This affects the efficiency of generation of AS2-AS8. As a result, the overlap between pump and phase-matching factor of AS9 is almost zero, so AS9 is generated. Middle row: AS1 and AS9 sidebands generation efficiencies with more optimal initial phase-matching angle ($1.6°$). With the initial angle being optimized, we can change the overlap between phase-matching factors and pump beam. Bottom row: AS1 and AS9 sidebands generation efficiencies optimal initial phase-matching angle ($1.5°$).

example, for AS1:

$$k_{opt} = [4k_p^2 + k_S^2 - 4k_p k_s cos\theta]^{1/2}, \tag{2.53}$$

where k_p and k_S - are the moduli of the wave vectors for the pump and Stokes fields correspondingly. The mismatch factor characterizes the efficiency of Raman anti-Stokes wavelength generation. Ideal phase matching happens at $(k_R - k_{opt}) = 0$ and $M = 1$, so the generated AS serves as a pump for next order process and so on. We study this process for ultrashort pulse synthesis and investigate how the wavefront optimization can increase the efficiency of the process.

3. ORBITAL ANGULAR MOMENTUM TRANSFER IN COHERENT RAMAN GENERATION*

This work focuses on the interaction of optical vortices, and femtosecond optical vortices in particular [76], with nonlinear Raman-active crystals [77]. Coherent multi-sideband Raman generation offers opportunities for the production of ultrashort (sub-femtosecond) optical pulses of adjustable shapes and for non-sinusoidal field synthesis [78, 79, 80]. The possibility of adjusting the transverse beam profile and producing coherent Raman sidebands of various vortex shapes adds another dimension to light-field shaping. The goal of our present work is to explore the process of transferring topological charge (otherwise known as the TC algebra) from input femtosecond beams into Raman-generated vortex sidebands. Topological charge is related to the OAM, but is generally not the same [81, 82]. However, the equation that governs TC transfer may still be derived from either orbital angular momentum conservation for created and annihilated photons or, equivalently, from considerations of phase-matching between the applied and generated beams. OAM, as a rule, is only conserved in cylindrically symmetric systems (*i.e.* in collinear setups), but is approximately conserved at sufficiently small angles (on the order of 10°, which is significantly larger than the value used in our experiment), as [42, 83, 84, 85] have shown in spontaneous parametric down conversion, second harmonic generation, and four wave mixing.

3.1 Methods

Our experimental setup is shown in Fig. 3.1. As is described in [86], we used a Ti:Sapphire regenerative amplier (Coherent, Legend) to produce infrared ($\lambda = 802$ nm) 35 fs pulses with a 1 kHz repetition rate and 1 W average power. We then chirped these pulses by changing the grating distance within the compressor unit of the amplier, producing pulses of around 200 fs. We retrieved the precise chirp using a second harmonic (SH) frequency-resolved optical gating (FROG) setup,

---

*Part of this chapter is reprinted from "Topological charge algebra of optical vortices in nonlinear interactions." Zhdanova, Alexandra A., Mariia Shutova, Aysan Bahari, Miaochan Zhi, and Alexei V. Sokolov, Optics express 23, no. 26 (2015): 34109-34117, copyright 2015, with kind permission from the Optical Society.

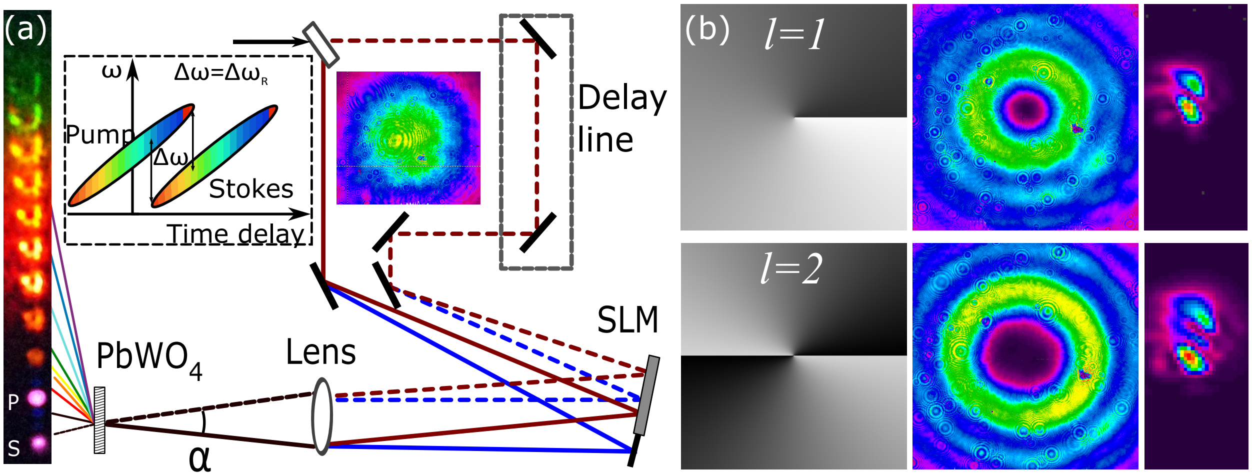

Figure 3.1: (a) Our experimental setup. Dashed lines correspond to Stokes beam, while solid lines correspond to pump. The blue lines correspond to the one-beam modulation case and the red lines correspond to the two-beam modulation case. The angle of the SLM is greatly exaggerated. Typical sidebands produced from this arrangement are also shown. The inset schematically depicts our two chirped pulses and the delay between them. (b) Computer generated phase masks (left), optical vortices obtained with these phase masks just before the focusing lens, approximately 76 cm after the SLM (middle), and vortices focused with a tilted lens (right).

with software provided by R. Trebino [87]. We determined the sign of the chirp by performing a SH-FROG before and after adding a slab of glass to the beampath of our chirped pulse.

The beam was then split into pump and Stokes beams by a non-polarizing beamsplitter. We adjusted the power in each beam with separate neutral density filters and observed the behavior of the generated coherent Raman sidebands. By tuning the power we were able to reduce nonlinear parasitic effects and thus optimize the quality of the sidebands. Finally, after either one or both beams were spatially modulated, they were focused (by separate 50 cm lenses) and recombined at a small angle (3.16 degrees, to satisfy phase matching conditions) in a lead tungstate ($PbWO_4$) crystal placed 2.5 cm before the focus, resulting in a beam diameter of about 1 mm. This distance ensured that the intensity was low enough that parasitic effects (such as self-phase modulation) did not dominate over the Raman generation.

The relative pulse delay, phase matching, and chirp chosen excited the $PbWO_4$ Raman mode of 325 cm^{-1} [86], as we confirmed with a spectrometer. As is shown in the inset of Fig. 5.4, for positive chirp (which is what we used for all results given here), the leading pulse acted as pump and the delayed pulse acted as Stokes. In this configuration, the Raman mode is driven by the instantaneous frequency difference $\Delta\omega = b\tau$, where τ is the relative delay of the two pulses (in femtoseconds) and b is their chirp rate (in cm^{-1}/fs) [86]. A standard set of sidebands thus generated is shown in Fig. 5.4(a). We label the sidebands as anti-Stokes One (AS1), anti-Stokes Two (AS2), and so on.

3.1.1 Spatial light modulator setup

A spatial light modulator (Hamamatsu x$10468 - 02$) was used for all spatial shaping of the beam. We optimized the phase masks (*i.e.* by adding a constant phase or multiplying by a constant) to produce beams which appear darkest in the center in the far field, as measured by a beam profiler (Spiricon SP620U). We confirmed independently, by using an interferometric setup, that these beams correspond to vortex beams that exhibit the proper behavior when interfered with Gaussian beams. These phase masks and examples of the beams thus produced are shown in Fig. 5.4. We performed two sets of experiments; for the first, we only spatially shaped one beam (so that the topological charge did not equal 0) and left the other as a Gaussian. Therefore, only one beam was input to the SLM and we were able to use the full size of the beam. For the second setup, we reduced the size of both beams by 25% with a telescope placed before the beamsplitter, so that the diffraction that resulted from the clipping of one beam on the SLM was avoided. The telescope was built with thin negative miniscus and plano-convex lenses to produce minimal spherical aberrations.

3.1.2 Frequency resolved optical gating setup

An essential part of the experiment is to carefully measure the laser pulse length, and precisely define chirp. For this we use frequency resolved optical gating (FROG) algorithm developed by Trebino's group [87]. We assemble a separate portable setup for taking FROG measurements in this and further experiments, Fig.3.2. The flip mirror redirect pump beam, switching its direction from experimental setup to FROG measurement setup. Beamsplitter splits pump beam into two

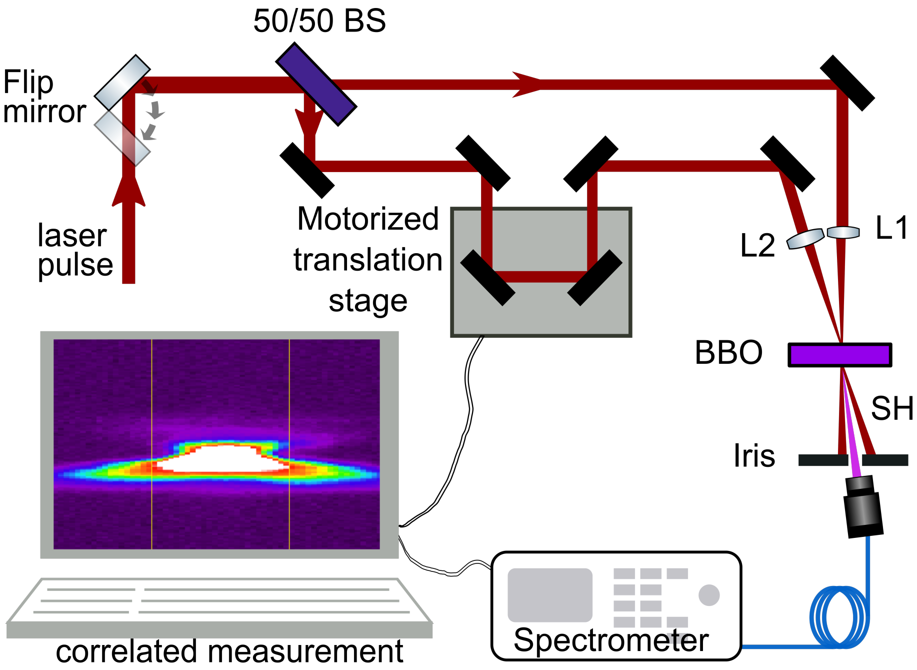

Figure 3.2: Schematic FROG setup. Flip mirror is used to quickly switch from main setup to FROG measurements. BS is beam splitter; L1 and L2 are focusing lenses, iris aperture is used to filter out fundamental beams; SH is second harmonic generated in BBO crystal

beams, the delay line (motorized programmable high resolution translation stage) connected to one part of the beam. Delay line allows to adjust relative phases between two parts of the beams. After the delay line beams are recombined in nonlinear type 1 BBO crystal for nonlinear autocorrelation measurement of generated second harmonics spectra. The motorized translation stage and spectrometer are connected to the computer, through the automated LabVIEW software, that adjust proper timing for each measurement. In order to get FROG trace one needs to take the evolution of SH spectra, generated in BBO in between two pumps with small micron (fs) delay step size. The example of the FROG trace and retrieved pulse length and phase is shown in Fig. 3.2

3.2 Results

3.2.1 One beam modulation with SLM

As mentioned above, after generating a set of Raman vortex sidebands, the TC for each sideband was checked by focusing with a lens tilted by ~ 6 degrees [47] and counting the number of spots in the focal plane. The number of observed spots is equal to $l_n + 1$. The spots form a tilted row and the slope of this row corresponds to the sign of TC, such that positive slope corresponds to positive TC and vice versa, as shown by Figs. 3.2.1-3.3.

We were able to generate up to 7 high quality vortices with $l_s = \pm 1$, without any background nonlinear processes and noise, and 15 vortices (up to blue wavelengths) at the maximum intensity below the burning point of the crystal. However, the intensity of the vortices generated with $l_s = \pm 2$ and ± 3 is lower than for $l_s = \pm 1$. Accordingly, only 6 AS sidebands were generated for $l_s = \pm 2$ and 5 AS sidebands for $l_s = \pm 3$. We hypothesize that this is due to the increase in the bright area of each vortex, as was shown in [88, 89] and as seen in Fig. 5.4. Therefore, as the vortex order increases, the peak intensity (at a fixed point) becomes smaller, impacting the Raman generation negatively. We can calculate the bright area A_l of a Laguerre-Gauss beam of order l generated from a Gaussian beam of radius w_0, using a formula from [89]: $A_l = \pi w_0^2 \sqrt{(l + 1.3)^2 - l^2 e^{-1.4/l}}$, so the intensity of an $l = 2$ beam is 75% of that for an $l = 1$ beam, and the intensity of an $l = 3$ beam is 83% of that for an $l = 2$ beam. However, it is important to note that the question of conversion efficiency is quite complicated, and a reduced efficiency can be due to a wide variety of other factors, such as spatial overlap and the increased divergence of higher order beams. Reduction in peak intensity is only the most obvious and most dramatic cause.

Finally, we checked the TC of the first three AS sidebands for $l_s = \pm 1$, ± 2 and the first two AS sidebands for $l_s = \pm 3$, as is shown in Fig. 3.2.1. Our measurements were limited by the resolution of the intensity distribution at the focus for each vortex; despite our use of loosely focusing lenses, we were unable to resolve the 10 spots theoretically predicted for AS3 of $l_s = \pm 3$.

3.2.2 Two beam modulation with SLM

In this experiment, we tested 4 different combinations of TC of input beams but kept the difference $|l_p - l_s|$ equal to 3. To confirm that the topological charge transfer took place, even for such a relatively large value of $|l_p - l_s|$, we measured the resultant TC of AS1.

As depicted in Fig. 3.3, the sidebands generated in this experiment are worse in quality (have diffraction fringes and are not complete donut shapes) and efficiency (they are barely seen by

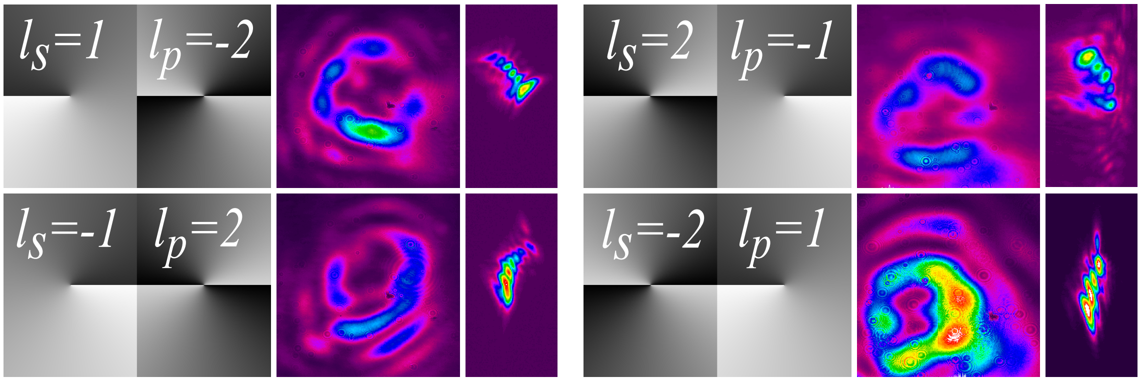

Figure 3.3: TC measurement of Raman sidebands using a tilted lens. For each block: digital phase maps for generating pump and Stokes beams (left), AS1 generated when these phase maps are applied (middle), AS1 focused with tilted lens (right).

eye) than sidebands generated with one modulated beam. Our experience has taught us that small changes (such as any coma introduced by lenses) from ideal spatial alignment can add a significant amount of distortion to Raman-generated beams. This issue is especially relevant for Raman-generated vortices, as any distortions in the beam profile reflect distortions in the carried OAM.

4. DETECTION OF MIXED OAM STATES VIA VORTEX BREAKUP [*]

To understand the nature of OAM and TC in our previous study we investigate the possibility of using a tilted convex lens to detect the mixed OAM state and measure its TC [49] . This means that the OAM state of the vortex may not necessarily be a pure state with a single TC value across the whole beam, but may contain several components with different OAM states and corresponding values of TC. These states arise as a result of flaws in the optical devices, such as spatial light modulators (SLM) or computer-generated holograms (CGH), widely used for generating vortices [90, 91] and may be amplified through any nonlinear process [92, 58]. As a result, the nonlinearly generated vortex beams may represent a mixed state [50] containing comparable amounts of different OAM values. The results of our theoretical and experimental work show that the tilted lens technique can be used to detect a mixed OAM state (superposition of two components) and helped us study the classical nature of OAM superposition.

4.1 Introduction and background

The optical vortex (OV) is a light beam with a donut-shaped transverse profile and a spiral wavefront. Its phase exhibits a singularity in the center (where the intensity is zero) and carries an amount of orbital angular momentum (OAM) per photon equal to $\hbar l$, where l is the topological charge (TC) of the OV [59]. The OAM properties of OVs are actively being studied because of their many applications, such as free space telecommunications [93], mode division multiplexing in a fiber [94, 95] optical micro- and nanomanipulation [96, 37, 97], astronomy [41] and many others. Since measurement of the TC is the common inevitable link in studying these processes, it is very important to characterize the standard measurement techniques thoroughly.

There are a variety of methods for measuring the TC of OVs; some are based on interferometry [98, 99, 100], others use an annular [44] or triangular aperture [101]. Methods based on the

---

[*] Part of this chapter is reprinted from "Detection of mixed OAM states via vortex breakup." Shutova, Mariia, Alexandra A. Zhdanova, and Alexei V. Sokolov, Physics Letters A 381, no. 4 (2017): 408-412, copyright 2017, https://doi.org/10.1016/j.physleta.2016.09.031, under Creative Commons licence https://creativecommons.org/licenses/by/4.0/.

property of multi-singular optical vortices to deform in the presence of some astigmatic media are particularly relevant to experimental use because of their extreme simplicity. Astigmatic laser beam behavior, propagation, and transformation were studied theoretically and experimentally in some detail for both Bessel modes of light [102], and Laguerre-Gaussian [103, 104] ones. The invention of a rather simple Hermite to Gaussian (and vice versa) mode converter exploiting a cylindrical lens to add astigmatism into the beam [56, 105] evolved into several techniques which allow experimentalists to measure the topological charge of OVs very easily [106, 47]. In this work, we study this last category of techniques, where we add astigmatism into the beam by inserting a tilted plano-convex lens; this technique is referred to throughout the manuscript as the “titled lens technique". This method has successfully been shown to measure the magnitude and sign of an OV with TC up to $|l| = 14$ [47].

In the current work, we investigate the possibility of using a tilted convex lens to detect the mixed OAM state [107] and measure its TC. As already stated above, the OAM state of the OV may not necessarily be a pure state with a single TC value across the whole beam, but may contain several components with different OAM states and corresponding values of TC. These states arise as a result of flaws in the optical devices, such as spatial light modulators (SLM) or computer-generated holograms (CGH), widely used for generating OVs. In practice, these devices create wavefronts which differ from the ideal and may have distorted phase and amplitude [90, 91]. Because SLMs and CGHs are phase-only modulators, these small distortions can be interpreted as separate components of the beam with different TCs (since TC is the only parameter which characterizes phase). Because nonlinear process amplify small perturbations (noise) [92, 58], these extra components play a large role for OVs in different nonlinear processes such as second harmonic generation [108], Raman generation with femtosecond OVs [109, 28, 110], or white light generation [111]. As a result, the nonlinearly generated beams may become so distorted that they represent a mixed state [50] containing comparable amounts of different OAM values.

This mixed state may be coherent – when components do interfere with each other [112] or incoherent – when components do not interact with each other. When the mixed state is coherent, it

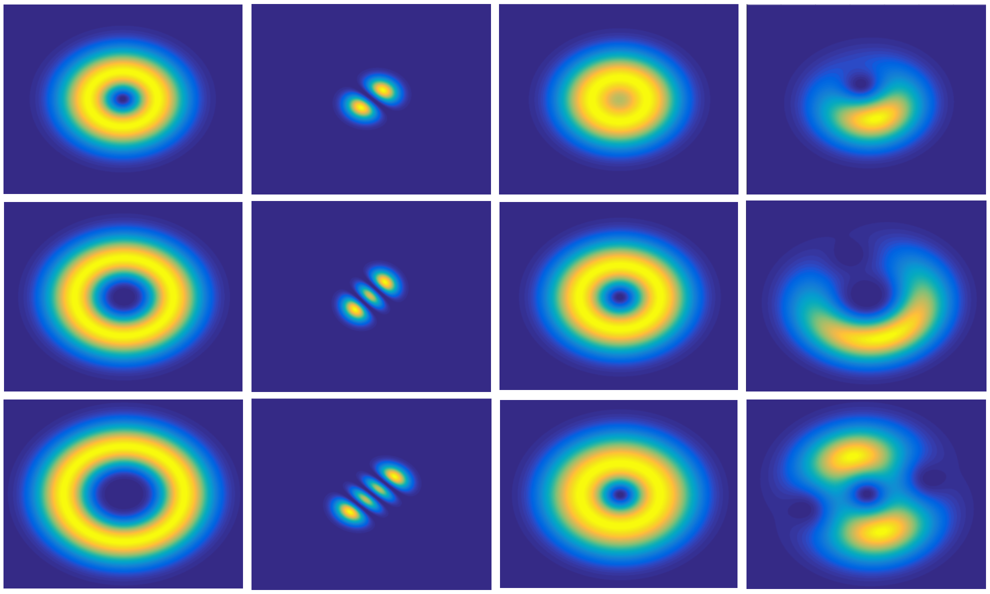

Figure 4.1: Transverse intensity distribution of OVs (color online). First column - pure OVs with $l = 1$ (top); $l = 2$ (middle); $l = 3$ (bottom). Second column - pure OVs at the focal plane of tilted lens with $l = 1$ (top); $l = 2$ (middle); $l = 3$ (bottom). Third and fourth columns - incoherent and coherent mixed states with 50% of each component in every OV, correspondingly, $\mathrm{LG}_{00} + \mathrm{LG}_{01}$ (top); $\mathrm{LG}_{01} + \mathrm{LG}_{02}$ (middle); $\mathrm{LG}_{01} + \mathrm{LG}_{03}$ (bottom).

is possible to detect it by observing the OV's transverse profile, the so called off-axial vortex [113]. However, the detection of incoherent mixtures by observing the transverse profile is less obvious. Examples of coherent and incoherent mixtures $\mathrm{LG}_{00} + \mathrm{LG}_{01}$, $\mathrm{LG}_{01} + \mathrm{LG}_{02}$, $\mathrm{LG}_{01} + \mathrm{LG}_{03}$ are illustrated in Fig. 4.1. As has been shown by Khonina et al. in [114], coherent superpositions have characteristic “chamomile-shaped" transverse intensity distribution profiles. Several algorithms are known to analyze the composition of mixed OAM states. Some techniques based on exploiting diffractive optical elements (DOE) have also been developed to separate OVs with different TCs in free-space. These techniques utilize the property of beams composed of components with different OAMs to “drift" from the optical axis at different distances [115, 114, 116, 117]. The use of a multistage method to determine the TC of a single photon is also possible; this method is based on using rotated dove prisms and a Mach-Zehnder interferometer in each stage [118]. In this letter, our group aims to study the applicability of the tilted lens technique, which is fairly simple in use and does not demand the separation of different components in space, to detect a mixed OAM state.

The possibility of analyzing the composition of this state and distinguishing between coherent and incoherent mixed states is also investigated and discussed.

4.2 Theory

Mathematically, an optical vortex beam propagating along the z axis in cylindrical coordinates (also known as a Laguerre-Gaussian or LG beam) can be represented by a complex field:

$$\begin{aligned} E(\rho, \phi, z, t) =& E_0 \frac{w_0 \rho^{|l|}}{w^{|l|+1}} \exp\left[\frac{-\rho^2}{w^2}\right] \\ & \times \exp[-i(|l|+1)\arctan\frac{z}{z_R} + \frac{ik\rho^2}{2R(z)} + i(l\phi + kz - wt)] \end{aligned} \tag{4.1}$$

where ρ, ϕ are polar coordinates in the transverse plane; w_0 is the radius of the beam at the beam waist (at $z = 0$); E_0 is amplitude parameter; $w = w_0(1 + z^2/z_R^2)^{1/2}$ is the transversal beam radius; $z_R = kw_0^2/2$ is the Rayleigh range; $R(z) = z(1 + z_R^2/z^2)$ is the radius of the wavefront curvature; l is the value of the TC; k is the wavenumber [58]. The complex amplitude of an OV at the beam waist in Cartesian coordinates can be written as follows:

$$E(x, y) = (x \pm iy)^l \exp[-\frac{x^2 + y^2}{w_0^2}] \tag{4.2}$$

At a certain distance from the beam waist in the presence of an astigmatic lens, a higher order OV breaks into $|l|$ secondary first-order vortices [119, 112]. In the transverse plane at this distance there will be $|l| + 1$ intensity peaks, oriented at a $\pm$ 45 angle relative to the tilt axis [103]. The propagation dynamics of an OV in the presence of a tilted spherical lens can be simulated using a ray transfer matrix analysis and generalized Huygens-Fresnel integral, as related in detail in [47]. In the end, the complex amplitude may be described as:

$$E = f_1 \exp[-(f_2 x^2 + f_3 y^2)] H_l(f_4 x^2 + f_5 y^2) \tag{4.3}$$

where x,y are transverse Cartesian coordinates. f_1, ... f_5 are the complex functions of θ (tilt of the lens), z, z_0 (distance from the waist plane to the tilted lens), f (focal distance of the tilted lens) and w_0, described as follows:

$$f_1 = \frac{i}{2}^{m+1} \frac{k w_1 w_2 (w_1^2 - w_2^2)^{m/2}}{(b_1 b_2)^{1/2}}; \tag{4.4}$$

$$f_2 = \left(\frac{k w_1}{2b_1}\right)^2 + i\frac{k d_1}{2b_1}; \tag{4.5}$$

$$f_3 = \left(\frac{k w_2}{2b_2}\right)^2 + i\frac{k d_2}{2b_2}; \tag{4.6}$$

$$f_4 = \frac{k w_1^2}{2b_1 (w_1^2 - w_2^2)^{1/2}}; \tag{4.7}$$

$$f_5 = \frac{i \text{sign}(l) k w_2^2}{2b_2 (w_1^2 - w_2^2)^{1/2}}. \tag{4.8}$$

Where:

$$b_1 = z_0 + z - \frac{z z_0 \sec\theta}{f} \tag{4.9}$$

$$b_2 = z_0 + z - \frac{z z_0 \cos\theta}{f} \tag{4.10}$$

$$d_1 = 1 - \frac{z_0 \sec\theta}{f} \tag{4.11}$$

$$d_2 = 1 - \frac{z_0 \cos\theta}{f} \tag{4.12}$$

$$w_1^2 = \frac{2b_1 w_0^2}{2b_1 + ik(1 - \frac{z}{f}\sec\theta) w_0^2} \tag{4.13}$$

$$w_2^2 = \frac{2b_2 w_0^2}{2b_2 + ik(1 - \frac{z}{f}\cos\theta) w_0^2} \tag{4.14}$$

At this point, the complex field is simply an elliptic Gaussian field modulated by a Hermite polynomial [47]. For a mixed OAM state, the complex field is a superposition of n fields:

$$E = AE_{l_1} + BE_{l_2} + CE_{l_3} + ... + DE_{l_n} \tag{4.15}$$

where l_1, l_2,l_3,...l_n are topological charges corresponding to each field, and A, B, C, ... D are the weight coefficients for each field. In this letter, we consider the superposition of two fields,

$$E = AE_{l_1} + BE_{l_2}. \tag{4.16}$$

However, it is easy to extend this theory to the superposition of three or more fields. The intensity of the resultant field superposition can be found as follows:

$$I = |E|^2 = A^2|E_1|^2 + B^2|E_2|^2 + \alpha(ABE_1E_2^* + ABE_2E_1^*) \tag{4.17}$$

The third term represents the coherent contribution to the intensity distribution, where α is a positive numerical coefficient signifying a degree of coherence between 0 and 1. There are three cases for this superposition: 1) completely incoherent ($\alpha = 0$, keeping only 1st and 2nd terms); 2) completely coherent ($\alpha = 1$, keeping all terms); 3) partially coherent ($0 < \alpha < 1$). This work focuses on the first and second cases because one can imagine the third case as a linear combination of the first two cases. We calculate the intensity distribution near the focal point of a tilted lens with the complex field Eqn. 4.3 plugged into Eqn. 4.17. We perform this calculation for several mixed OAM states: $\mathrm{LG}_{00} + \mathrm{LG}_{01}$, $\mathrm{LG}_{01} + \mathrm{LG}_{02}$, $\mathrm{LG}_{00} + \mathrm{LG}_{02}$, $\mathrm{LG}_{01} + \mathrm{LG}_{03}$, $\mathrm{LG}_{00} + \mathrm{LG}_{03}$ and $\mathrm{LG}_{01} + \mathrm{LG}_{04}$. The results for all cases are depicted in Fig. 4.2.

In this figure, we investigate the one-dimensional intensity distribution along the $+45$ direction in the transverse plane of the optical vortex. As can be seen from Fig. 4.2, the mechanisms for the coherent and incoherent additions of any mixed OAM state act differently (particularly as affects the transverse intensity distribution evolution near the focal spot of a tilted lens for variable weights of components) for the case of $\mathrm{LG}_{00} + \mathrm{LG}_{01}$, $\mathrm{LG}_{01} + \mathrm{LG}_{02}$, $\mathrm{LG}_{00} + \mathrm{LG}_{03}$, $\mathrm{LG}_{01} + \mathrm{LG}_{04}$ but not in the case of $\mathrm{LG}_{00} + \mathrm{LG}_{02}$ and $\mathrm{LG}_{01} + \mathrm{LG}_{03}$. Indeed, for all the states that we included in the Supplementary Materials, it is not the TC of each component which plays a significant role in this evolution, but the difference between the TCs of each component (Δl) which does. In other words, let us take any mixed OAM state with two components such that the difference between them equals 1. Then, for every such mixed state, the left/right peak will split into two in the coherent case and an additional peak will emerge from the center in the incoherent case (see Fig. 4.2, (a)). Meanwhile, for any combination with $\Delta l = 2$, we will get no difference between the coherent and incoherent cases – each of the two outside peaks will split into two (Fig. 4.2, (b)).

Hence, we note that different evolutionary mechanics for coherent/incoherent addition of states are at play for TC differences equal to 1 and those equal to 2. This difference extends to other cases of Δl as well ($\Delta l = 3, 4, ...$ each have their own evolution). Further examples to support our assertion are available in the Supplementary Materials. We also can conclude that by observing the transverse intensity distribution, we can detect the mixed OAM state and distinguish between coherent and incoherent cases. Moreover, it can be seen from Fig. 4.2 that the tilted lens technique is insensitive to the perturbations (up to $\sim 30\%$) around a pure state and indicates only the dominant component of a mixed state.

Finally, we find that the tilted lens technique can distinguish between different ratios of “mixedness" in the mixed states, but only by measuring the relative intensities of each peak in the transverse intensity distribution. Particularly in the cases when an equal amount of each TC component is present, the intensity distribution largely deviates from the ideal case – the peaks can no longer be clearly distinguished in some cases, while in others they are so small as to be barely visible.

4.3 Experiment

A schematic of the experimental setup is shown in Fig. 4.3. The beam from a CW He-Ne laser (~ 0.7 mW, 632 nm) was split by a 50x50 beam splitter into two equal components. After splitting, each component was shaped into a pure OAM state by an SLM (Hamamatsu x10468-02). After traveling $z_0 = 2$ m from the laser output plane, which we considered to be the beam waist plane [120], the beams were recombined coherently or incoherently to create a mixed OAM state. In the “incoherent" mixing case, there were several measures taken to minimize coherent interference. For example, one beam was delayed by longer than the coherence length with respect to the other (but care was taken to keep the diameter of both vortices nearly equal) and a polarizer was used to ensure that the polarizations of the two beams were crossed, further preventing interference. In the coherent case, the same experiment was carried out without delaying the second component or

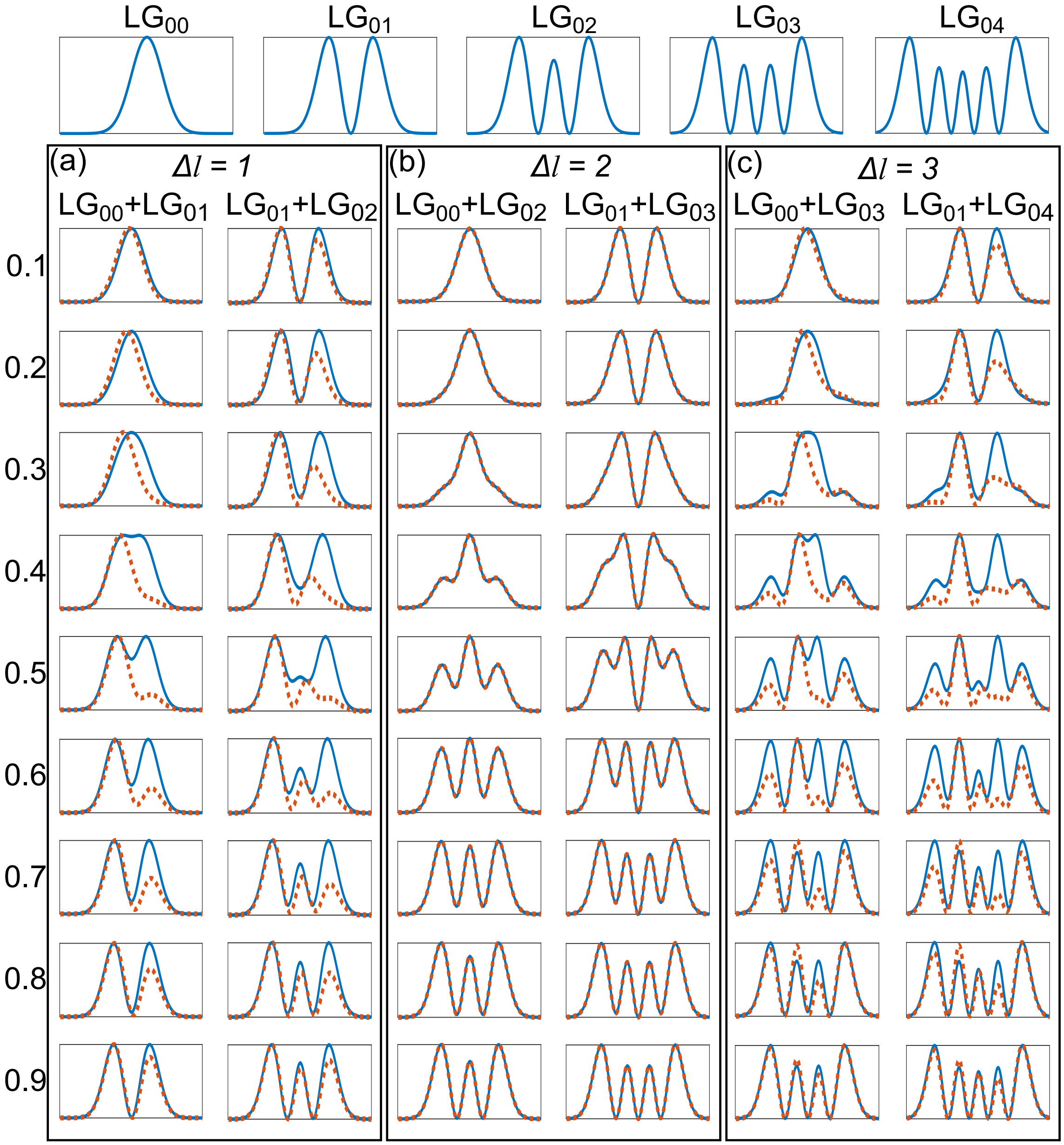

Figure 4.2: Theoretical intensity distribution near the focal point of a tilted lens along the $+45$ direction in the transverse plane of the optical vortex for mixed OAM states. The numbers on the left signify the weight of the component with the highest topological charge. Top-most graphs indicate pure OAM states for LG_{00} (Gaussian beam), LG_{01}, LG_{02}, LG_{03}, and LG_{04}. The three boxes - (a), (b), (c) - show the cross section of the intensity evolution of the mixed OAM states with different values of Δl, varying the weight coefficients of each OV in the mixed state. The blue solid line indicates the incoherent addition of two components of the state, the orange dotted line indicates coherent addition (color online). (a): in the coherent case, as the amount of LG_{01} (LG_{02}) increases, the right peak starts to decrease, moves left and splits into two at the point of equality of each component so that in the end (a nearly pure state) the intensity distribution is indistinguishable from that of LG_{01} (LG_{02}); for the incoherent addition the intensity evolution is symmetric and the middle peak appears in-between the two initial ones. (b): coherent and incoherent addition are indistinguishable. (c): additional peaks emerge from the left and right from the center peak, which remains almost unchangeable.

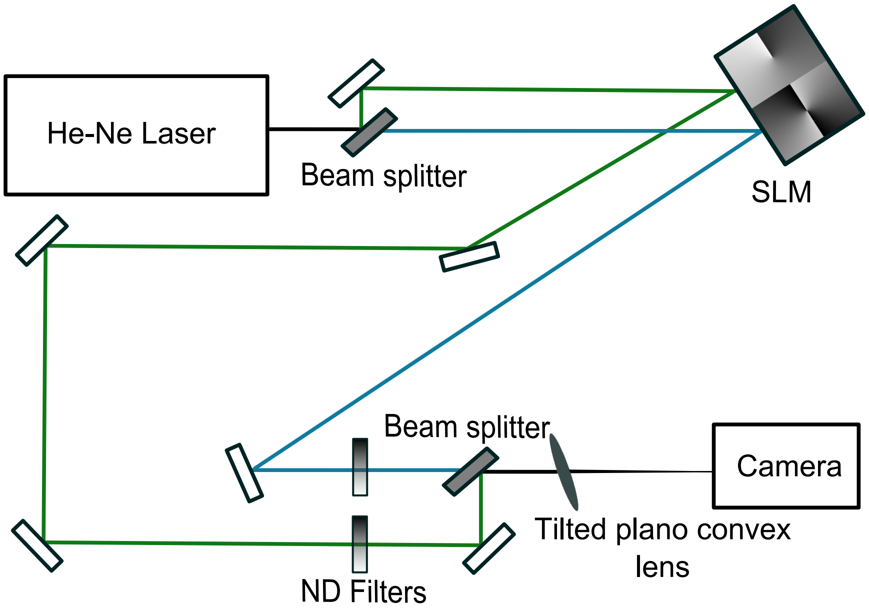

Figure 4.3: Experimental setup for measuring the topological charge of mixed OAM states. The angle of the SLM is greatly exaggerated (color online).

using a polarizer.

In all cases, the recombined beam was then focused by a tilted (at an angle $\theta \approx 11$) convex lens of focal length $f = 20$ cm in the manner described in the introduction. The results were then collected by a beam profiler (Spricon SP-620 U) near the focal point of the lens ($z \approx f \approx 20$ cm). Variable neutral density (ND) filters (Thorlabs NDC-50C-4M) were used to change the relative intensities of each component. These results are summarized in Fig. 4.4. For clarity, experimental results are depicted along with the theoretical two-dimensional intensity distributions; good agreement between simulation and experiment can be seen from these results.

4.4 Discussion and Conclusion

The results of our theoretical and experimental work show that the tilted lens technique can be used to detect a mixed OAM state (superposition of two components). As shown in Fig. 4.4 for $\mathrm{LG}_{01} + \mathrm{LG}_{02}$, both in the coherent and incoherent cases the experimental implementation of the tilted lens technique showed all of the theoretically predicted principal differences between coherent and incoherent addition of components (the splitting of one spot for coherent addition

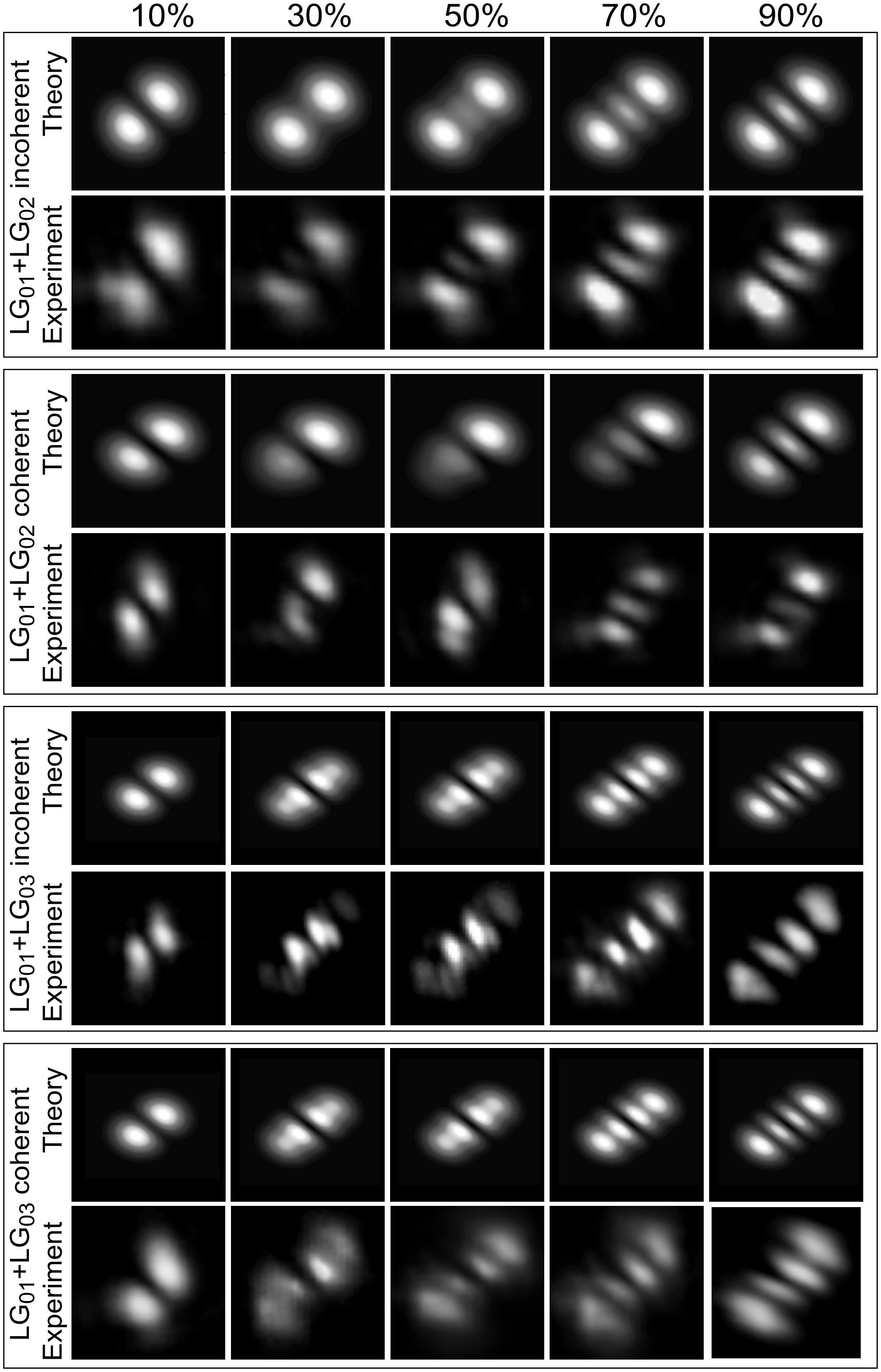

Figure 4.4: Intensity distribution near the focal point of the tilted lens for mixed OAM states; the relative intensity of the optical vortex with the highest topological charge is indicated.

and the emergence of a third spot in between the central two for incoherent addition). Moreover, this technique may be used to analyze the composition of the beam by observing the evolution of the transverse intensity distribution without the separation of different components in space when both components have relatively equal weight coefficients. We have shown that the experimental intensity distribution is consistent with that calculated using Eqn. 4.15. For relatively pure OAM states (dominant component is 70% or more) the technique yields the TC of the dominant component of the beam. When the beam contains several (two or more) components with equal intensity, the tilted lens technique detects a mixed OAM state and shows whether coherent or incoherent addition of the components is present. In this case, a deeper analysis or an alternate technique discussed in the Introduction to this letter is needed to obtain the TC for such a mixed OAM state.

To summarize, the tilted lens technique is easy technique which can be practically used for detecting mixed OAM state, although, it cannot be used to determine the TC and weight coefficient of every component of this mixed state, but it can show that a certain OAM state is not pure and may contain several equal components with different topological charge. This fact can be used as a starting point for applying other, less simple algorithms mentioned above to analyze the composition of the beam and to determine the OAM of the whole beam. Moreover, we conclude that the resultant TC determined with this method is rather insensitive to the interference between components and gives the same number of spots (intensity peaks) in the cases of interfering and non-interfering components. However, the mechanism for the evolution of these peaks and their respective intensities is very different in the cases of coherent and incoherent addition. Hence, a separate treatment is needed for each case.

5. COHERENT RAMAN GENERATION CONTROLLED BY WAVEFRONT SHAPING*

5.1 Introduction and background

Broadband coherent Raman generation results from molecular modulation in Raman-active media [121]. This process provides a promising way towards the synthesis of sub-cycle pulses of coherent light covering the ultraviolet-visible-near infrared range (UV-VIS-NIR) [122, 80, 123, 124]. This source is ideal for studying ultrafast processes in atoms and molecules. Moreover, molecular modulation allows for the possibility of sub-cycle pulse shaping for visible wavelengths. This gives a unique opportunity for optical arbitrary waveform generation (OAWG), which stands as a long term goal for physicists since the invention of the laser [125, 126, 127] and is essential for quantum control of chemical reactions [128, 129].

To initiate the coherent Raman generation one needs to prepare a state of molecular coherence in the medium. It can be done using two optical laser fields (pump and Stokes) which frequency difference matches the vibrational frequency of the Raman-active medium. During this process, a vibrational superposition state is created and all the molecules in any small subvolume vibrate in unison. The phases of this vibration correspond to a coherence wave driven by the applied laser fields. The coherent vibrations, in turn, modulate the fields to produce spectral sidebands shifted by the Raman frequency. When the phase-matching conditions are satisfied the Raman generation process goes efficiently and cascades to generate multiple mutually coherent Raman sidebands. These sidebands are equidistant in the frequency domain (separated by the Raman shift) and cover the whole NIR-VIS-UV region. The vibrational coherence wave is then driven by a combination of all fields, applied and generated.

Typically the phase-matching conditions for the process above are relieved in gases in the near-UV, VIS and NIR regions of the spectrum as the chromatic dispersion is negligible for the wavelengths far from electronic and vibrational resonances. The generated Raman spectra can

---

*Part of this chapter is reprinted from "Coherent Raman Generation Controlled by Wavefront Shaping." Shutova, Mariia, Anton D. Shutov, Alexandra A. Zhdanova, Jonathan V. Thompson, and Alexei V. Sokolov, Scientific reports 9 (2019). copyright 2019, under Creative Commons licence https://creativecommons.org/licenses/by/4.0/.

be adjusted to produce ultrashort pulse or tailored for various purposes. For example, Katsuragawa's group proposed and experimentally demonstrated the possibility of tailoring relative phase relationships among high-order sidebands by using transparent plates with adjustable thickness and position, thereby achieving remarkable spectral control over the sideband generation process [130, 131]. At the same time, in highly dispersive media (crystals [132]) fulfilling the phase-matching conditions is important for producing Raman sidebands efficiently [133, 134, 135]. Overall, these conditions depend on factors such as the refractive index at each of the wavelengths involved, the crossing angle between the two input laser beams, and the interaction length in the Raman medium [79]. With multiple laser fields affecting the phase of the molecular coherence, and then interacting with it to produce polarization waves, the phase-matching conditions may become quite complicated. In the cascaded Raman process the crossing angle between pump and Stokes affects the efficiency and direction of the generated anti-Stokes sideband (AS1); then, the AS1 angle affects AS2 and so on. Therefore, when a high-order sideband is generated, the generation process involves a range of crossing angles, which becomes difficult to optimize simultaneously. In essence, this work addresses the optimization problem mentioned above. As a result we show that optimal generation can be achieved not with a single one, but with a tailored set of $\vec{k}$-vector components/angles within the adaptively shaped pump beam.

Previously Zhi $et\ al.$ theoretically showed that the crossing angle variations are expected to alter the phase-matching conditions and cause a spectral shift of the generated AS sidebands[79]. Liu $et\ al.$ experimentally showed that the phase-matching angle affects the center wavelength of the individual sidebands [133]. Shon $et\ al.$ [136] theoretically showed the possibility to tune phase-matching conditions to a different regimes for solid hydrogen. By optimizing the crossing angle between input fields and the interaction length, the input field can be converted either to broadband sidebands generation or to a single high-order sideband. Above works indicate that the phase-matching conditions for noncollinear cascaded Raman generation in highly dispersive media are nontrivial and need further theoretical and experimental study.

With the development of liquid crystal based phase-only spatial light modulators (SLMs) [3] it became possible to realize various adaptive optics algorithms [5, 6] that help to focus light through turbid media [7, 10, 11], to tailor spectrum of supercontinuum generated in a sapphire plate [12], to enhance Raman scattering signal [13], or to improve contrast of coherent anti-Stokes Raman scattering (CARS) microscopy [17]. In addition, Thompson $et\ al.$ showed [14] theoretically and experimentally that the efficiency of second harmonic generation can be enhanced by using wavefront correction algorithms. In the work of Tzang $et\ al.$[15] the authors demonstrated the ability of adaptive optics to control the stimulated Raman scattering (SRS) and four wave mixing (FWM) processes in multimode fiber. They use wavefront shaping of input beams to control the superposition of modes coupled into the fiber. This allows them to manipulate the spectra and intensities of the generated sidebands, i.e. suppressing, enhancing or shifting them.

We extend the above ideas and develop an approach for the optimization of coherent Raman generation with an adaptive wavefront correction. We apply the continuous sequential algorithm with spiral out geometry [9] to one of the optical fields that drive Raman generation. We set the peak intensity within a spectral range covering one higher order sideband (for example AS10) as the target for the optimization algorithm. As a result of this optimization, accomplished by adjusting the beam profile, we increase the intensity of all high-order Raman sidebands and extend the total bandwidth of the generated spectrum. Broad coherent Raman spectrum is of use for ultrashort pulse production, which can be done by overlapping the generated sidebands and adjusting their relative phases to compensate for delays gained as a result of the dispersion [137, 135, 138, 139, 140]. Spectral bandwidth in this case defines the resultant length of the produced ultrashort pulse.

5.2 Results and discussion

5.2.1 Extending the spectral bandwidth

In this set of experiments, we generate multiple Raman sidebands using two chirped femtosecond laser pulses. We can set the algorithm to increase/suppress the peak intensity of any chosen spectral region. We pick the spectral region so that the center wavelength of the desired sideband will fall within this region (see "Methods" section for the experimental details). We choose AS10 (570 nm), because it is the highest order sideband generated under our experimental conditions. We set the adaptive algorithm to maximize the peak intensity in the spectral region of 550-600 nm. The ratio of current signal to the initial signal on the spectrometer for each iteration is depicted in Fig. 5.1a. Each iteration corresponds to the phase optimization of one particular pixel on the SLM array. Several sharp leaps on the graph show that a significant intensity enhancement corresponds to the phase optimization of several individual pixels on the array. Sharp leaps occur due to the phase difference between certain neighboring pixels, which may drastically alter the resultant beam profile (refer to "Methods" section for the details of the optimization algorithm). After optimization, AS10's intensity is enhanced by a factor of 13 (150^{th} iteration).

Albeit we can select various spectral regions for any optimization goals affects all sidebands and not only selected one. We cannot enhance or suppress one sideband without affecting the others; on the contrary, the optimization affects Raman generation overall.

To confirm the overall enhancement we measure the average power of each sideband (Fig. 5.1b). The optimized total power is $\sim 20\%$ higher than the initial. We see that the power of AS4-AS10 (675-570 nm) sidebands has increased, moreover, the two new higher order sidebands AS11 (558 nm) and AS12 (548 nm) have emerged. Figure 5.1c shows the comparison of two generated spectra before and after optimization; the spectral broadening and overall brightness increase can be easily seen by eye.

Figure 5.2 shows that after the optimization of AS10, the Raman generation spectra has changed significantly. The linear and nonlinear parasitic scattering near the fundamental laser wavelength has decreased and the center wavelengths of mid- and high- order sidebands have changed.

5.2.2 Interpretation and simulation

Figure 7.5a shows that the adaptive optics algorithm finds the appropriate phase and intensity beam profile to optimize the conditions for the high-order sideband generation. This phase-intensity profile affects the experimental system in several ways.

First, it affects the beam shape and position at the nonlinear interaction area. To quantify this

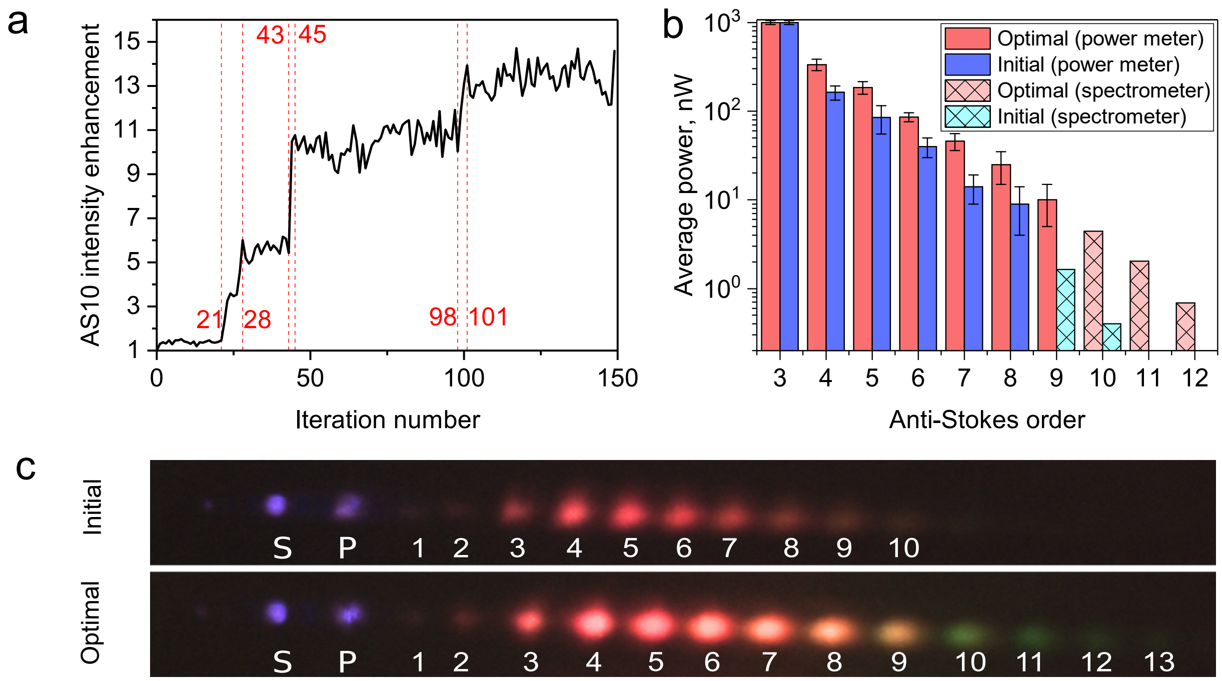

Figure 5.1: a: AS10 intensity signal detected after every iteration during the optimization process. The graph is normalized by the initial (not shaped) value of the intensity. Red dashed lines show the iterations with the highest increase of intensity on the spectrometer. b: Average power of sidebands with (blue columns) and without (red columns) wavefront shaping, measured with a photodiode power meter. Initial AS9, as well as all of AS10-AS12 powers were below the sensitivity limit of the power meter. Solid columns represent the data taken with the photodiode sensor (power meter) and the plaid columns represent the integrated spectra taken with the calibrated spectrometer. The spectra were integrated over each individual sideband. c: Picture of the row of generated sidebands on a white screen. Top - before optimization, bottom - after optimization; P - pump beam; S - Stokes beam; numbers 1-13 denote orders of generated AS.

effect we can roughly estimate the beam profile numerically, using Fourier optics. For this, we perform a simulation with PROPER Matlab libraries [141], based on Fourier transform algorithms [142]. The Gaussian profile with the phase-correction (obtained experimentally, Fig. 7.5a, first column) undergoes the focusing with the lens. Last column in the Fig. 7.5a shows the obtained beam profile at the imaging plane (the focal plane of the lens). Although, these simulations come with some caveats because the wavefront distortion added by the SLM smears out the Gaussian mode of light, so that the beam profile varies with the propagation distance. Fourier optics gives us information about the distorted beam profile only at the focal plane. However, we are interested

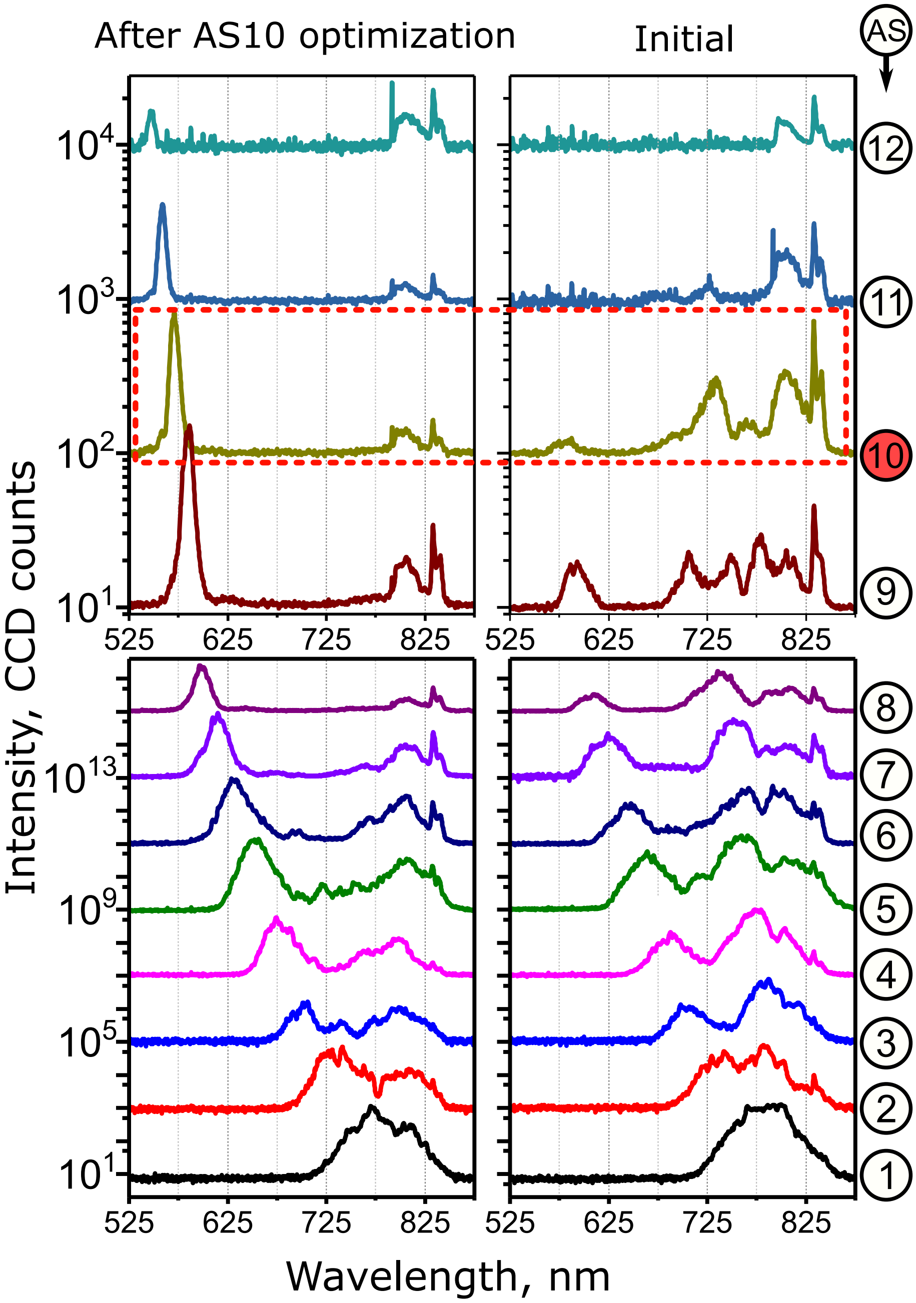

Figure 5.2: Spectra of the generated Raman sidebands before (right) and after (left) optimization, with the goal to maximize intensity of AS10 (highlighted with red dashed rectangle). Numbers on the right correspond to the order of the anti-Stokes sideband (AS1 - AS12). Each individual sideband is spatially separated from the others and focused tightly into the calibrated spectrometer with the help of spatio-spectral filter (see "Methods" for the experimental details). The multiple measured spectra are plotted with a 20 dB (bottom) and 10 dB (top) offset.

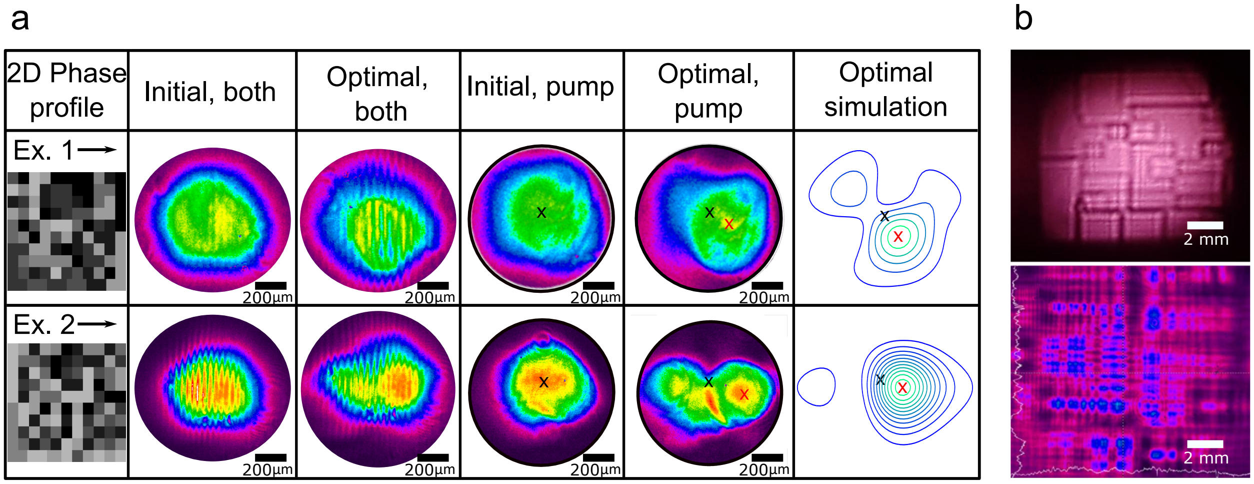

Figure 5.3: a: SLM phase-masks for the two representative examples of optimization with different beam alignments. Top row - Example 1 (corresponds to the data presented in Fig. 5.1), bottom row - Example 2. Columns show the spatial phase profile after optimization; beam profiles before and after optimization (the images correspond to beam profiles on the surface of the crystal, ~ 2.5 cm before the focal plane of the focusing lens). "Both" denotes the profile of overlapped pump and Stokes beams. Contour graphs depict simulated beam profiles at the focal plane of the focusing lens after optimization. Black and red X-es indicate the beam intensity maxima before and after optimization correspondingly. The pump-Stokes crossing angle after optimization is decreasing for Ex.1 by $\sim 0.04°$, for Ex.2 by $\sim 0.1°$. In addition black X-es indicate the center of Stokes beam in all cases. Sizes are not to scale. b: An example of optimized beam profile as seen on the white screen (top) and as measured by the beam profiler (bottom) in the near-field zone of the SLM.

in the imaging plane located 2.5 cm before the focal plane (2 and 3 columns of the Fig. 7.5a, due to location of the nonlinear interaction area in the experiment). Nevertheless, we see similarities in the simulated (4 column) and experimentally obtained beam profiles (3 column), which adds to the understanding of the effect produced by generated phase profiles. On the other hand, the spatial structure of the generated AS beams does not become complex after the optimization, which is a benefit for ultrashort pulse synthesis.

Second, in the most of the experiments, the center wavelength of mid- and high-order sidebands is shifted after the optimization (see Table 5.1). This serves as a good indicator of the crossing angle change [79, 133]. To fully understand the pump-Stokes "crossing configuration" we consider a typical example of the beam profile in the near-field region of SLM (Fig. 7.5b). It shows the overall complicated picture of the pump beam wavefront, where each intensity maximum has a

Table 5.1: Experimentally measured center wavelengths of generated Raman sidebands AS3-AS12 before and after optimization

AS order	AS3	AS4	AS5	AS6	AS7	AS8	AS9	AS10	AS11	AS12
Before optimization, wavelength, nm	710	687	665	646	624	611	592	583	-	-
After optimization, wavelength, nm	706	675	653	629	615	596	586	570	558	548

different phase. This picture represents the space of multiple pump wave vectors ($\vec{k_{pi}}$), each of these vectors contributes to the final superposition ($\vec{k_p} = \sum_{i=1}^{n} \vec{k_{pi}}$) and affects the final phase-matching for generated sidebands [136].

To track capabilities of the adaptive algorithm to change the phase-matching picture, we need to estimate the overall contribution of each small pixel into the final $\vec{k_p}$ state, and the role this $\vec{k_p}$ plays in generation of n-th AS. This problem is very complex, not only because the phase matching conditions for n-th AS depend on, (n-1)-th AS, but also because of the optimization process is different for each experiment. It depends on the sideband chosen for the optimization and on the experimental alignment.

Nevertheless, we can estimate the crossing angle change for the AS1 generation (the simplest case, dependence only on one pump-Stokes beams orientation). The phase-matching conditions can be seen from the equation for the phase mismatch factor for Raman generation [75]:

$$M = sinc^2[(k_R - k_{opt}) \times L/2], \tag{5.1}$$

where $(k_R - k_{opt})$ stands for the wave vector mismatch, $L = 500\mu m$ - the crystal thickness, k_R - the wave vector modulus of the generated Raman sideband, k_{opt} - the wave vector modulus of the generated Raman sideband calculated from the geometrical representation of wave vectors; for example, for AS1:

$$k_{opt} = [4k_p^2 + k_S^2 - 4k_p k_s cos\theta]^{1/2}, \tag{5.2}$$

where k_p and k_S - are the moduli of the wave vectors for the pump and Stokes fields correspondingly. The mismatch factor characterizes the efficiency of Raman anti-Stokes wavelength generation. Ideal phase matching $(k_R - k_{opt}) = 0$ and $M = 1$ in (1) ensures a fixed relative phase between generated anti-Stokes wave and nonlinear polarization and efficient energy extraction from input fields. On the other hand when $0 < M < 1$ the process goes less efficiently.

To estimate the AS1 generation efficiency dependence on the phase-matching angle change quantitatively, we compare the experimentally detected beam positions before and after the optimization by looking at the beam intensity maximum. Using ray optics we calculate that the propagation angle change for various optimizations (different experiments) can be as large as ∼0.1°. Therefore, the difference in the phase matching factor for AS1 for the case $M(2.3°) = 0.76$, $M(2.4°) = 0.91$, (the Sellmeier equation for the refractive index was taken from [143]) is equal to $\delta M = 0.15$. Moreover, the direction of optimized $k_{AS1,opt}$ is changed in comparison with non optimized k_{AS1}.

Next step will be to estimate AS2 generation change after the optimization, because of k_p and k_{AS1} changes, and so on for AS3, AS4 - AS12. This procedure describes step by step the changes produced by wavefront optimization, that significantly affect the high-order sidebands generation. The overall picture ends up being quite complicated. Figure 7.5b shows, in essence, that the generation is optimized by a (non-trivial) combination of pump k-vectors, but not just one optimal k-vector.

5.3 Methods

5.3.1 Optical layout

Our setup is based on the idea of driving molecular vibrations with a pair of time-delayed linearly chirped pulses [86]. The experimental layout is depicted in Fig. 5.4a. We use a Ti:sapphire femtosecond oscillator+amplifier laser system (Coherent Micra, Legend) with Fourier transform limited $\sim$ 35 fs, 3.7 mJ laser pulse (1 kHz repetition rate). We stretch the pulse in time up to $\sim$ 70 fs (spectral width 476 cm^{-1}) FWHM by offsetting the compressor inside the amplifier from optimal position. By doing this we introduce a linear chirp to the pulse and allow the generation of sidebands due to the excitation of the 325 cm^{-1} Raman mode in a $PbWO_4$ crystal [86]. The Raman coherence lifetime for this mode is $T \approx 2.5$ ps [144], excitation occurs in the transient regime $\tau_p \ll$ T, where τ_p denotes the time duration of pump pulse[79].

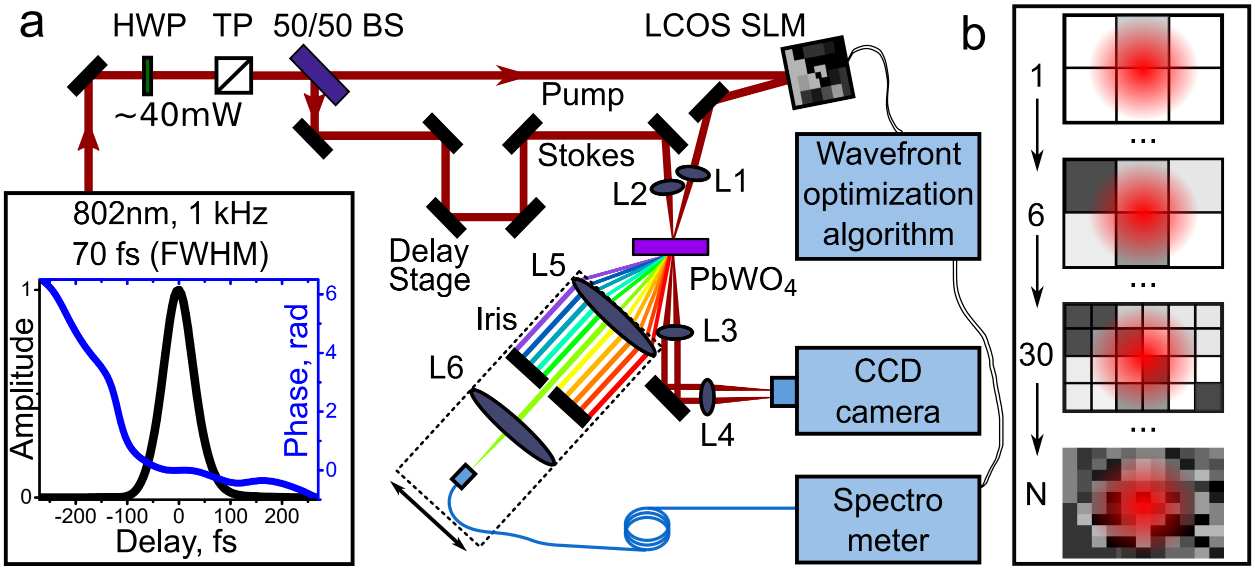

Figure 5.4: a: Experimental setup for optimized Raman sideband generation with feedback-based wavefront shaping algorithm. HWP - half-wave plate, TP - thin polarizer, BS - beam splitter, L1 - L6 are focusing plano-convex lenses. A sample pulse retrieved via SHG FROG is shown in the inset. Optics in dashed square (L5, L6, Iris, spectrometer head) can be moved along the generated Raman spectra for the single sideband spectrum detection. b: Shaping algorithm; the numbers indicate the iteration and the pictures show the SLM screen with the Gaussian beam profile, square blocks depict optimization pixels, and gray color code shows phase variation of phase profile of the beam.

The chirped pulse then passes through a half-wave plate and a polarizer system for attenuation (down to 40 μJ) and more precise polarization control. The pulse is then split by a 50/50 beam splitter. One half of the pulse is used as a pump, the other is used as Stokes. The pump pulse then reflects off of the SLM (LCOS SLM, Hamamatsu X10468-01) and acquires a wavefront modification. The Stokes pulse passes through a retro-reflector on a translator (delay stage) for precise time delay control. Finally, we overlap pump and Stokes pulses in time and space inside the $PbWO_4$ Raman crystal. Both beams are loosely focused by 50 cm lenses L1 and L2 behind the crystal at a $\sim 2.5 \pm 0.5°$ angle (the spot size of the beam on the crystal surface is $\sim$ 600 μm, ~2.5 cm before the focal plane). The average power in each of the two beams incident onto the crystal surface equals to $\sim$ 13 mW. The pump and Stokes pulses overlap in time and space and produce multiple orders of Raman sidebands separated by the Raman shift. We collimate the produced sidebands by 5 cm plano convex lens L5 and use an iris diaphragm to filter out the particular sideband we chose for optimization. The sidebands are focused with a lens (L6, 10 cm focal length) and coupled into the spectrometer's input fiber (multimode, 600 μm core, numerical aperture 0.22, acceptance angle $12.7°$). Convergence angles of the sidebands are small ($\sim 0.31°$), which ensures good coupling. We measure the average power of the sideband with the photodiode sensor (Ophir PD10-PJ-V2, sensitivity limit - 10 nW), not shown. Lenses L3 and L4 image pump and Stokes beam profiles onto the CCD camera.

5.3.2 Spatio-spectral filter

Since the phase-matching conditions for cascaded Raman scattering in crystals are non-collinear, each higher-order anti-Stokes frequency is generated at a certain angle to the previous (lower-order) one and all the generated sidebands are spread out in a horizontal plane. For convenience the sidebands are collimated shortly after the crystal with the lens L5 and lower order sidebands are attenuated by a set of neutral density filters (not shown). To measure the spectrum of each individual sideband, we ensure its separation from all other sidebands with an iris diaphragm and focus the separated sideband with the lens L6 into the fiber spectrometer (Ocean Optics USB2000+). Therefore, the spectrum of each sideband were measured separately to ensure no aberrations by centering it on the lenses (spatio-spectral filter is highlighted with the black dashed square in the Fig. 5.4a). One concern for this configuration is whether the input beam shaping will affect the fiber coupling efficiency. To get reasonable comparison of intensities before and after the optimization, we focus the light tightly into the spectrometer's fiber (diameter 600 μm) to ensure a good, constant coupling efficiency for all spectral components of light.

5.3.3 Wavefront optimization algorithm

The spectrometer and the phase-only SLM are controlled by an adaptive feedback algorithm running in a closed loop fashion. This algorithm is known as an iterative continuous sequential algorithm with spiral out geometry [9] (Fig. 5.4b). Initially, the algorithm splits the SLM screen into blocks of pixels (6 is the minimum number of blocks, Fig. 5.4b1), and varies the phase applied to the 1st block of pixels from 0 to 2π in steps of $2\pi/7$. While doing this, the algorithm detects the signal on the spectrometer within a chosen spectral range for each phase value (Fig. 5.1a). After finishing spectral detection for the 1st block, the algorithm compares the detected spectra, chooses the one that matches with the optimization condition in the best way and memorizes it along with the corresponding phase value for this block. After the 1st block (1st iteration), the algorithm moves to the 2nd block (Fig. 5.4b6). When all blocks are checked, the algorithm divides current blocks into smaller subblocks (Fig. 5.4b30) and does the phase variation and spectral detection again [9]. The algorithm can be manually stopped at any point or when the desired result is achieved (Fig. 5.4bN). The user can choose among several optimization goals, for example: (a) maximize the peak intensity within a certain spectral range; (b) maximize the average intensity within the required spectral range. Any desired spectral range can be specified arbitrarily within the range of the spectrometer.

We have found that careful alignment of the setup is important for our experiments due to the sensitivity of both the wavefront correction technique and cascaded Raman process. We ensure the spatial overlap of the pump and Stokes beams in the crystal and the equality of their diameters and intensities with the beam profiling CCD camera (Spiricon SP620U). We choose intensities that are sufficient for Raman generation while avoiding parasitic effects such as four wave mixing or self-phase modulation. The pump-Stokes frequency difference, their crossing angle, polarizations and beam profiles play an important role in satisfying phase-matching conditions and must be carefully optimized. We measure a temporal chirp and pulse duration with SH-FROG [145] and detect no spatial chirp in the beam according to the references [146, 147].

5.3.4 Detailed AS10 optimization

Figure 5.5 shows the detailed spectra of several sidebands (AS5, AS7, AS10) before and after the optimization of AS10, described above. As we can see in the picture, the intensity of each shown sideband is growing after the optimization and the parasitic signal in the scale of fundamental wavelength is getting smaller.

Figure 5.6 depicts the profiles of the AS1 and AS2 sidebands before and after optimization. After optimization AS1 and AS2 become brighter and smaller in size, which indicates more efficient coherent Raman generation.

5.4 Conclusion and future work

We demonstrate the ability of adaptive optics to increase the intensity of Raman sidebands using the wavefront optimization. We show that the same technique extends the total spectral bandwidth of Raman sideband generation by phase-only corrections to the pump beam profile. The optimization algorithm finds the phase-intensity beam profile which is able to improve the coherent Raman generation. We find that the center wavelengths of the generated sidebands become shifted after the optimization, which can be attributed to the change in the beams crossing angles. We describe the step by step process of phase-matching optimization. The obtained extended spectral bandwidth (and enhanced Raman sidebands) at given total average power is advantageous for generating shorter and more energetic sub-cycle light pulses.

Figure 5.7 is adapted from Ref. [148] shows the experimental setup for synthesis of a single cycle white light pulse by combining four coherent Raman sidebands. We showed that it is possible to get 7fs pulse with this setup. In the future we plan to combine the adaptive optics algorithm with this setup to get more energetic and shorter pulses of light.

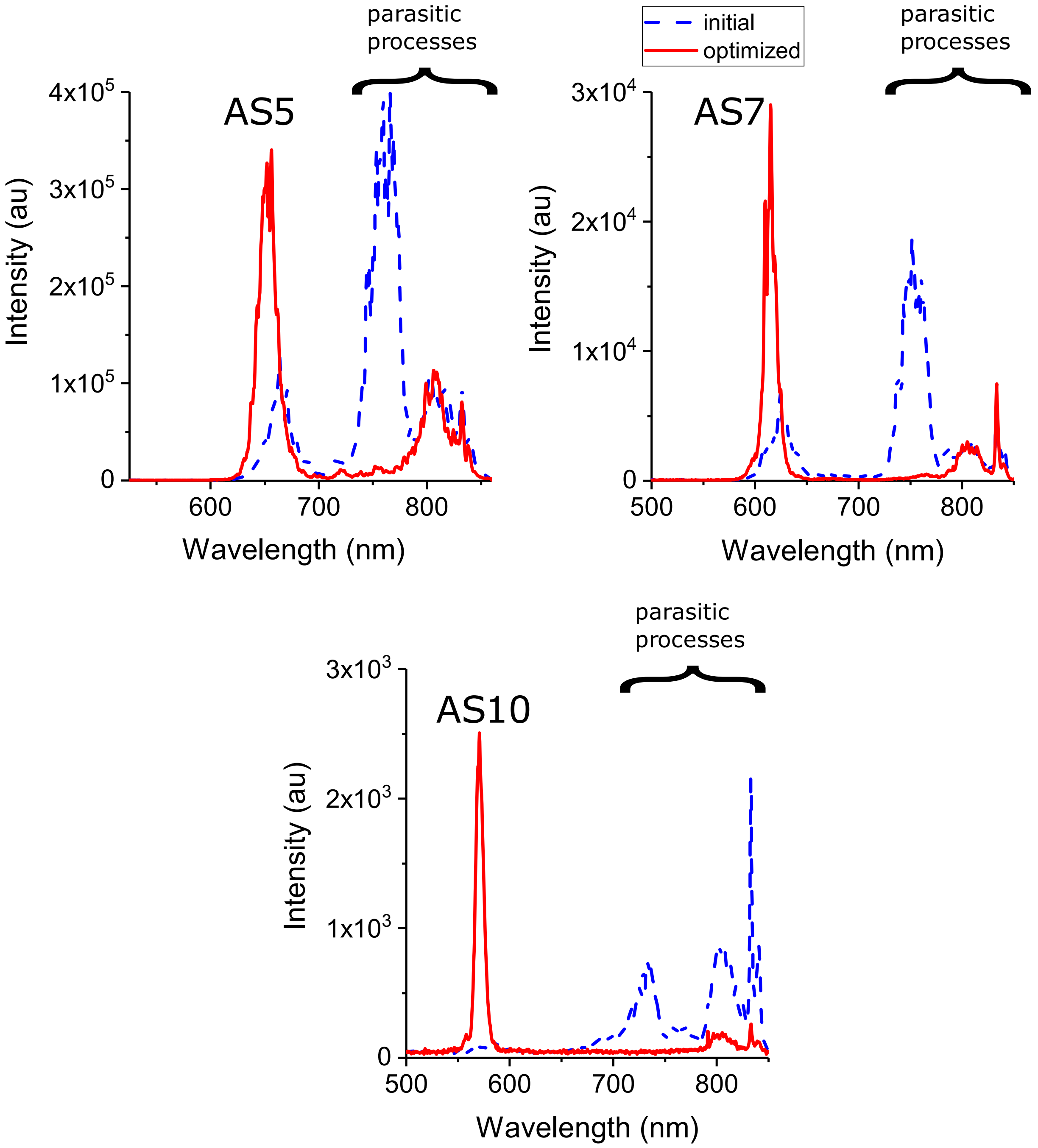

Figure 5.5: AS5, AS7 and AS10 spectra before (blue dashed line) and after (red solid line) optimization. The spectra are the same as in Fig. fig:spectra, but on a linear scale. Initial and optimized corresponding sidebands are depicted on the same graph for clarity.

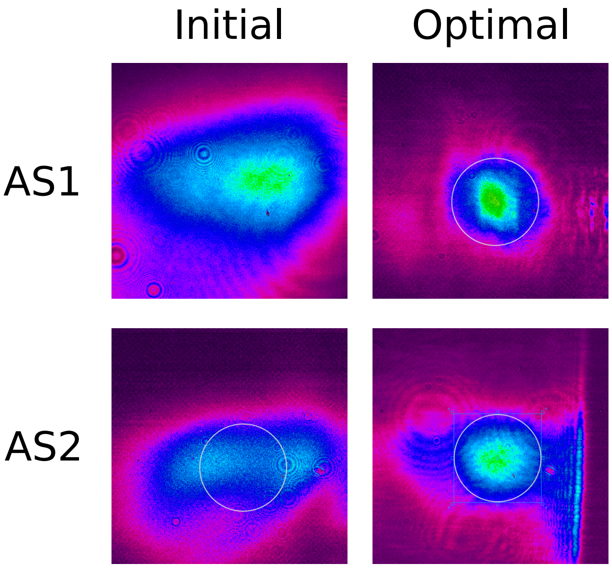

Figure 5.6: AS1 and AS2 beam profiles before (initial) and after (optimal) optimization. Elliptical shape of the initial sidebands can be explained by presence of self diffracted sidebands. These sidebands propagate almost collinear to the low order sidebands due to small wavelength difference. As can be seen from the picture, the spatial structure of the generated sidebands is more round close to a Gaussian.

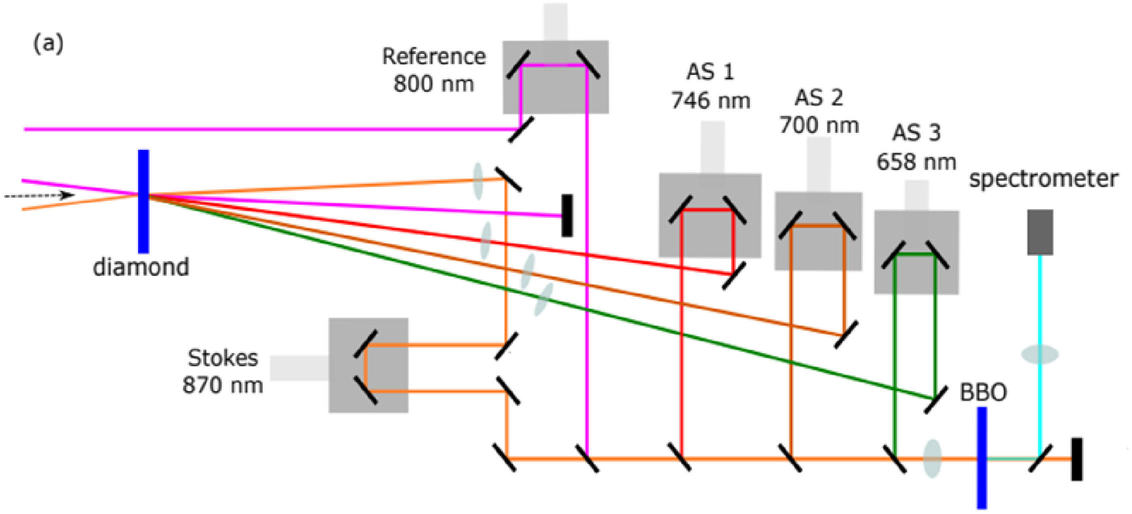

Figure 5.7: Experimental setup modification for collinear synthesis of single cycle coherent white light pulse with dichroic mirrors.

6. BINARY PHASE PLATE FOR HIGH INTENSITY NON-DIFFRACTING HOLLOW BEAM STRUCTURE*

6.1 Introduction

Spatially shaped optical field structures produced with coherent light sources that have circular symmetry and remain constant over significant propagation lengths, often called circular lattices, have attracted growing interest in recent years. Laser beams focused with a conical lens (axicon), an example of such a structure, are well described by a Bessel function of zeroth order. The peak intensity of such a beam is located on the central axis and its diameter remains unchanged providing diffraction-free propagation for a long distance. The distance of diffractionless propagation is determined by the angle of the formed conical beam and its initial size. In contrast, Bessel beams of higher orders consist of a hollow beam with a dark near-axis region. The diameter of such a beam increases with the Bessel function's order number and remains unchanged over a long propagation distance. Bessel beams of high order can be produced by focusing Laguerre-Gaussian (LG) modes with a non-zero azimuthal index [149] using an axicon. The result, which is an example of so called optical vortices, have a spiral wave front with singularities on the axis. It carries an orbital angular momentum (OAM) associated with the LG azimuthal index. The axicon provides a conical wave front which forms a Bessel beam of high order with an associated OAM.

Optical vortices of high orders have numerous applications in advanced inscription methods for optical communication [150, 43, 151], optical tweezers for particle trapping and manipulation in nanotechnology and microbiology [152, 153, 154, 151], and ultrahigh resolution microscopy [155, 151]. Propagation of high intensity optical vortices in nonlinear media shows a rich variety of new phenomena with high potential for the generation of high harmonics, X-ray lasers, acceleration of particles, and creating wave guide structures in plasmas [156, 157, 158, 159, 160, 161, 162, 163]. Hollow beams of high intensity can be used to produce strong imploding shockwaves in condensed

---

*Part of this chapter is reprinted from "Binary phase plate for high-intensity non-diffracting hollow beam structure." Shutova, Mariia, Zack Liege, Alexander Goltsov, Anatoli Morozov, and Alexei V. Sokolov, JOSA B 36, no. 5 (2019): 1313-1319, copyright 2019, with kind permission from the Optical Society.

media [164].

Optical vortices, as well as Bessel beams of high order, can be produced with a mask called a kinoform designed for specific orders [165], computer-generated holograms [166], spatial light modulators (SLM) [167], and spiral wave plates [168, 169]. Variety of specific phase modulating wave plates has been proposed to generate azimuthal, spiral, and petal-like optical filed structures [170, 171]. While different approaches have been developed to design various optical elements based on plane holograms, their efficiency usually does not exceed 50%. Efficiency of refractive spiral elements can be higher; however their fabrication is quite complex and expensive with limited success in formation of Bessel beams of high order. Realization of binary phase masks produces first order diffraction with a maximum theoretical efficiency of 40.5% [172, 173].

In this work, we study an alternative method for producing a hollow non-diffracting beam structure featuring an axisymmetric array of beams using the combination of an axicon and a simple binary phase plate (PP), which can be manufactured with standard photolithography techniques. In contrast to other designs, the proposed PP-axicon (PPA) combination does not lead to significant losses due to diffraction of the input beam; all of the diffracted beam components participate in the formation of a ring profile. Our goal is to create a structure using a femtosecond pulse in a gaseous medium to guide powerful ultrashort laser pulses as a step for the development of X-ray lasers and Raman amplification in plasmas.

We show that a binary multi-sectoral phase plate providing azimuthal π-phase modulation in a collimated beam, combined with an axicon, results in the formation of a pair of co-propagating optical vortices with opposite topological charges. The topological charges are determined by the number of sectors in the PP. The produced diffractionless field structure is well described by a combination of high order Bessel functions. Interference of these two vortices results in formation of a ring of bright spots at the hollow dark region perimeter with 100 % modulation depth.

6.2 Design and numerical simulation of the Phase Plate Axicon converter

The proposed PPA converter combines an axicon and a PP sequentially installed into the axis of a laser beam with a wavelength λ propagating along the z-axis, see Fig. 6.1. It forms a hollow optical field structure which propagates unchanged over a long distance.

We consider a circularly symmetric case, where the PP is divided into an even number of equal sectors, denoted by N. The thickness difference between neighboring sectors provides a π-shift in the transmitted wave front. The PP imprints the following azimuthally dependent phase delay F into the transmitted laser beam [170]):

$$F(\phi, R) = \frac{\pi}{2}[1 + sign(sin\frac{N}{2}\phi)], \quad R > r_0, \tag{6.1}$$

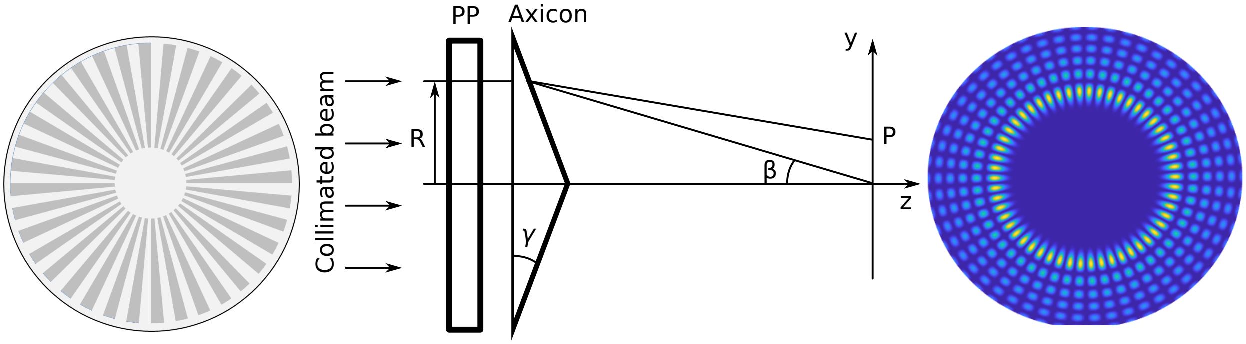

Figure 6.1: a: Schematics of the PPA converter with PP being a phase plate providing a π- shift of the beam transmitted through neighboring radial sectors. An example of the intensity distribution for a PP with 54 sectors is given on the right. The near-axis region of the PP is left blank due to technological limitations and it will be blocked in future experiments with intense laser beam to avoid optical damage.

where N is the number of corresponding sectors, ϕ is the azimuth angle, and R is the radial coordinate, r_0 is the central spot radius that is blocked due to technological limitations. The refracted beam angle $\beta = (n-1)\gamma$, where γ and n are the axicon base angle and the material refractive index, respectively. The intensity distribution on an incidence plane can be calculated with Fresnel integrals. Using the scalar theory of diffraction, we write the laser intensity at an arbitrary point P with polar coordinates (y,α) as follows [174]:

$$I(P(y,\alpha)) = I(R)\ 2\pi\, k\, R\, \frac{sin\beta}{cos^2\beta} \left| \int_0^{2\pi} exp[\, i\, F(\phi) - i\, k\, y\, sin\beta\ cos(\phi-\alpha)\,]\, d\phi \right|^2, \tag{6.2}$$

where, $k = 2\pi/\lambda$ is the wave number. In particular, with $F(\phi, R) = 0$, Eq.6.2 gives the well-known equation for a Bessel beam:

$$I(P(y,\alpha)) = I(R)\ 2\pi\, k\, R\, \frac{sin\beta}{cos^2\beta} \left[J_0(k\, y\, sin\beta) \right]^2. \tag{6.3}$$

An example of the intensity distribution from Eq. 6.2 is plotted in Fig. 6.1, 6.2 for N=54. Interestingly, when the number of sectors is large, i.e. $N >> 1$, the intensity distribution after the converter can be well fit by the function:

$$\frac{I(P(y,\alpha))_{fit}}{I_0} = \left[J_{N/2}\, (y^{(N/2)}\, \frac{y}{R_0}\,)\ sin\frac{N}{2}\,\alpha \right]^2, \tag{6.4}$$

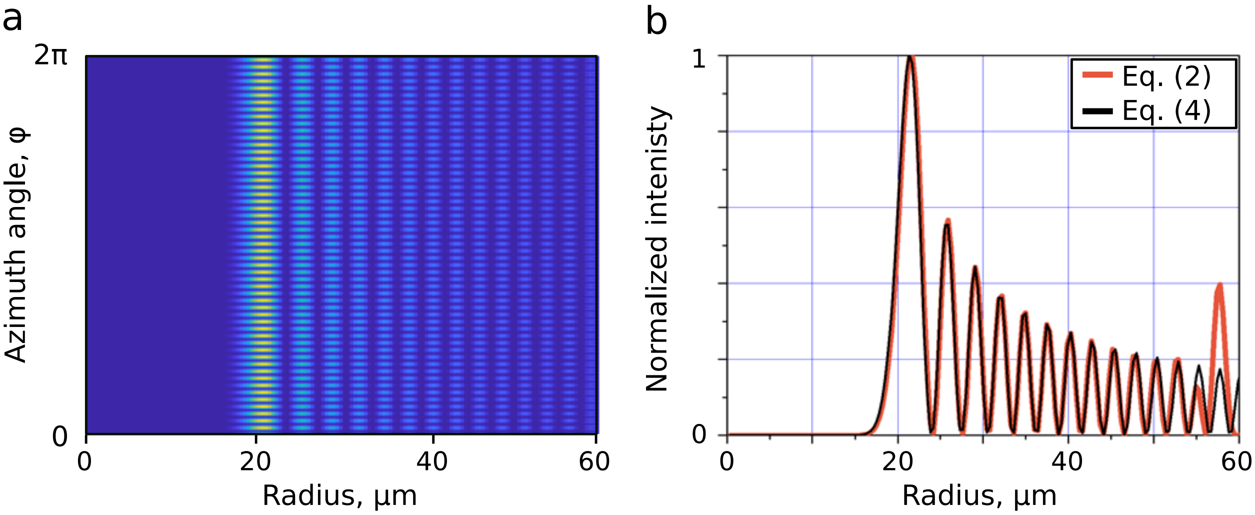

Figure 6.2: a: Intensity distribution after the PPA converter, via Eq.2 for a large number of sectors. Axicon base angle is 20°, $N = 54$, and $\lambda = 800nm$; b: Radial distribution comparison between the fit from Eq. (2) and Eq. (4).

where I_0 is the maximum on-axis intensity which would be produced with the axicon alone (without the PP), $J_{N/2}$ is the Bessel function of the first kind of order of N/2, α is the azimuthal angle, $y^{(N/2)}$ is the radial position of the first maximum of $J_{N/2}$, and $R_0 = y^{(N/2)}/(ksin\beta)$. For the case in Fig. 6.2b the fitting Eq.6.4 works well for first 12 oscillations and then fails for larger radii.

The radial size of the produced hollow structure can be expressed via the radius of the first maximum of the Bessel function of N/2 order $(y^{(N/2)})$,

$$R_{ring} = R_0 = \frac{y^{(N/2)}}{k\,sin\beta}. \tag{6.5}$$

As $y^{N/2} = N/2$ for $N >> 1$, then

$$R_{ring} = \frac{N}{2k\,sin\beta}. \tag{6.6}$$

Note that for the LG modes R_{ring} scales with the square root of N.

According to the fitting from Eq.6.4, the maximum intensity in the produced field structure scales as

$$[J_{N/2}(y^{(N/2)})]^2 \sim N^{-2/3}, \tag{6.7}$$

which stems from the fact that for $N >> 1$,

$$|J_N(y^{(N)})| \sim N^{-1/3}. \tag{6.8}$$

(For any practical value of N these statements can be easily verified by direct calculations.) Using Eq.6.4-6.6, one can calculate the dependence of the PPA performance upon the convergence angle β.

We simulate the intensity distribution after the PPA converter using Eq.6.2. For our simulations and experiments we use an axicon made from fused silica with an apex angle of $140°$ providing for a convergence angle $\beta = 10°$ and assume a laser beam with a flat top intensity distribution. To investigate the performance of the proposed converter, we perform simulations with varying number of sectors, wavelength, duration, and bandwidth of the laser pulse.

Figure 6.3a shows the dependence of the radius of the main ring forming the perimeter of the hollow dark region on the number of sectors N. For $N >> 1$, it is proportional to $N\lambda/sin\beta$, which agrees with the scaling from Eq.6.6. As can be seen from Fig. 6.1, the intensity maxima of the centermost ring are shaped like petals whose radial size ΔR slowly grows with N as $\Delta R \sim N^{1/3}$, while their azimuthal dimension $\Delta\phi$ is proportional to 1/N.

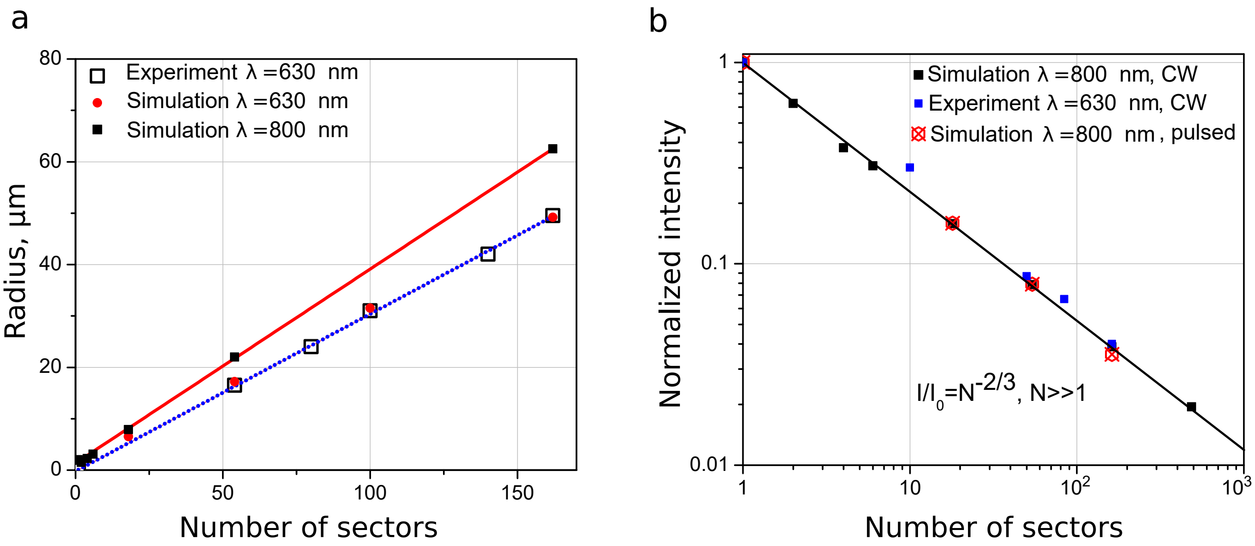

Figure 6.3: a: Radius of the main ring versus the number of PP sectors. Measurements for $\lambda = 0.63$ nm were obtained in experiments with an SLM instead of a PP. b: Intensity maximum of the (PPA) beam normalized to the intensity maximum of the regular Bessel beam (modulated by axicon only) versus the number of sectors. Black squares and crossed red circles show the difference between continuous wave (CW) and pulsed laser for $800nm$ (pulsed laser line bandwidth equals to $33nm$). Blue squares represent experimental data for 630 nm CW experiment.

The energy concentration is determined by the ratio of the intensity maximum in the circular lattice to the on-axis intensity of a zero order Bessel beam, obtained with an axicon standing alone (see Fig. 6.3b). Indeed, the intensity ratio falls with the number of sectors as $N^{-2/3}$ in accordance with the fitting from Eq.6.4, following directly from the fact that $J_N(y^{(N)}) \sim N^{-1/3}$.

The tolerance in the height difference between neighboring sectors on the PP is illustrated in Fig. 6.4a,b. As one can see in Fig. 6.4b, the deviation of the phase delay F from a perfect value of π results in the appearance of additional light in the dark region with an intensity peak on the central axis. It also leads to modulation between neighboring peaks over the main ring. Both effects significantly grow with an increasing deviation in the phase delay. For $F = 0.7\pi$, the on-axis maximum amplitude becomes equal to the on-ring maximum amplitude. At the same time, the intensity ratio between neighboring on-ring peaks reaches 2.5. For a given F the effect grows with the number of channels, as is illustrated in Fig. 6.4c.

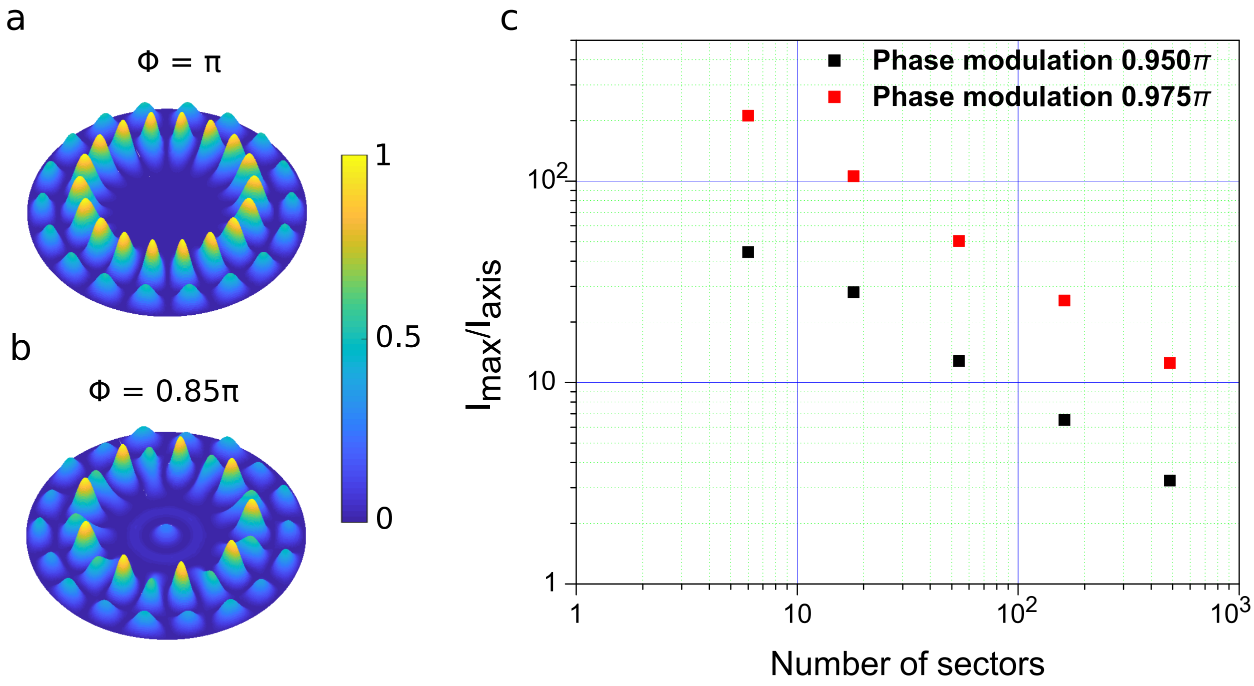

Figure 6.4: Intensity distribution after the PPA converters with various phase delays F: a: $F = \pi$; b: $F = 0.85\pi$. Number of PP sectors $N = 18$. c Intensity dependence on the number of sectors for various phase modulations. Intensity maximum is normalized by the current on-axis intensity.

Although the appearance of an on-axis intensity peak might present an interest for some particular applications, in this work we require that this central peak be zero. Finite laser line bandwidth is another factor which may affect the PPA converter performance, in addition to fabrication tolerances. This is particularly important in the case of ultrashort pulses. We simulate this effect for laser pulses with various Gaussian line bandwidths. For example, a 33nm FWHM laser line corresponding to about a 30 fs pulse duration is plotted in Fig. 6.5b. The ring radius and normalized intensity dependence for these bandwidths are found to be insensitive to the bandwidth and coincide with corresponding values for a monochromatic beam as shown in Fig. 6.3b. For cases with $N >> 1$ and bandwidths below 33nm, the intensity of the on-axis spot remains negligible.

Strictly speaking, when the laser pulse spatial length becomes comparable to the produced diffraction structure dimensions, the dynamics of its formation have to be taken into account. To consider the transient effect of laser pulse duration we estimate the time required for the steady intensity distribution to be established. When the number of PP sectors is high, e.g. $N > 50$, the radius of the main ring becomes relatively large R $\sim 20-30\mu m$, which implies that the arrival time of the pulse from the axicon to a point P (Fig. 6.1) may become comparable with pulse duration or even exceed it. The maximum time spread is $\delta t \sim 2R_{ring}tg\beta/c \sim$ 30 fs for $R_{ring} = 25\mu m$. To better understand this effect, we calculate the set of intensity distributions near the optical axis at different moments in time. We apply a Heaviside function to simulate the evolution of the generated field structure (see Fig. 6.5a). Using this data we calculate the step response and point spread functions as depicted in Fig. 6.5b. The second function is the derivative of the step response. These functions can be used to determine the real intensity dependence on time. As can be seen in Fig. 6.5b, the steady state distributions are established in about 25 fs. Therefore, for laser pulses shorter than 25 fs, the efficient intensity after the converter can differ significantly from that of the original beam.

6.3 Experiment with PP converter

We first checked the validity of our simulations experimentally with a liquid crystal SLM (LCOS SLM Hamamatsu X10468-02, 600x792 pixels). Although it cannot be exposed to high power beams due to the low damage threshold, it can easily mimic the behavior of the proposed PP converter and can be easily and quickly reprogrammed, which gives an opportunity to optimize experimental parameters. Experimental setup in the SLM configuration is depicted in Fig. 6.6a. The collimated beam from a He-Ne laser is expanded to cover the surface area of the SLM screen to minimize distortion. Since the SLM accepts only one state of linear polarization, we use a half

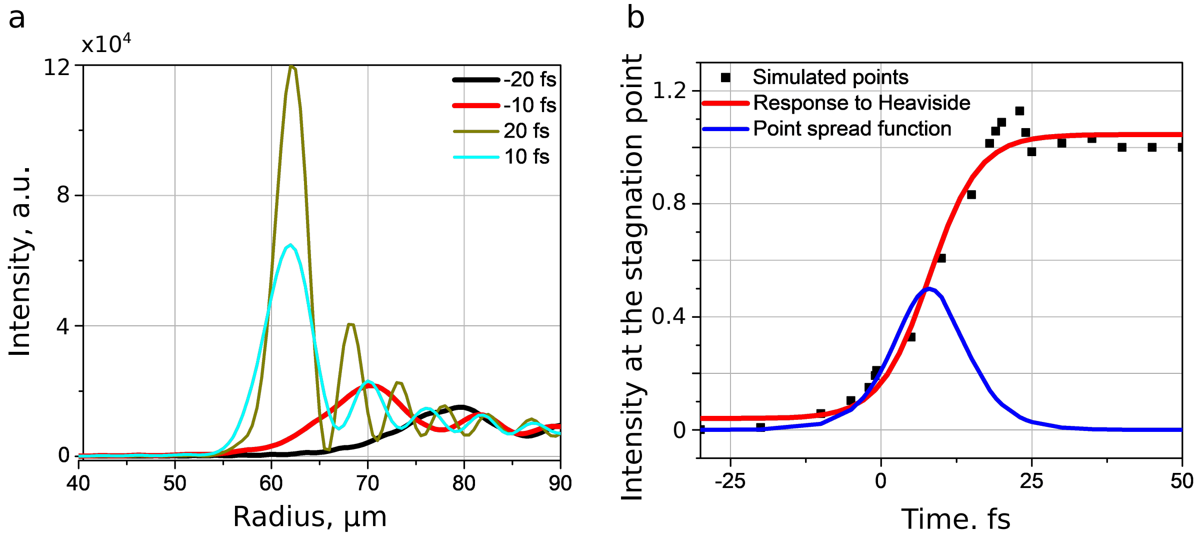

Figure 6.5: a: Temporal dynamics of a hollow beam structure. Laser pulse shape is a Heaviside step function. The number of sectors N is 162, $\lambda = 800$ nm, and the main ring radius is ~60 μm. b: Response and point spread functions. FWHM of the point spread function τ is ~ 15 fs.

wave plate (HWP) and polarizer to filter out any redundant polarization. The expanded beam then reflects from the SLM surface at a near zero incidence angle and the SLM imprints a circular phase relief onto the beam. To further avoid distortions due to the limited size of the SLM pixels (20 x 20 μm), the central part of the beam (3-mm diameter) is blocked (not shown). After that the beam with the imprinted phase is converted to a non-diffracting beam with the axicon (diameter 25 mm, apex angle $140°$), attenuated (not shown), and monitored by a CCD camera (Thorlabs DCU223). Figures 6.6b,d show the near-axis intensity distribution after the laser beam passes through this SLM-axicon setup. Ring radius measurements (Fig. 6.3a), efficiency of energy concentration, and intensity distributions (Fig. 6.4) are in excellent agreement with simulation results, shown in Fig. 6.6c. The observed tubular structure of the beam is maintained over a distance of ~3 cm along the optical axis, which is determined by the input beam diameter and the axicon apex angle.

A set of phase plates suitable for experiments with a He-Ne and high power laser beam of 800 nm wavelength and with a number of sectors N = 60 and 90 were fabricated on 2 inches diameter fused silica wafers via a standard "lift off" photolithography procedure and characterized with a scanning electron microscope. Test results of the 60 sector plate with an etching depth of 695 nm

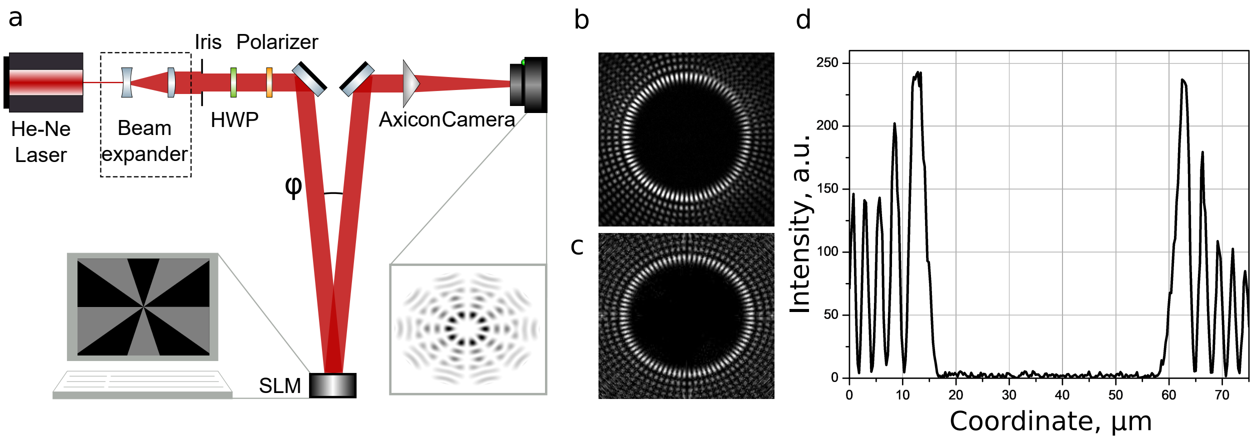

Figure 6.6: a: Experimental layout with the SLM. Beam is expanded by a Galilean telescope. HWP is a half wave plate and the incidence angle $\phi/2$ is sufficiently small $\sim 1°$ to avoid beam profile distortion. Left inset: an example of a typical phase relief for a circular lattice with N = 10. Right inset: an example of an intensity distribution observed with the CCD camera. b: Experimental intensity distribution obtained with a laser wavelength of 0.63 μm and number of sectors $N = 80$; the main ring radius is 50 μm. c: Simulated intensity distribution with the same parameters. d: Experimental transverse intensity distribution (taken from b).

(which produces a π-shift for a laser wavelength of 633 nm) are presented in Fig. 6.7a, where the intensity distributions and radial cross-section are taken at the planes located at different distances from the axicon. As one can see from the figure, the distributions are quite close to simulations and their quality remains almost unchanged over a length of 25 mm. The diameter of the main ring is $38\mu m$, thus the aspect ratio of the produced light structure is ∼600. Note the comparatively low level ($\sim 5\%$) of stray light inside the dark region of the distribution. A 60 sector plate was also tested with a femtosecond laser at 800 nm, with a pulse duration of 120 fs, shown in Fig. 6.7b.

6.4 Discussion

Experiments with the SLM and lithographically fabricated phase plates presented above show excellent agreement with simulations and demonstrate annular beams with diameters up to $150\mu m$ with length-to-diameter ratios of up to 103. The nature of such beams can be understood by analysis of the results presented above, showing that for a large number of sectors the intensity distribution after the converter can be fit with high accuracy by an angularly modulated high order Bessel function (Eq.6.4). This result can be interpreted as follows (see also [175, 176]). Consider

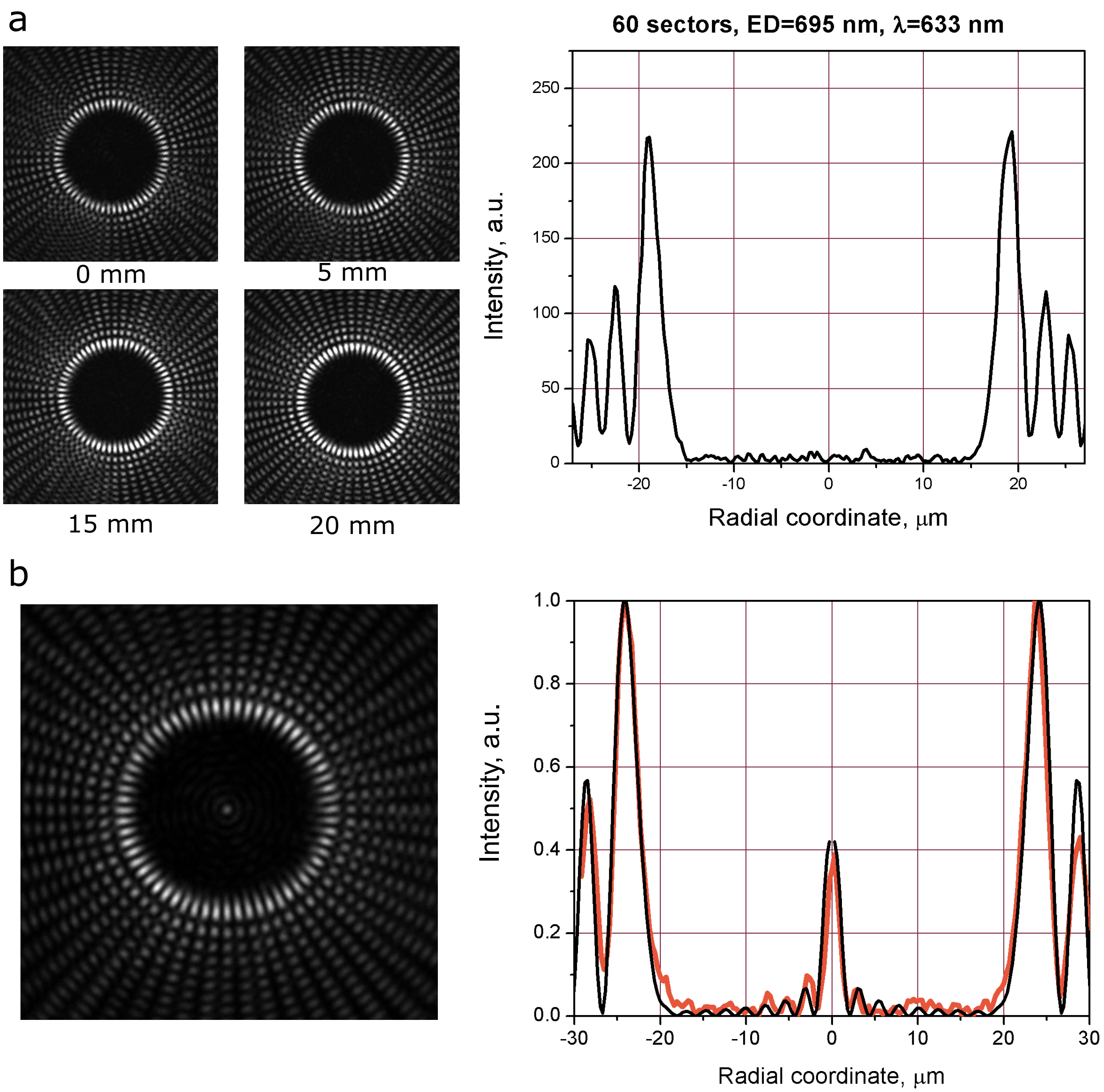

Figure 6.7: a: Intensity distributions (left) and radial intensity cross-section (right) at different distances from the axicon. The fused silica phase plate had a diameter of 2 in and an etching depth of 695nm. Laser wavelength was 633nm, and the ring diameter was 38 μm. b: Intensity distributions (left) and radial intensity cross-section (right) obtained with a 60 sector phase plate tested with a 120 fs laser at $\lambda = 800nm$. The brown curve is the experiment and the black curve is the simulation. The appearance of a low intensity peak on axis is due to a mismatch of the actual etching depth of 980 nm and the target value of 890 nm for $\lambda = 800nm$.

a laser beam with orbital angular momentum l. In the case of cylindrical symmetry, the electric field can be written as:

$$E(r,\phi,z) = E_0(r,z)e^{i(kz+l\phi)}, \tag{6.9}$$

where $E_0(r,z)$ is the complex amplitude, $r^2 = x^2+y^2$, and ϕ is the azimuthal angle. Superposition of two beams of equal amplitude carrying opposite topological charges $\pm l$ with initial phase shift α reads as:

$$\begin{aligned} E(r,\phi,z) = E_0(r,z)[e^{i(kz+l\phi)} \, + \, e^{i(kz-l\phi+\alpha)}] = \\ = E_0(r,z)e^{i(kz-\alpha/2)}[e^{i(\alpha/2+l\phi)} + e^{i(-\alpha/2-l\phi)}]. \end{aligned} \tag{6.10}$$

The corresponding intensity distribution

$$\begin{aligned} I(r,\phi,z) = |E_0(r,z)e^{i(kz-\alpha/2)}[e^{i(\alpha/2+l\phi)} + e^{i(-\alpha/2-l\phi)}]|^2 = \\ = |E_0(r,z)|^2 \, 4cos^2(\alpha/2 + l\phi) \end{aligned} \tag{6.11}$$

is modulated over the azimuth with the function $cos2(l\phi)$. The azimuthal location of different maxima is determined by the initial phase difference α between the original beams. Comparing the last expression with Eq.6.4, one may conclude that a beam produced with the combination of the axicon and a π-modulated N sector plate represents a superposition of two high order Bessel beams carrying the opposite OAM of N/2. Some deviation from the pure superposition observed for the 13th and 14th peaks in Fig. 6.2b may be interpreted as the contribution of the second order diffraction components of the PP. Azimuthal symmetry of the PP leads to balance of diffracting components which contribute to the formation of vortices carrying opposite charge. This can be qualitatively understood by accounting for diffraction in the azimuthal direction over the pure phase grating (0-π sectors, no zero order) that results in the production of two beams twisted in opposite directions. An asymmetry in the diffracting structure with respect to the azimuthal angle can lead to an imbalance of intensities in the produced vortices. For instance, consider two similar

$\pi/2$-modulated phase plates with N sectors installed sequentially and shifted by the angle π/N with respect to another. This "superimposed sector plate" will introduce into the incoming beam a phase delay of 0, $\pi/2$, π, $3\pi/2$, 0, $\pi/2$, π, $3\pi/2$ etc., providing a $2\pi/N$ periodic structure with asymmetry in the azimuthal direction. After combining this PP with the axicon, the outgoing beam can be represented by two vortices with opposite OAM and unbalanced intensities. Obviously, this "superimposed plate" serves as a rough approximation of the spiral plate. The limit of a very large number of sectors and small amplitude of modulation represents a perfect phase screw. Note that the 100% intensity modulation in the semi-ring structure stems from equal intensities of the produced vortices of opposite charge. As a result, the maximum intensity exceeds the case when a single vortex is generated with a "classical" spiral phase plate by a factor of 2.

In conclusion, we propose a PPA converter as a novel method for generating circular lattices with simple phase modulation. The advantage of this converter is in its relatively simple binary phase pattern in combination with an axicon. The converter allows us to avoid complex combinations of Bessel and Laguerre-Gaussian beam modes for creating the circular lattices of interest. The same phase pattern can be used to manufacture a simple binary phase plate for creating an extended lattice with extended plasma channels, which are of particular interest for a number of applications like guiding powerful laser beams in plasma, X-ray lasing, Raman back scattering, electron acceleration, and generation of shock waves in gases. We simulate the various aspects of the PPA converter performance and find optimal PP parameters and fabrication tolerances to manufacture the PP for future experiments with high energy beams. We consider the effects of ultrashort pulse bandwidth and duration on the performance of the PPA converter. We confirm the performance of the proposed converter and validate all the calculated optimal parameters in the experiment with an SLM and manufactured fused silica phase plates with a He-Ne and Ti:sapphire CPA 800 nm laser. Experiments with lithographically fabricated phase plates demonstrate the high potential of the proposed approach for high energy laser beam applications.

7. ADAPTIVE SURFACE ENHANCED RAMAN SCATTERING ON RANDOM NANOSURFACES VIA WAVEFRONT SHAPING

Surface-enhanced Raman scattering (SERS) spectroscopy is a popular technique for detecting chemicals in small quantities. Rough metallic surfaces with nanofeatures are ones of the most widespread and commercially successful substrates for efficient SERS measurements. A rough metallic surface creates a high-density random distribution of so-called ‘hot spots’ with local optical field enhancement causing Raman signal to increase. In this letter we revisit the classic SERS experiment [177] with rough metallic surfaces covered by a thin layer of copper phthalocyanine molecules. As a modification to the classic configuration, we apply an adaptive wavefront correction of a laser beam profile. As a result we demonstrate an increase in brightness of local SERS hot spots and redistribution of Raman signal over the substrate area. We hypothesize that the improvement is due to optimal coupling of the shaped laser beam to the random plasmonic nanoantenna configurations. We show that the proposed adaptive-SERS modification is independent of the exact structure of the surface roughness and topography, works with many rough surfaces, and gives brighter Raman hot spots in comparison with conventional SERS measurements. We prove that the adaptive-SERS is a powerful instrument for improving SERS sensitivity.

7.1 Introduction

Surface-enhanced Raman scattering (SERS) technique is well known for its ability to detect small concentrations of analytes. SERS was discovered in 1974 by Fleischmann *et al.*, working with pyridine molecules adsorbed at a silver electrode [18], and then demonstrated in a modified version by Hayashi [177], by utilizing rough surfaces coated with copper phthalocyanine (CuPc). SERS is of high demand by biochemists, because of its *in vivo* sensing ability [178]. SERS exploits Raman scattering, known for exceptionally high molecular specificity, in combination with enhancement given by locally generated surface plasmons - collective oscillations of electrons - induced by the incident laser field [179]. The enhancement is critical, because without it spontaneous

Raman scattering is extremely inefficient and requires a large number of molecules to produce a measurable scattering signal. Typically, two SERS mechanisms are identified as contributing to the Raman signal enhancement: chemical (charge transfer) mechanism, providing a $\sim 10^2$ [180], and electromagnetic mechanism responsible for $\sim 10^4 - 10^{12}$ enhancement [181]. The total SERS enhancement factor has been observed to be as large as 10^{14} [19], however, quantitative theories on the sensitivity limit of SERS are still under debate [182] and the question whether the SERS is capable of sensing a single molecule is still open.

The concept of a plasmonic hot spot is central to the theory of electromagnetic enhancement in SERS. Hot spots are formed due to an interplay among (1) resonant plasmon excitation, (2) a lightning-rod or edge effect, and (3) focusing of surface plasmon-polaritons (propagating plasmons). A single hot spot often occupies a region only several nanometers across, and can occur in, for example, a local dip on a metallic surface. In that region the electric field can exceed the incident laser fields by orders of magnitude - a number termed the field enhancement factor. When a molecule is localized in the hot spot, Raman scattering off of that molecule is enhanced by the total factor equal to the field enhancement factor raised to the 4^{th} power. This is because light/radiation intensity is proportional to the field squared, and the hot spot enhances both incident and scattered radiation. While the enhancement of the incident radiation is easy to understand (it's akin to ordinary focusing), the enhancement of the scattered radiation can be viewed as being due to the increase of the density of states of light. Vaguely speaking, hot spot physics leads to focusing of both the incident light and the vacuum fluctuations that lead to spontaneous Raman scattering [183]. Concentration of light in a plasmonic hot spot is therefore qualitatively different from what can be achieved with a simple lens.

Surface plasmon resonance provides the major contribution to the electric field enhancement mechanism; the enhancement is largest when the incident laser wavelength is on resonance with the natural plasmonic oscillation. Many studies show that variations in size and shape of surface nanofeatures cause significant change in the surface plasmon resonance [22], making it possible, with the recent advancements in nanomanufacturing, to tune the resonant frequency. Mie theory explains this tuning only for simple symmetrical particles [184], and quantitative methods for more complex shaped objects involve numerical calculations such as finite difference time domain (FDTD) or finite element methods (FEM). Furthermore, the lightning-rod or edge effect comes into play for sharper features, and the surface plasmon-polariton propagation and focusing contributes to the full picture and makes the highest hot-spot field enhancement possible.

SERS with colloids and rough metallic structures relies on a random distribution of hot spots within the illuminated area [185, 186]. However, with the advent of lithographic techniques it becomes possible to create an ordered distribution of hot spots and improve robustness and sensitivity of SERS [187]. In addition, with the advancing atomic force microscopy (AFM), one can create local hot spots anywhere on the sample surface using metalized AFM nanotips, which are usually as small as $\sim$ 10 nm in apex diameter. This technique is called tip-enhanced Raman spectroscopy (TERS) [188], and it gives an opportunity to image biomolecules, *i.e.* DNA [189], with unprecedented sub-nanometer spatial resolution combined with high chemical specificity. Lithographically manufactured SERS substrates and metallized TERS tips offer a pathway toward engineered plasmonic nanoantennas that, at least in principle, can be optimized to receive an ideal plain wave or a Gaussian light beam and concentrate a substantial part of its power into the hot spot. In practice, this task is challenging because of unavoidable imperfections in manufacturing and surface-quality problems. Besides, while both techniques have produced remarkable results, combining high sensitivity, specificity, and resolution, they suffer from low reproducibility, and quantitative theories describing them are limited. In comparison, the original type of SERS, utilizing random rough and/or colloidal structures, appears to leave little room for design and optimization. In this work, we propose and implement a scheme where optimized coupling of laser power into a plasmonic hot spot is accomplished via adaptive optical wavefront shaping.

Laser wavefront shaping by adaptive correction of the beam phase profile is a powerful instrument for improving the qualities of various spectroscopic techniques. With an adaptive wavefront correction it is possible, for instance, to enhance spontaneous Raman signal through turbid media [13] or to increase coherent Raman scattering in a Raman-active crystal [190]. Moreover, adap-

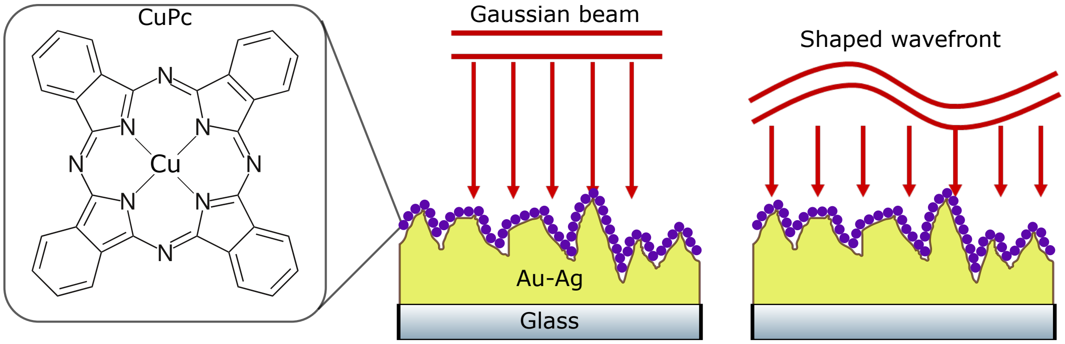

Figure 7.1: Schematic layout of the substrate. Inset: Molecular structure of copper phthalocyanine (CuPc). Red arrows show schematically the sample illumination by shaped vs. Gaussian laser wavefront.

tive optics is able to control stimulated Raman scattering (SRS) and four wave mixing (FWM) processes in a multimode fiber [15]. In the last few decades, with the availability of fast high-resolution digital micromirror devices (DMDs) [191], adaptive optics is becoming faster and more compact than ever, which gives a freedom to implement it to any experimental setup [1, 4].

In this letter we show that if applied to SERS, wavefront shaping via adaptive optics has a capability to increase the Raman signal from analytes. The adaptive wavefront correction redistributes localized plasmons and makes plasmons to be generated in more efficient way. Adaptive-SERS could potentially improve the sensitivity of SERS and allow measuring low concentrations of analytes or, in the ideal case, reduce the sensitivity limit to a single molecule [23]. Moreover, we show that the adaptive-SERS is robust, and it can be applied to a rough metallic surface with any nano-relief.

7.2 Experiment

For the proof of principle experiment we use commercially available Ocean Optics SERS substrates RAM-SERS-SP, that are manufactured with a gold-silver (Au-Ag) nanosponge alloy to produce stable random hot-spot surface distribution, (for other methods of preparing metallic surface with nano-relief see Appendix D). We cover these substrates with a thin layer of copper phthalocyanine (CuPc) molecules, Fig. 7.1, and monitor the behavior of three relatively strong Raman lines (around 1520 cm^{-1}, 1445 cm^{-1}, 1335 cm^{-1}) at various spots on the surface. To induce Ra-

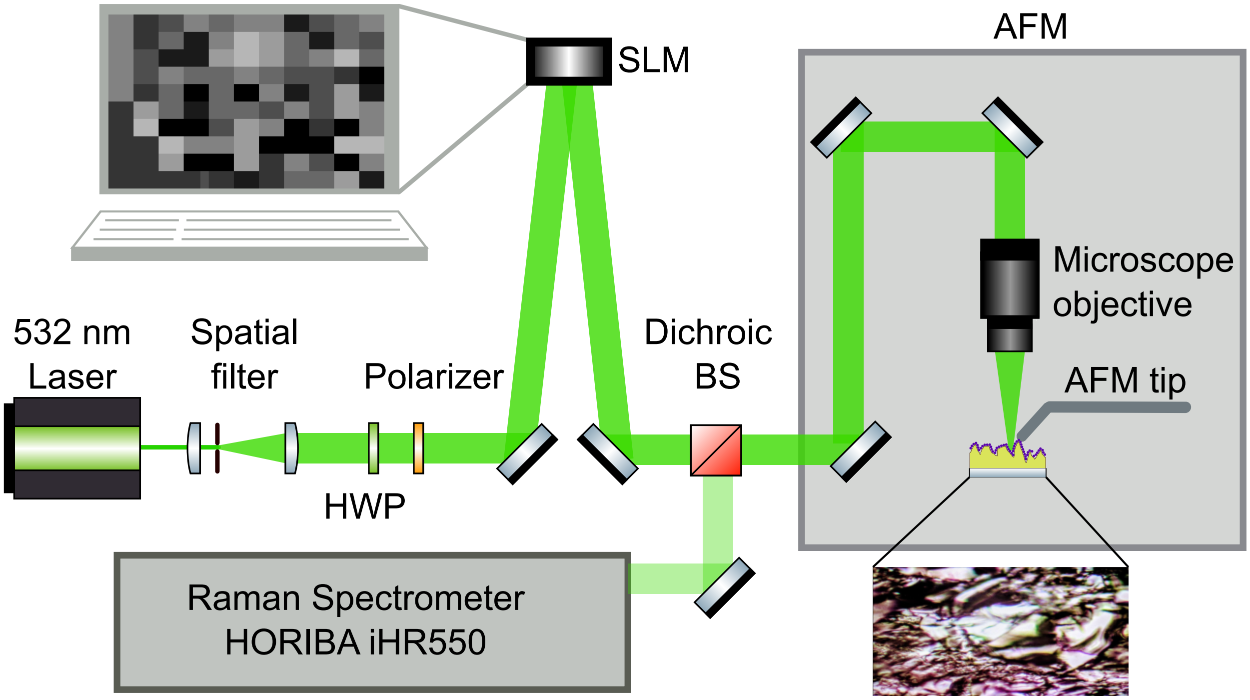

Figure 7.2: Experimental setup for SERS with wavefront correction. HWP is half wave plate. SLM connected to the computer with the dynamic wavefront correction software. Microscope objective (Olympus, NA 0.45) focuses shaped beam onto the sample with the rough metallic surface and thin layer of CuPc molecules. Inset on top: an example of generated phase mask, displayed on SLM scree. Inset on bottom: optical microscope image of the rough metallic Au-Ag surface.

man scattering, we use 532 nm pump laser (Verdi, Coherent Inc.), Fig. 7.2, which is the closest to the plasmon resonance of the Au-Ag alloy. We use the reflective phase only liquid crystal on silicon spatial light modulator (LCOS SLM) to do the input beam wavefront correction. We use a list of phase masks generated by a sequential algorithm described in Ref.[9, 190], display them one by one on the SLM screen and determine the phase profile for the output beam that increases Raman scattering signal detected by the spectrometer (Horiba iHR550).

Before applying the wavefront correction, we perform characterization of the rough random surface with the Raman and AFM microscopes. Figure 7.3a shows the AFM image of the substrate. As we see, AFM topography image does not give sufficient information about the surface relief, therefore we add AFM phase image, 7.3b, to reveal small defects on the surface [192], obtained by detecting phase feedback of AFM tip. These defects give rise to hot spots under Raman

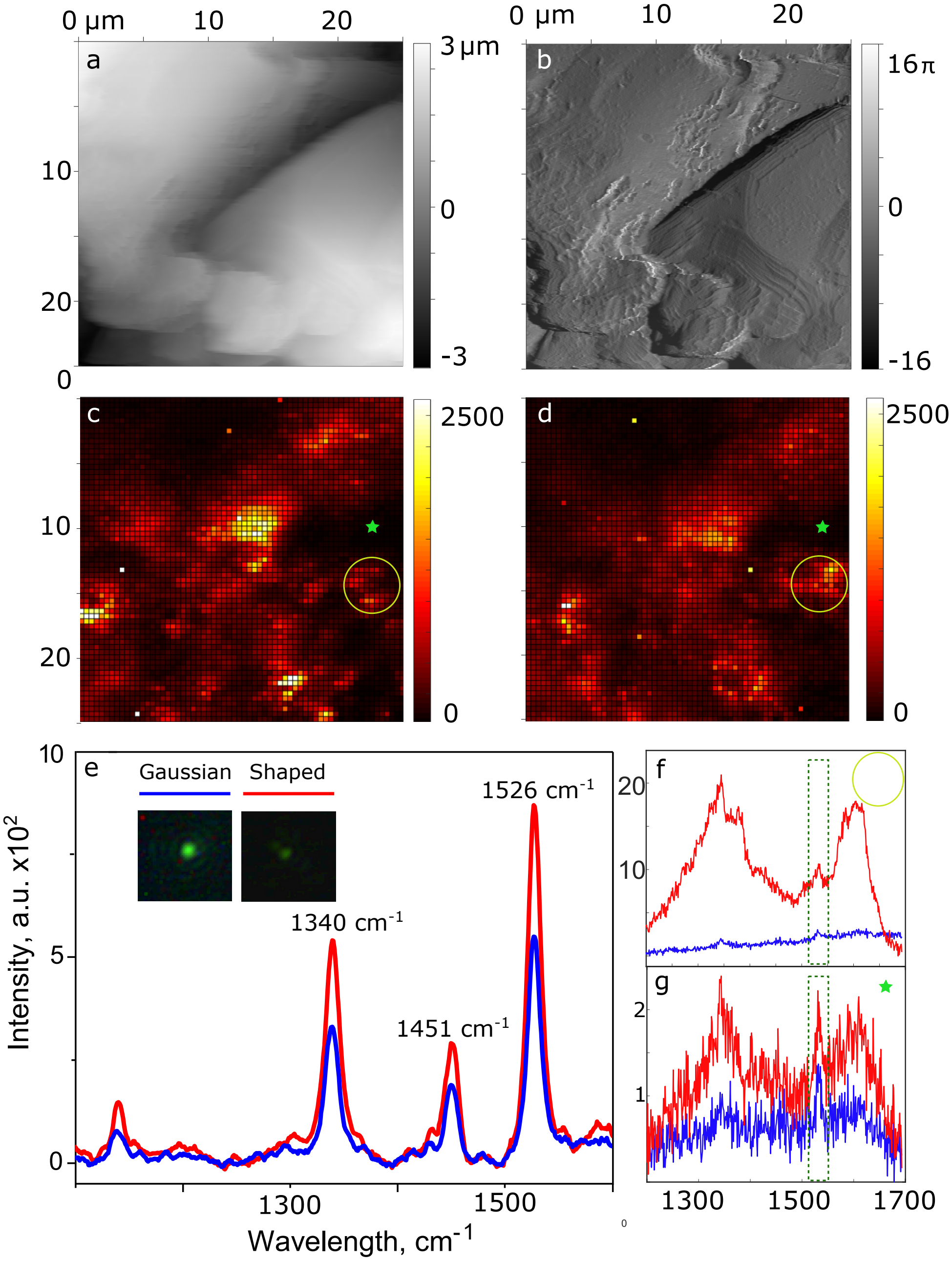

Figure 7.3: AFM images of 25x25 μm of the SERS substrate. a: topography map; b: corresponding phase map; c: corresponding Raman map with the spatial hot spots distribution. Colorbar shows the intensity (a.u.); d: Raman map of the same area on the substrate, taken with shaped laser beam; e: Optimization procedure: Raman signal comparison in the local hot spot taken with Gaussian beam profile (blue line) vs corrected wavefront (red line). This measurement is taken inside the white circle with a 10 s acquisition time and baseline correction, separately from c and d. The spectra show the Raman peaks of interest, and a typical signal enhancement during the optimization procedure. f and g show the spectra comparison from the actual data scans c and d with 1s acquisition time. Sign in the upper right corner of each indicates where this spectra were taken. Green dashed rectangle shows the spectral range, where the signal was optimized (around $1520 cm^{-1}$). We pick two points (star and circle) to compare the spectra in bright area and in the dark area of the scan.

microscope. We then correlate AFM microscope image of the surface with the Raman microscope image (without AFM tip) 7.3c to see how the topography of the sample reflects the positioning of hot spots. We see that the observed hot spots have various sizes and signal enhancement factors.

7.3 Results

After mapping the hot spot distribution, Fig. 7.3c, and their enhancement factors, we apply the wavefront shaping algorithm. For this we pick a random hot spot, which is visible on the Raman image (white circle), move our laser beam to its location using fine knobs of the AFM piezo drivers, and execute the wavefront correction algorithm described above. When the algorithm is finished and we see the increased resultant Raman signal, we readjust the focal distance of the objective, to make sure that we work with the brightest and smallest possible laser spot. The beam diameter (full width at half maximum, FWHM) of the initial non-shaped beam in our experiment is 1.4 μm. As we see on Fig. 7.3e, SERS signal in the particular spot increases. After we detect the increase in the signal, we scan the same area with the shaped beam to see how the hot spots redistributed, Fig. 7.3d. As an example, the hot spot in the white circle (target hot spot) that was a reference point has an improved local enhancement factor. We note that we can do only two scans on the same area of the substrate without significant sample degradation and bleaching, even with relatively short acquisition times (1-2 s). The only way to reuse the surface at least one more time is to increase the laser power, but this, on the other hand, can damage the metallic surface. Unfortunately, it is not possible to keep the laser power at the same level and increase the acquisition time, as we have to deal with the mechanical sample drifts when obtaining long-time acquisition and high resolution Raman image of a relatively large area. Therefore, we cannot reuse the same area and do two consecutive measurements with two different phase profiles.

To check whether the enhancement from wavefront shaping is universal and repeatable, we need to overcome the experimental problems described above. For this, we randomly pick several ($\sim$15) areas (20x20 μm) on the sample and run the wavefront correction procedure, described above, Fig. 7.4 shows some of the representative data. As a result, we get the signal enhancement for the target hot spots (white circles) in the most cases; that ranges in average from 1.1 to 2. We

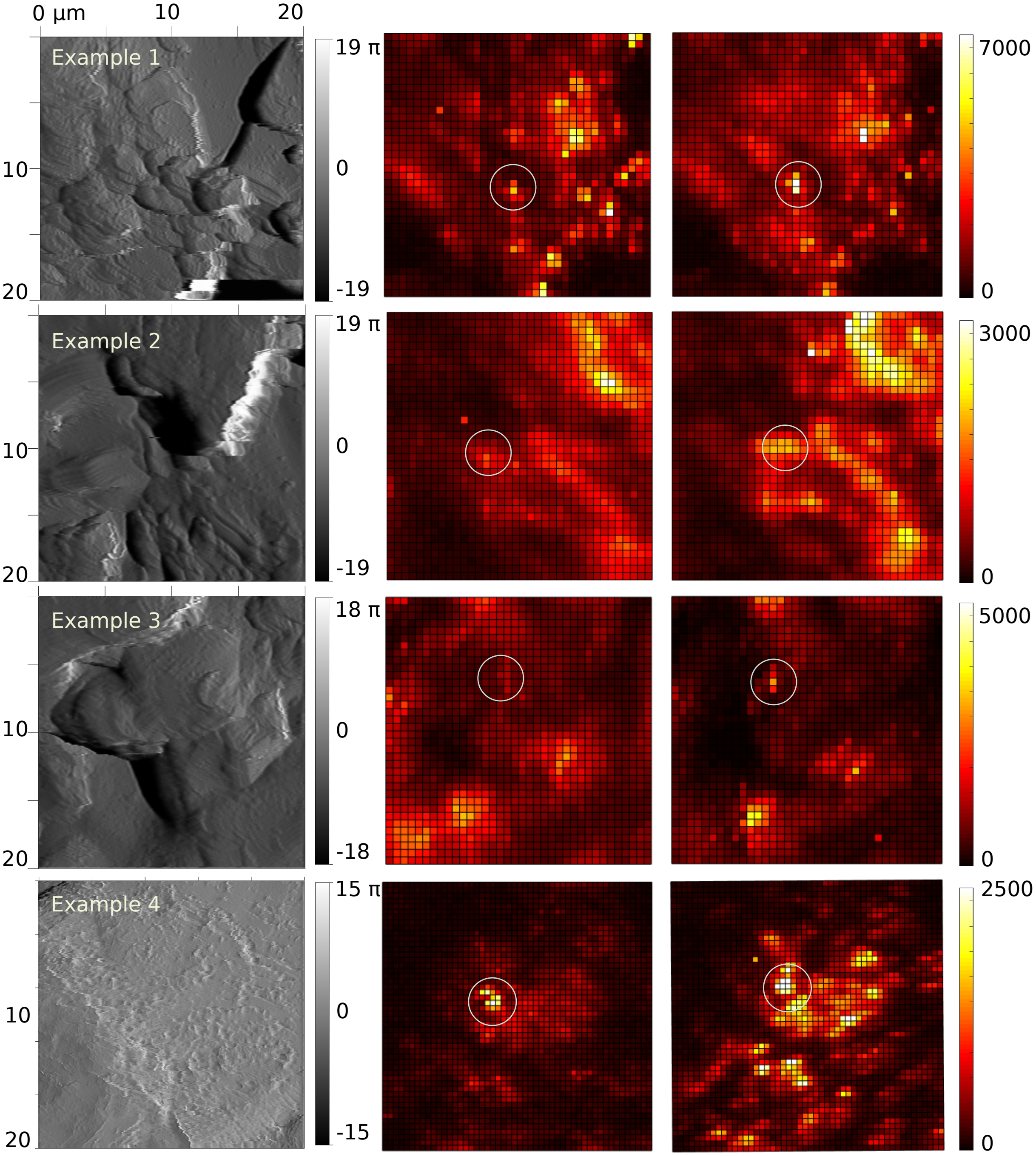

Figure 7.4: Examples of surfaces on a SERS substrate. Left column: phase AFM image. Middle column: Raman image with non shaped beam. Right column:Raman image with shaped beam. Hot spots that were being optimized are highlighted white circle.

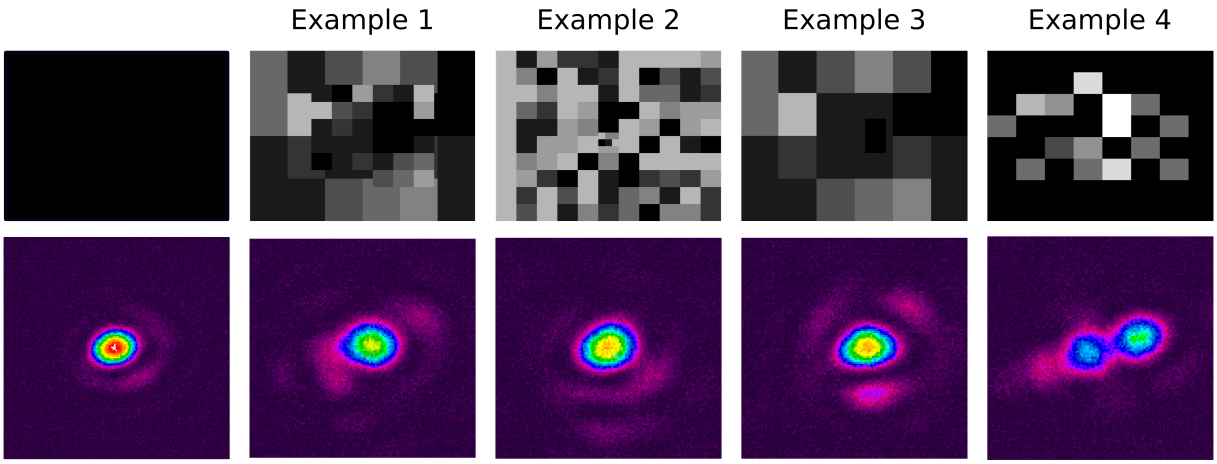

Figure 7.5: Phase masks (top) and corresponding beam profiles (bottom) for unshaped beam and Examples 1-4. The images are taken with the beam profiling camera (Spiricon SP620U), the laser beam is focused right after the SLM with a plano convex lens (focal distance 30 cm). The beam size is reduced to 5 mm in diameter, to emulate the microscope objective input.

also see that the other intensity distribution over the rest of the sample area may vary significantly. In Example 1, the target hot spot has become brighter, in contrast to the most of surrounding hot spots. Examples 2 and 4 show the overall Raman signal increase over the whole scanned area and many more hot spots brighten in addition to the target one. Example 3 depicts significant brightening of the target hot spot and shrinking and brightening of two surrounding hot spots. We conclude that different pump wavefront shapes optimize coupling for different hot spots spread over the area of a random sample. We use a beam profiler (Spiricon, SP620U) to measure the pump laser beam shape before and after running the adaptive algorithm. Figure 7.5 shows the measured profiles. We see that the initial, not shaped beam has an almost ideal Gaussian profile, and it is the brightest in comparison with the shaped beams. We note that if we run the algorithm twice for the same hot spot, we often get two different correcting phase masks, therefore, the "optimal" phase masks are not unique.

7.4 Conclusion and discussion

To summarize, our experiment demonstrates the use of adaptive wavefront correction to increase Raman signal in SERS. We show that this approach, which we call adaptive SERS, improves the enhancement factor and in general, alters the intensity and distribution of SERS hot spots. The phase-only adaptive optics algorithm relies on tailoring the phase profile and changing the laser beam wavefront in accordance with the surface topography. By doing this we achieve more efficient surface plasmon generation and field enhancement in the chosen hot spot. We believe the main mechanism that drives the signal improvement lies in the more efficient hot-spot excitation and, therefore, Raman scattering off of the molecules located in the hot spots. We don't expect the optimization process to affect the directionality (radiation pattern) for the chosen spot on the sample.

Many questions remain, and will be addressed in future studies. For example: Will adaptive pump-beam shaping improve TERS? And: What if in SERS, in addition to shaping the pump beam, we also shape the signal beam (on its way to the spectrometer)? Will we be able to optimize the coupling of the distorted signal beam into the spectrometer? [We believe our spectrometer slit was likely accepting a constant fraction of the signal light, but the question still deserves a more careful consideration.] The demonstrated method is universal and can be applied to different kinds of surfaces, since the wavefront shaping relies only on the output Raman signal and does not depend on the particular features and structures on the sample surface. As we have shown in this letter, in addition to SERS enhancement factor increase for the target hot spot, the wavefront correction can result in many different outcomes. It increases an overall Raman signal; brightens a target hot spot, and makes the surrounding hot spots less/more bright; or brightens the target hot spot with the same relative signals from surrounding hot spots. As a continuation for this experiment we propose to develop a feedback loop algorithm, which will tie up all the possible controls of AFM, Raman microscope, spectrometer and SLM and optimize them in order to achieve any desired outcome.

8. SINGLE MOLECULE CHIRAL SPECTROSCOPY WITH SHAPED BEAMS

8.1 Introduction

In this chapter we develop the experimental tool for single molecule chiral spectroscopy. We build upon three technological pillars, depicted in Fig. 8.1: (1) the ability to produce structured beams with the programmable, precisely controlled shape; (2) nanofabrication capabilities allowing production of plasmonic nanoantennas; and (3) detection techniques making single-molecule spectroscopy possible [193]. Our work ties together the key elements of three pillars - three red hexagons of Fig. 8.1 - allowing for an ultimately new type of fundamental spectroscopic studies. Bioplasmonics is already enabling detailed analysis of living biostructures with high resolution [194]. Plasmonic nanostructures can concentrate light within subwavelength region and greatly enhance the local electric field [195]. Existing ultrasensitive plasmonic nanosensors are based on nanostructures [196], metasurfaces [197], or random metallic nano-surfaces [198]. With all of these means it is possible to induce electric dipole transitions in molecules that are subjected to the local enhanced electric field [199], when the structure is illuminated by light resonant with the localized surface plasmon. Recent technological advancement, such as 3D focused ion beam microscopy [200], have allowed us to construct plasmonic sensors of various geometries at high ($\sim$ 1 nm) resolution. However, since plasmonics is a relatively new field, there is considerable room for improvements. Even with state-of-the-art sensors, many questions stay unanswered and many problems remain unsolved.

A prominent example of such a problem pertains to an interplay between chirality of matter and chirality of light [201, 70]. Unlike left- or right circularly polarized light interaction with chiral molecules (optical activity), the effect of light's OAM (or its left- or right-handeness, Fig. 8.2) on chiral molecules has not been adequately explored. The reason why the exploration of chiral-light-matter interaction is so difficult experimentally is simple: it is the orders-of-magnitude mismatch between the characteristic size of molecules (nm) and the smallest achievable characteristic size

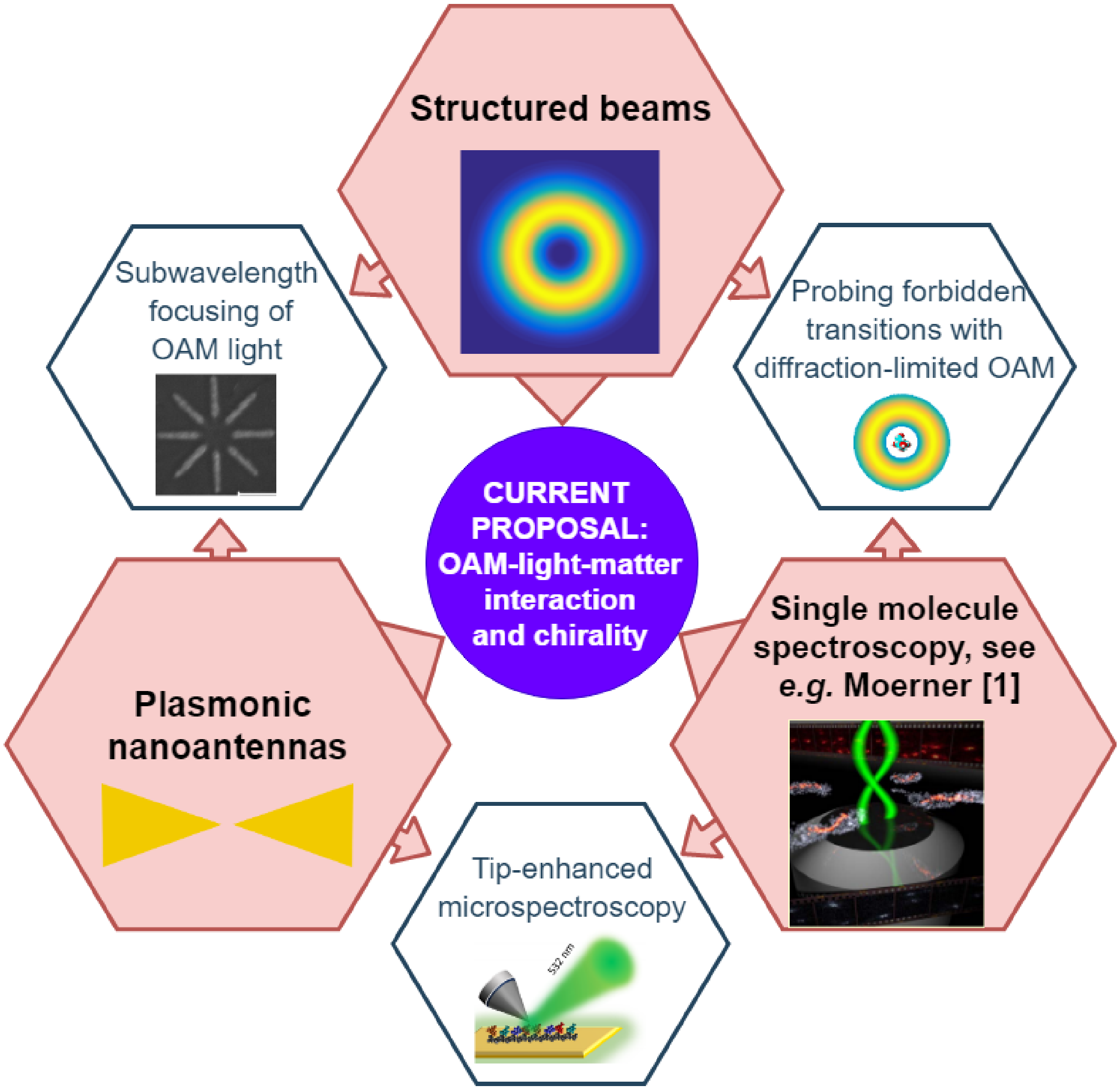

Figure 8.1: The genesis of the current chapter. Red hexagones depict existing well-developed technologies. Small white hexagones are the combinations of two neighbouring red hexagones. Our experiment in the middle is a combination of all depicted concepts.

of free-space laser beam structures (microns). Another under-explored problem is non-efficient inducing of multipole transitions in single molecules [68, 202, 203, 204].

When studying interaction of molecules with OAM-carrying beams, the experimental challenge is threefold:

- The need to understand the basic principles of chiral light-matter interactions. The groups of Cameron *et al.* [70], Afanasev [68], Forbes and Andrews [74, 71], Jauregui [67] and others

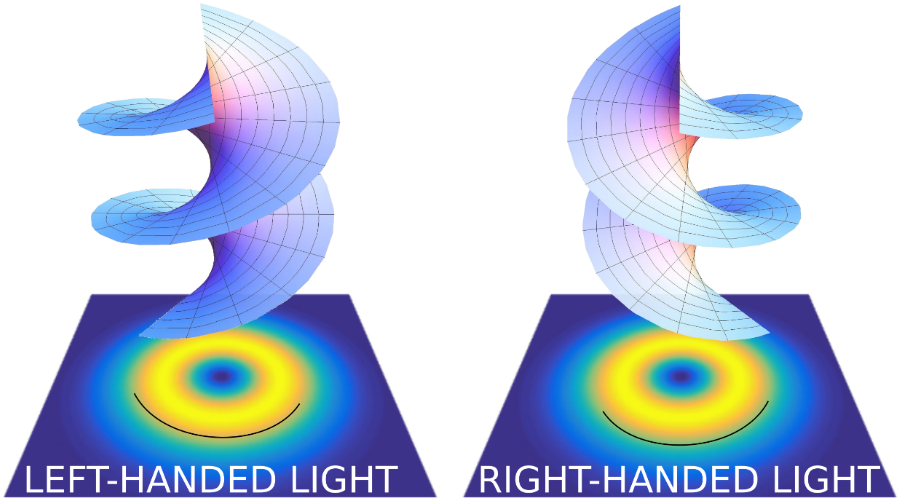

Figure 8.2: Left- and right-handed light with OAM. The light's wavefront looks like corkscrew, it can be twisted left or right. This twist does not affect final intensity distribution; however, this twist as well as phase singularity, play important role in chiral light-matter interactions.

connect chiral OAM-light interactions with combinations of forbidden atomic transitions. However, the existing theoretical hypothesis needs further development and, importantly, support with experimental evidence;

- The need of precise placement of the molecule at the center of the OAM light beam (the phase-singularity point). This problem may be approached differently, e.g. trapping the molecule in an electrostatic or magneto-optical trap, that has been done by Schmiegelow *et al.* in [69]. Alternatively, one can come up with a novel experimental configuration based on AFM tip functionalization [205], which will ensure non-optical stable molecular position in the vicinity of beam axis which considers molecular orientation.

- The need of the large optical field gradient such that the field changes considerably on the molecular length scale. A high optical field gradient is required for quadrupole transition to occur inside the test object as well as for inducing chiral light-matter interactions. In the absence of sub-diffraction-limited focusing this would require ultra-high light intensities. This condition is necessary to increase the probability of the light transition to the internal

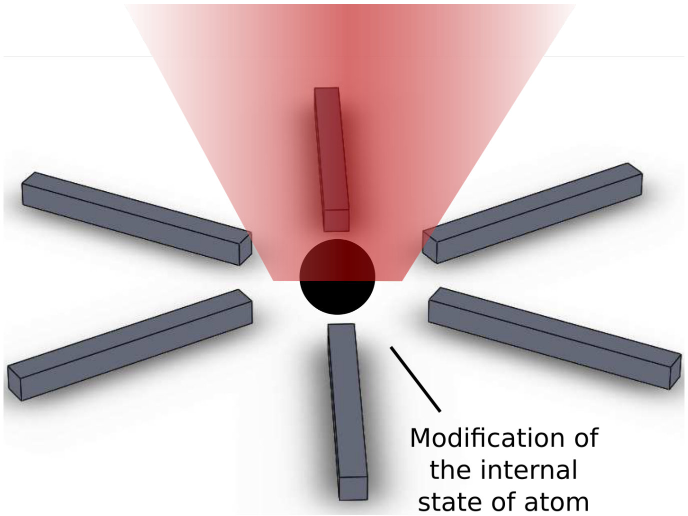

Figure 8.3: An example of nanoantenna, which serves as a nanolens and focusing the light onto the nanosized scale, preserving its structure. Under this condition, a modification of atomic state and selection rules with light is allowed.

degrees of freedom (dippole-forbidden ones). High optical field gradient can be created by transferring the spatial light structure onto the nanoscale by means of plasmonic nanoantenna - thereby increasing the field gradients without increasing the peak intensity.

In this work we expand previously mentioned scope studies to complex biomolecules (such as amino acids, proteins, DNA) and enhance the transition probability by reducing the size of the light beam. Single-molecule spectroscopy with the OAM-carrying light will provide a tool to access and study transitions that would otherwise be forbidden [206]. Nano-structured light can become a useful tool in nano-biophotonics, enabling studies of basic processes in biomolecules and providing a doorway toward fundamental science which may ultimately help cure diseases and study human genome in a more efficient way [207]. We aim to develop and fabricate nanostructures suitable for subwavelength focusing of light with OAM and integrate these structures with molecules in the center to study chirality and probe quadrupole and magnetic transitions. Ultimately, our goal is to create a new technology for the focusing of twisted light into the subwavelength volume. This technology will help answering questions such as: does the twisted, or so-called chiral light interact with chiral molecules in some special way, when we transfer OAM to the molecule's internal degrees of freedom? Can we excite quadrupole transitions in the molecules more efficiently with the OAM-carrying light? As we study these questions, we expect to be able to make the transfer of OAM from light to the single molecule much more efficient, and to detect OAM photons emitted by the molecule. The ability to transfer the light structure to the nanosized volume can also bring the resolution of the imaging techniques to the atomic scale and help to efficiently induce the forbidden transitions in biomolecules. All this will lead to better understanding of basic processes in living organisms.

Our project aims to capitalize on state-of-the-art nanomanufacturing technology in order to study chirality and OAM-of-light-matter interaction. Moreover, OAM of light, focused to break the diffraction limit, can be used in microscopy and spectroscopy with structured light that will give a new way of seeing and characterizing molecules or other small complex objects. Light with OAM has a corkscrew wavefront and has a characteristic quantum number, called topological charge (TC) [32, 50, 49]. The zero-intensity center axis of such a beam is a basic light-wave phase singularity [31]. An integer number of 2π phase accumulation around one turn of the wavefront spiral corresponds to integer TC, or, in the ideal case, an integer amount of orbital angular momentum that the vortex carries [32]. An optical vortex can be considered as "chiral" in the same sense as a molecule. To detect the impact of the structural "twist" on the chiral molecule, in other words to transfer OAM to internal degrees of freedom, the twist feature size ($\sim 10^{-6}$ m for diffraction-limited focusing) needs to be made comparable with the size of the molecule ($\sim 10^{-9}$ m). A plasmonic antenna confining the spatial structure of light inside the small volume can solve this problem [53, 208, 209] (Fig. 8.4). Here we note that in the prior work, Kern *et al.* [210] have shown that it is possible to increase the probability of a dipole-forbidden transition in cesium by several orders of magnitude with linearly polarized light using a standard dipole nanoantenna; and the group of Kasperczyk *et al.* have demonstrated detecting magnetic transitions in quantum dots using optical wavelengths with an azimuthally polarized laser beam [206].

One of the important milestones of this work is to create a reliable and repeatable algorithm for subwavelenght focusing of structured light. Focusing ability is as important here as the proper

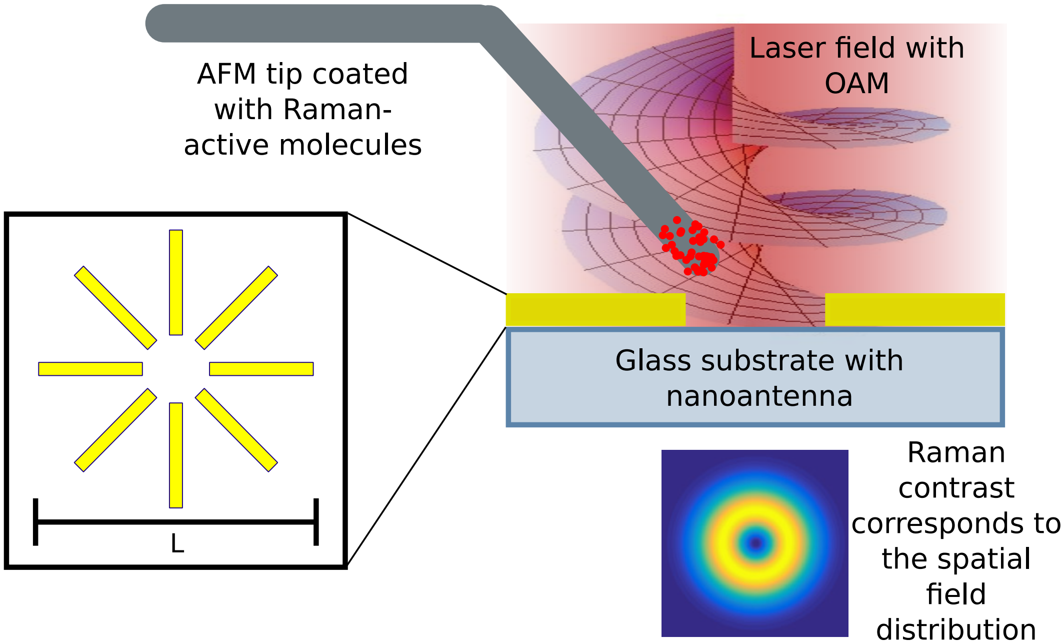

Figure 8.4: The experimental scheme. Inset depicts the geometry of the nanoantenna for OAM focusing, where L is the effective size of the nanoantenna, of the order of illuminated wavelength. The AFM tip, covered with Raman-active molecule can probe spatial distribution of optical field, with ~ 2 nm spatial resolution.

transfer of light's spatial structure to the nanoscale. In other words, the phase singularity point should be stable and the OAM of the focused light should have the same topological properties as in the initial state. Moreover, we need to establish the optical light field probing algorithm that would work with nano-resolution.

In earlier theories and experiments it was assumed that OAM component of light cannot be independently transferred to molecules [72, 73]. However, the discussion continued over the years, and researchers started to find evidence of the opposite [71, 74]. The phase singularity in the middle of the optical vortex plays significant role in OAM light-matter transfer. It means that the chiral molecule has to be tightly located on a beam axis. On the other hand, if the molecule is located on the beam axis, it only sees the zero field intensity that is associated with OV dark center. Hence, some experimental tools need to be developed to reduce the optical vortex diameter. Moreover, the theoretical concepts to support this problem should be developed.

The theoretical work [202] proves the possibility to focus light with OAM into the subwavelength volume with the nanoantenna while preserving its structure. However, the experiment [68] uses diffraction-limited vortices and relies on a very small transition probability. The work focuses on inducing forbidden transitions in trapped calcium atoms with a diffraction limited OAM beam and detection of the corresponding change in selection rules. The measured transition is extremely weak due to the light-atom size mismatch.

The theory and simulation done by Heeres *et al.* [52] bring this idea forward by proposing a simple and straightforward plasmonic nanoantenna design to focus light with OAM. An example of such a nanostructure is depicted in Fig. 8.3. Conveniently, the suggested antenna design can be used for all wavelengths of light, with proper scaling [199]. Arikawa *et al.* [53] in their work demonstrated the perfect subwavelengths focusing of terahertz light with OAM, using larger scale (millimeter-sized) antennas proposed in [52]. A similar design has a potential to work for the visible wavelengths range, which is the most suitable for studying chiral biological molecules [189] and forbidden transitions [69]. Visible light naturally provides smaller focused spot size and can be safely used for studying living organisms. However, deeper studies and design optimizations need to make such a complex structure easier to fabricate and work in real experiment. To the best of our knowledge, there is no demonstration of the visible light with OAM subwavelength focusing after the works mentioned above were published. We aim to fill this gap, taking several works [68, 53, 52] as a foundation and overcoming possible difficulties.

The main obstacle to the experiment in the visible range is the fabrication difficulties. Fabrication of small antennas is technologically demanding, particularly when it comes to the issue of surface quality of the smallest features. It is worth noting that long wavelengths are not convenient to study biomolecules, because the area of the optical field and the structure confinement are still too large in comparison with the size of a single biomolecule.

In this chapter, we define optimal characteristic sizes and geometrical layout of the nanoantenna for visible light carrying OAM through simulation and optimization. Then, we fabricate nanoantenna using focused ion beam (FIB) microscope. After that, we test the performance of the nanoantennas in experiments by mapping the electric field's spatial distribution (Fig. 8.4). In this experiment, focusing strength of the nanoantenna is as important as the proper transfer of light's spatial structure to the nanoscale. In other words, the phase singularity point should be stable and the OAM of the focused light should have the same topological properties as in the initial state. And finally, we develop and propose the experiment to test the OAM transfer from light to simple single molecules, quantum dots/nanodiamonds or/and widely used rare earth doped nanoparticles, since these are relatively easy to grow in small sizes and have many dipole-forbidden magnetic and quadrupole transitions. To effectively test the process of OAM transfer to the internal degrees of freedom, we plan to use color centers in nanodiamonds, which are widely known for their magnetic sensing applications in physics and biology [211]. After successful development of all these steps we will move on to testing more complex biomolecules, such as aminiacids, proteins and DNA, using well developed chemical procedures in a combination with our experimental setup.

8.1.1 Simulation

We choose the simplest nanostructure layout that is capable of focusing light with OAM onto the nanoscale. There are two types of experimental layouts: transmission scheme (the transmitted light is being detected by another objective), that is popular in the literature [212, 213] and reflection scheme (the light that gets reflected back into the objective). In our work we use a reflection scheme, where the molecule is placed in the center of the nanostructure and the reflected light is detected. However, the setup can easily be modified to detect transmitted light. The nanostructure layout is based on the number of metallic dipole antennas aligned around one center, with the $\sim$ 100 nm gap in the center (see inset of Fig. 8.12). Each dipole antenna (two rods aligned along one direction) accepts the light with only one polarization direction: parallel to the longest side of the rod. The given dipole antenna creates the surface plasmons, localized in the gap between the two rods. This design works efficiently with circularly polarized light, that carries OAM and is in resonance with the nanorods. Whole antenna in this case creates the ring of light along the perimeter of the inner nanogap. The phase singularity point stays in the center of this ring creating characteristic intensity minimum [52]. As a result, the ring of light around the edges recreates the optical plasmon vortex. The size of the optical vortex depends on the size of the inner nanogap.

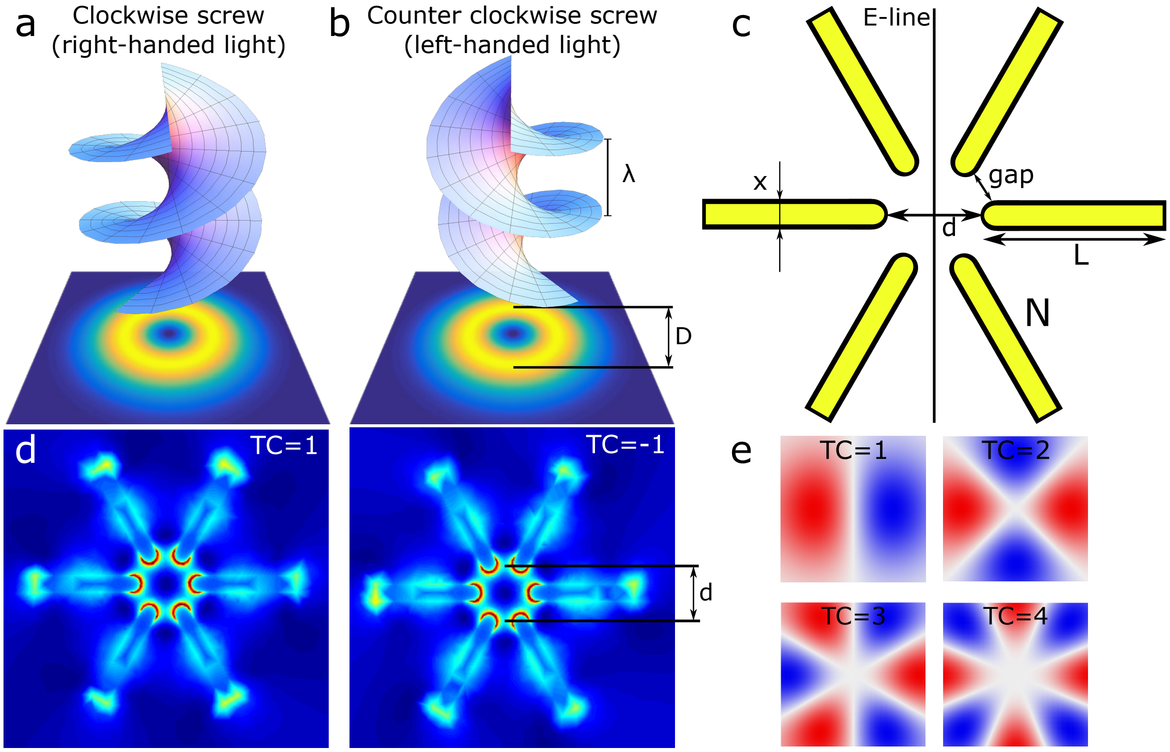

Figure 8.5: a: Right-handed and b: left-handed light wavefront with the resultant intensity (beam profile). D - diameter of the diffraction limited vortex. c: Geometrical layout of nanoantenna with the parameters to be optimized; x - thickness of one rod; d - diameter of inner area; gap - minimal distance between two rods; N - number of rods; L - length of the rod, E-line is the line where we measure antenna enhancement. d: An example of the field distribution, generated by the antenna c; ring, formed by high intensity in the center is a resultant plasmonic vortex with the diameter equal to the parameter d of nanoantenna c. e: 2D phase of optical vortices with TC=1,2,3,4. Color gradient varies from -2π(blue) 2π(red). White area in the center denotes the phase singularity point. The images are drawn not to scale.

Hence, by achieving the smallest nanogap size, we can reduce the size of the optical vortex to the size of the molecule, allowing for large electric field gradient and enabling the light interaction with the molecular internal degrees of freedom. In this work we optimize all the nanolens parameters for 532 nm wavelength and make the design easy to manufacture. We keep in mind both fabrication limitations and antenna efficiency, and compromise in between those two. We create a universal plasmonic structure, that is good for many purposes and focuses various beams with various parameters efficiently.

An efficient antenna should transfer certain properties of light (structure and phase profile) unchanged onto a nanoscale (Fig. 8.5 c). The proposed nanolens is made of gold, consists of *N* rods (*N* can vary) oriented along one center. Localized surface plasmons are being excited inside the rods, if illuminated by light. The characteristic sizes of the nanoantenna are smaller than the wavelength of light, which means that the excited plasmonic modes are highly discretized [214]. Therefore, resonant wavelengths of the nanoantenna strongly depend on the antenna geometry as well as nanoantenna-optical vortex positions. Resonant localized surface plasmons result in a strong light scattering in antinodes of plasmon (ends of rods). This scattering happens on the nearfield scale and spreads on $\sim$20 nm into the air around the rods. If we illuminate this structure with a resonant optical vortex light, the generated plasmons form the ring of light in the inner area of the antenna. This ring of light is equivalent to the diffraction limited optical vortex, but has a diameter of the inner area of nanoantenna. Essentially, the only parameter that defines the size of the generated plasmonic vortex is the diameter of the inner area, which makes the proposed design flexible: we can manufacture nanolens with lesser number of rods and the ring diameter will be naturally smaller.

We aim to make a universal nanolens design by optimizing it for optical vortices with different topological charges, TC=1,2,3,4, as well as for different handedness (TC=-1,-2,-3,-4). The optical vortices with different TCs have similar intensity distributions [49], but distinct phase profiles, Fig. 8.5 e. Optimizing the antenna designs for various TCs requires us to confirm the conservation of these singularity points and their order. Nanolens works equally well for right-handed and left-handed vortex 8.5 c.

First, we find the optimal rod size (*L*) for the nanolens to be in resonance with 532 nm incident wavelength. For this we vary the rod lengths keeping the incident light wavelength fixed for TC=1, and detect the maximum enhancement given by each of these lengths. Figure 8.6 a demonstrates that the gold nanolens with *N*=8 has periodic resonances, that are associated with the number of half-wavelengths fit on one rod length. For our nanolens we pick the brightest (1 wavelength) resonance. The rod length for this resonance is approximately equal to 240 nm, which is reasonably easy to manufacture and keeps the overall structure size large enough to avoid the nanolens being

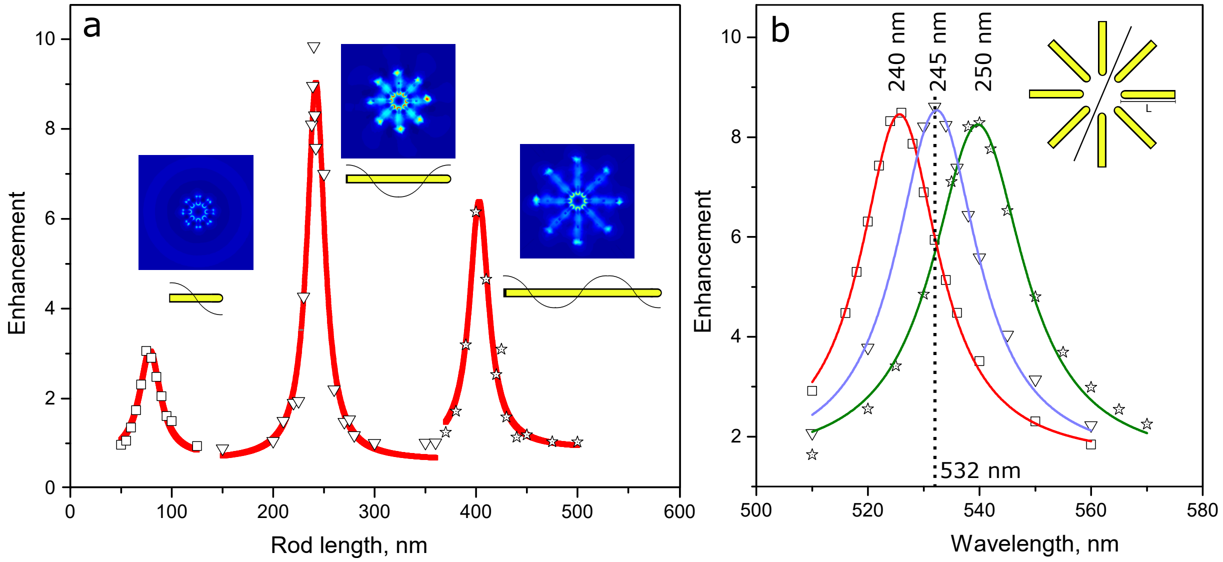

Figure 8.6: a: Length of rods (*L*) parameter optimization for 532 nm and TC = 1 incident laser beam on the antenna with 8 rods (*N* = 8). Three peaks show 1/2 wavelength, 1 wavelength and 3/2 wavelength resonance curves. b: Fine tuning of *L* parameter around 1 wavelength resonance in (a). 5 nm change in *L* moves the resonance peak by ∼ 8 nm.

completely inside the dark center of the diffraction limited optical vortex. Figure 8.6 b shows the dependence of the length rod on the resonance wavelength. In this figure we fix the rod length, and vary the wavelength to monitor how the resonance peak shifts. This also allows fine tuning the rod length of the optimal nanolens.

As we mentioned before, the localized surface plasmon causes intense light scattering in the nanolens antinodes, and spreads in the air around the rod on ∼20 nm. For easier manufacturing of the antenna, we want to keep the gap parameter close to 40 nm. This will ensure the stable ring brightness. Figure 8.7 a shows the dependence of the gap on the inner circle diameter (*d*), which reflects the diameter of the generated plasmon vortex. Linear dependence with slightly different slopes for different number of rods proves that the rods do not interact with each other. We estimate the performance of varying gap/inner ring diameter by detecting the lowest possible enhancement (in the middle between two rods) generated by antenna, Fig. 8.7 b. We see that the produced enhancement, as expected, decreases with the larger gap. However, it shows different behavior for different *N*.

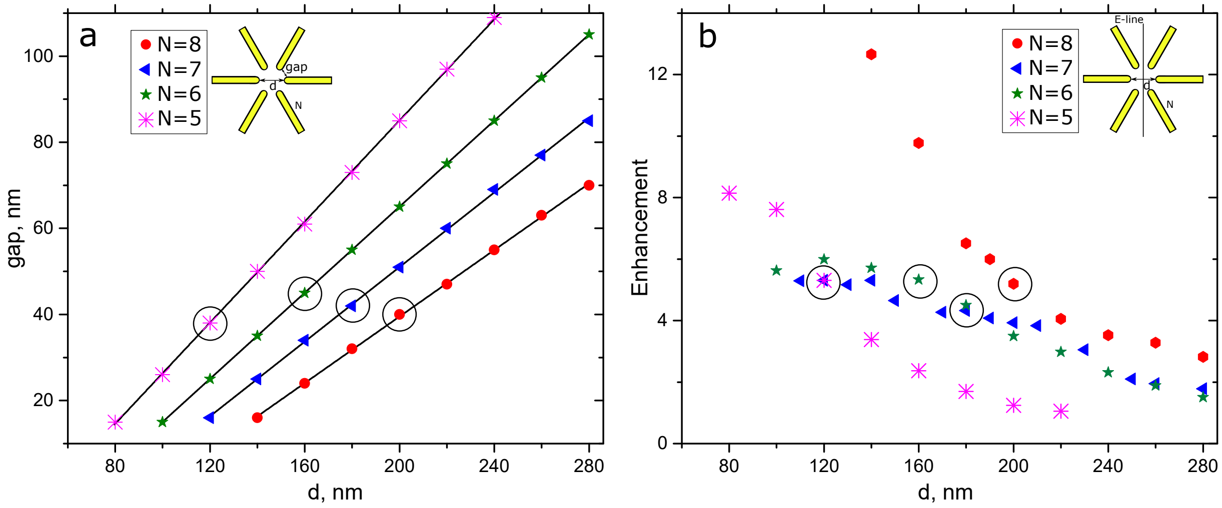

Figure 8.7: a: Gap length dependence on the inner area diameter (d). We pick the inner area diameter that corresponds to the gap = 25 nm for our prototypes. b: The antenna enhancement dependence on the diameter of the inner area (*d*). We measure the enhancement over the line between two rods and find a maximum value (on the inner ring).

Next we optimize a minimal number of rods antenna should have to transfer various TCs. To estimate the quality of focused light we pick two criteria:

- Brightness and evenness of the inner ring of light;
- Pronounced phase singularity point in the middle.

For both of these criteria we need to analyze the 2D intensity and phase distribution for various TCs. We consider the nanolenses with $N = 5,6,7,8$ and define the maximum TC, that each of these nanolenses can focus. We chose $N = 8$ to confirm that 8 rods nanolens works for TC = 1,2 as it was shown in [52], and prove, that this nanolens works for both handedness as well. Then, we want to reduce a number of rods in nanolens to simplify the manufacturing while maintaining functionality, and to reduce the inner area diameter to keep the plasmon vortex as small as possible.

We start with $N = 8$, depicted in Fig. 8.8. We pick the gap size to be around 40 nm, therefore, we use the optimal inner area diameter using Fig. 8.7. We check the quality of ring of light using the intensity distribution and the phase singularity using phase distribution. We also show the overall antenna enhancement along the white line (Fig. 8.8) to prove that antenna creates an

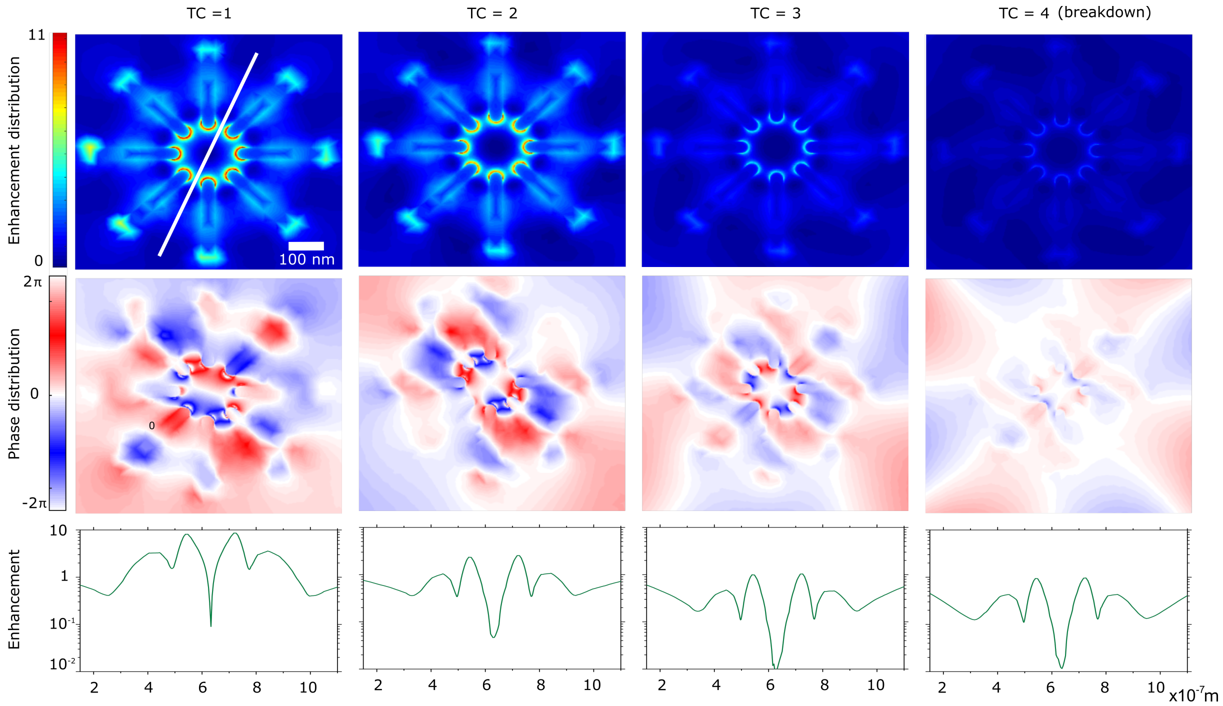

Figure 8.8: Top row: Intensity distributions for N = 8; λ =532 nm; gap = 40 nm; d = 200 nm; L = 245 nm; x = 40 nm. Middle row: Corresponding phase distribution. Color code is similar to Fig. 8.5 e indicating the presence of characteristic phase singularity. Bottom row: The antenna enhancement (log scale) measured along the white line (see top row). Antenna with N = 8 can successfully focus beams with TC = 1,2,3. When we try to focus TC = 4, the structure fails to reconstruct all 8 phase petals as in Fig.8.5 e.

optical vortex field profile with zero intensity in the center. For N = 8 we see, that the structure easily focuses the light with TC = 1,2, confirming the results from Ref. [52]. In addition, the same structure is capable of focusing TC = 3. When antenna is illuminated with optical vortex with TC = 4, we do not see a pronounced phase singularity point. There are a several reasons for that:

- The light beam diameter is significantly larger than the antenna;
- The antenna enhancement is insufficient;
- High order optical vortices become unstable at these scales and the high order singularity point breaks into several first order singularities that cannot be distinguished here.

Moving on to the antenna with N = 7, Fig. 8.9, we see that when optimized, it has comparable

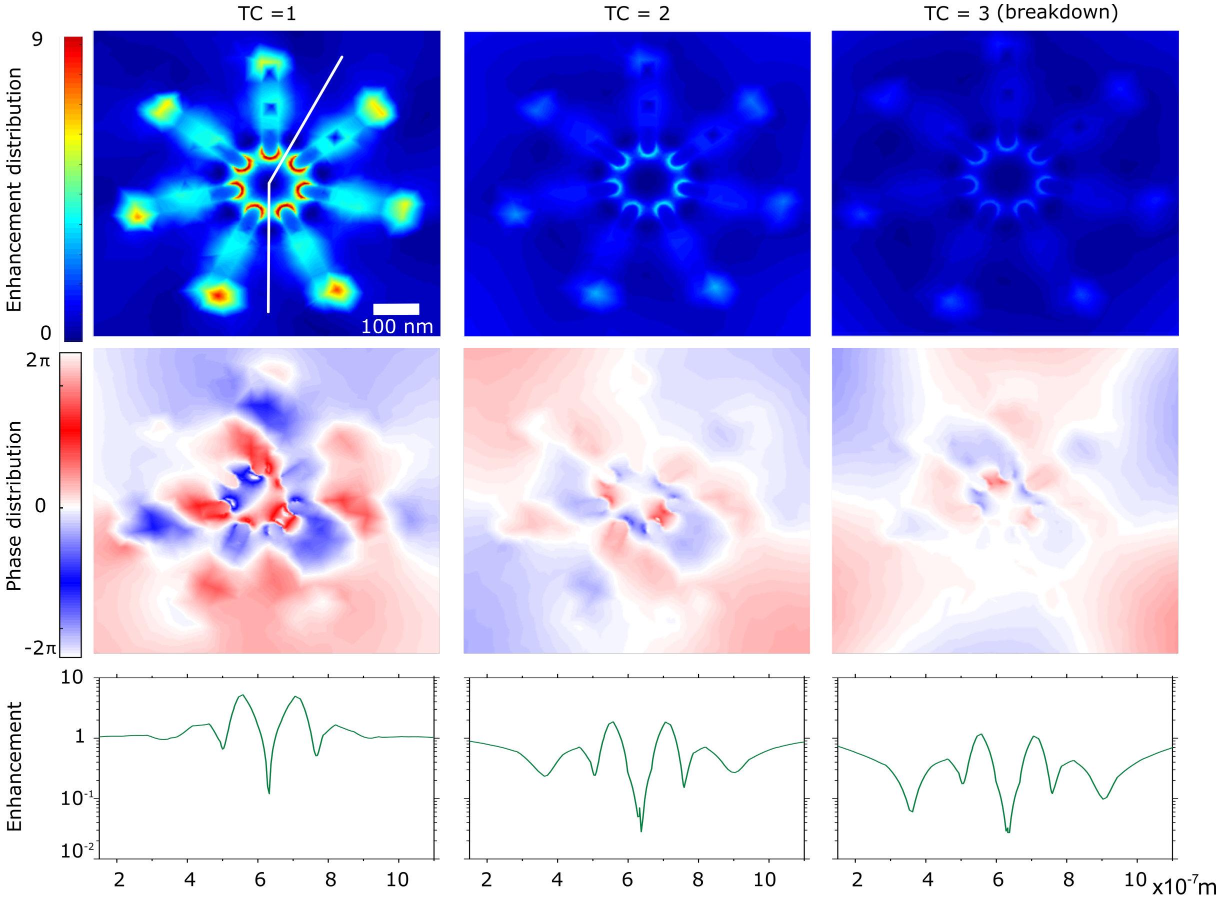

Figure 8.9: Top row: Intensity distributions for N = 7; λ =532 nm; gap = 40 nm; d = 180 nm; L = 245 nm; x = 30 nm. Middle row: Corresponding phase distribution. Color code is similar to Fig. 8.5 indicating the presence of the characteristic phase singularity. Bottom row: The antenna enhancement in a log scale measured along the white line (see top row). The antenna with N = 7 can successfully focus beams with TC = 1,2. When we try to focus TC = 3, the structure fail to reconstruct all 6 phase petals as in Fig.8.5.

enhancements with the N = 8 antenna. On the other hand, 7-rod antenna cannot focus vortex with TC = 3; on a phase profile picture we see the singularity point corresponding to TC = 2 instead. Performance of the antenna with N = 6, Fig. 8.10, in comparison with N = 7, shows larger enhancement and the same efficiency in terms of phase-profile transfer, it also gives smaller plasmonic vortex diameter. We check that nanolens with N = 6 works equally well for right-handed (TC = -1) and left-handed (TC = 1) vortex 8.5 c, and we conclude that all other nanolenses N = 8,7,5 would have the same property.

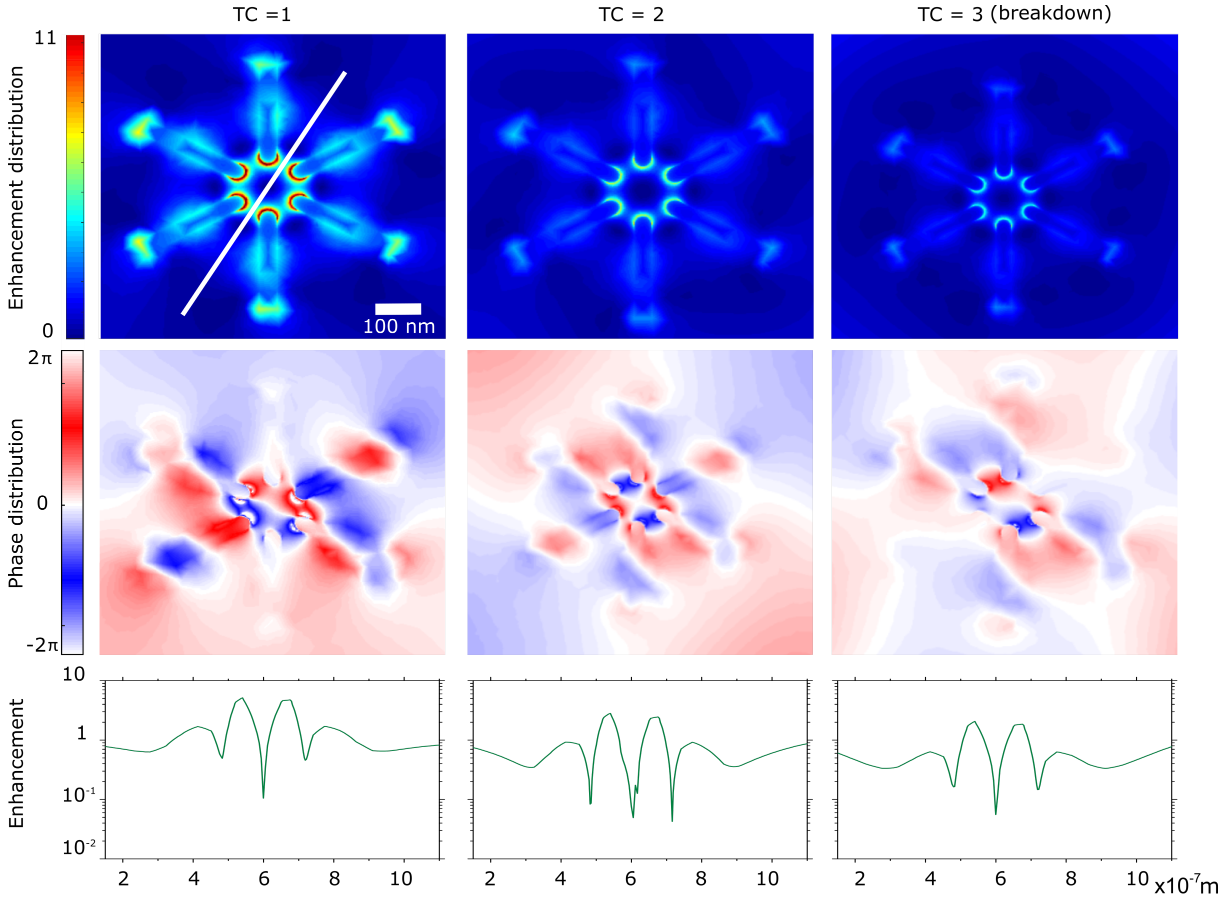

Figure 8.10: Top row: Intensity distributions for N = 6; λ =532 nm; gap = 40 nm; d = 160 nm; L = 240 nm;x = 40 nm. Middle row: Corresponding phase distribution. Color code is similar to Fig. 8.5 indicating the presence of characteristic phase singularity. Bottom row: The antenna enhancement (log scale) measured along the white line (see top row). The antenna with N = 6 can successfully focus beams with TC = 1,2. When we try to focus TC = 3, we can still see all 6 needed petals. However, they are not perfectly symmetric, which may affect the experimental results on a single molecule scale.

We perform finite element method (FEM) using COMSOL software. We illuminate the antenna with a circularly polarized optical vortex beam, propagating along the z axis. Its electric field in cylindrical coordinates can be represented as follows:

$$E(\rho,\phi,z,t) = E_0\frac{w_0\rho^{|m|}}{w^{|m|+1}}\exp\left[\frac{-\rho^2}{w^2}\right]\exp\Big[-i(|m|+1)\arctan\frac{z}{z_R}+\frac{ik\rho^2}{2R(z)}+i(m\phi+kz-wt)\Big], \tag{8.1}$$

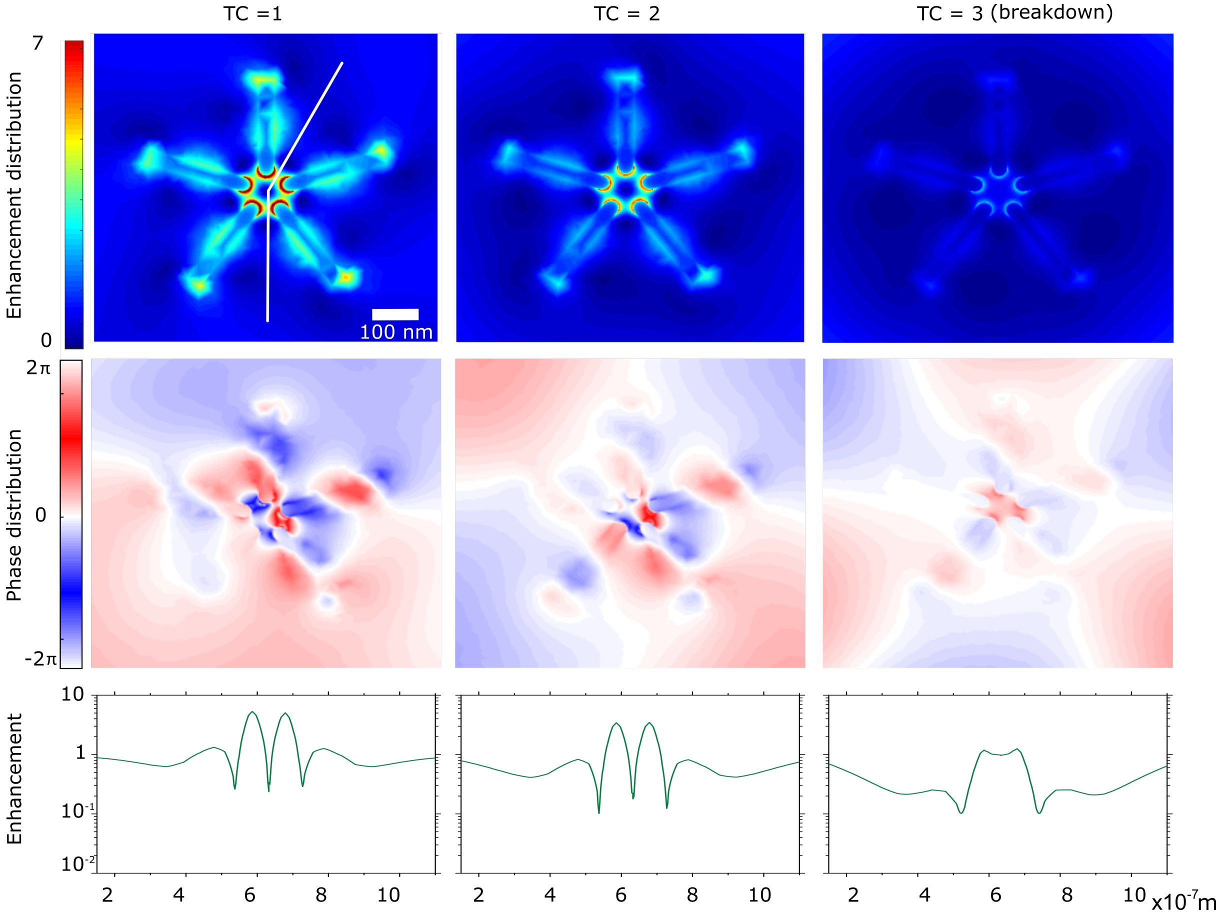

Figure 8.11: Top row: Intensity distributions for N = 7; λ =532 nm; gap = 40 nm; d = 120 nm; L = 240 nm; x = 40 nm. Middle row: Corresponding phase distribution. Color code is similar to Fig.8.5 e indicating the presence of characteristic phase singularity. Bottom row: The antenna enhancement (log scale) measured along the white line (see top row). The antenna with N = 5 can successfully focus beams with TC = 1,2. When we try to focus TC = 3, the structure fail to reconstruct all 6 phase petals as in Fig.8.5 e.

where ρ, ϕ are polar coordinates in the transverse plane; w_0 is the beam radius at the beam waist (at $z = 0$); E_0 is the amplitude parameter; $w = w_0(1 + z^2/z_R^2)^{1/2}$ is the transverse beam radius; $z_R = kw_0^2/2$ is the Rayleigh range; $R(z) = z(1 + z_R^2/z^2)$ is the radius of the wavefront curvature; m is the value of the TC; and k is the wavenumber [58]. When the height of the nanolens rods is fixed, h=50 nm, we detect the resultant field distribution at h_1=25 nm. We are interested in two values: electric field magnitude $|E| = \sqrt{E_x^2 + E_y^2 + E_z^2}$ (top rows in Figs. 8.8, 8.9, 8.10, 8.11) and phase $Im(E_x) + Im(E_y) + Im(E_z)$ (middle rows in Figs. 8.8, 8.9, 8.10, 8.11).

We estimate the focusing ability of the nanolens for each TC by dividing diameter of a diffraction limited optical vortex to the diameter of the inner area of the nanolens. For example, focusing ability of a nanolens with 5 rods, *d*=120 nm, w_0=800 nm, TC=1 equals to:

$$\frac{D}{d} = \frac{2w_0}{d}(\frac{|m|}{2})^{1/2} \approx 9, \tag{8.2}$$

where $D = 2w_0(|m|/2)^{1/2}$ is a diameter of an optical vortex at its beam waist [58]. For TC=2 the focusing ability of the same lens increases to 13. However, looking at Fig. 8.11, we see, that the increased focusing ability is compensated with the decreased field enhancement.

Thinner rods allow us to decrease the ring diameter even more, meaning that the nanovortex size can be pushed to be smaller. However, we noticed a few issues while trying to push these limits:

- Thinner rods distort the ring appearance and stability;
- When inner diameter is less than 50 nm, the intensity does not go to zero in the center;
- Very small inner diameter causes the rods oriented in the same direction interact with each other, which destroys the optical vortex;
- During manufacturing, thinner rods tend to appear more distorted, which makes the antenna enhancement less reliable.

We conclude from the simulation, that N=5 antenna with x=40 nm allows us to achieve the smallest ring diameter with the relevant enhancement.

8.2 Nanostructure design and fabrication

We have carried out initial fabrication trials using a focused ion beam (FIB) system. Figure 8.12 shows a nanoantenna with 8 rods. We have used FIB to mill Au substrates with a thickness of 50 nm. The width of each rod is 50 nm, the length of each rod is 500 nm, and the diameter of the central area is 300 nm. Fine structures can be fabricated using different parameters, including beam

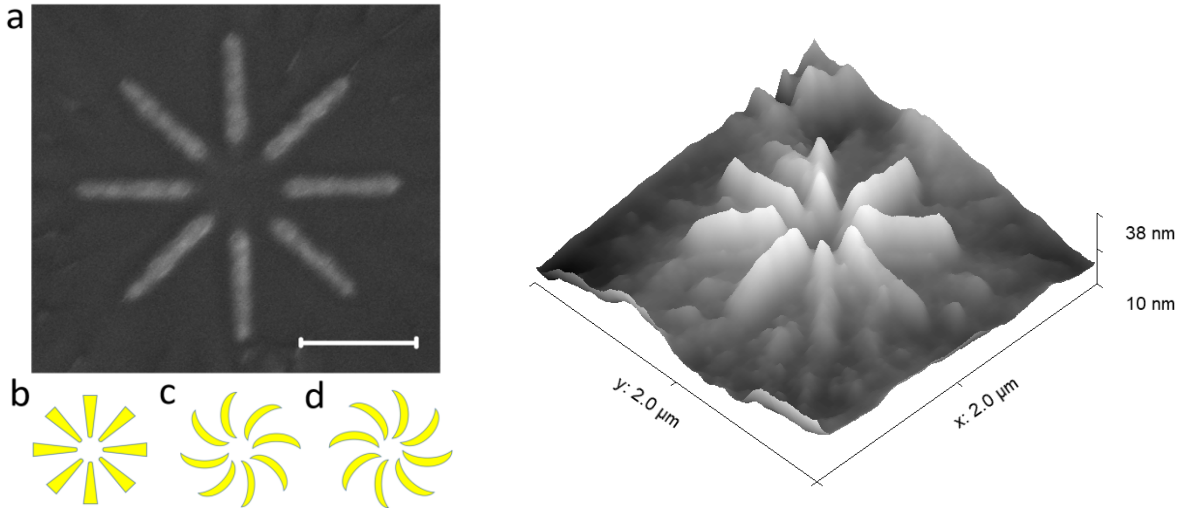

Figure 8.12: Right image: One simple OAM antenna design, with 8 rechtanglular rods; the scale bar is 500 nm; a is obtained with scanning electron microscope. We will also study other structures, *i.e.* b, c, d. Left image image: the same nanoantenna image obtained with the AFM microscope.

voltage, beam current, beam dwell time, beam passings, and the melting direction. To improve the performance of nanoantennas using light with OAM, we study different structures as shown in Fig. 8.12(b, c, d). The structure with 8 crescent rods as shown in Fig. 8.12(c, d) may lead to a stronger twisted light focusing effect. 30 kV Electron Beam Lithography (EBL) System (Raith Voyager) is also available at Baylor University. The image to the right in Fig. 8.12 is obtained using AFM (AIST, Horiba) to confirm the appearance and geometry of generated nanoantenna.

8.3 Experimental setup

We build an experimental setup, Fig.8.13, based on Raman microscope with spectrometer (Horiba iHR550) and Nanonics AFM microscope. We perform a modification of the input beam path by adding a flip platform with 2 mirrors to the initial setup to send the beam to the SLM (Hamamatsu). The SLM applies vortex shape to the laser (532 nm, Verdi, Coherent, Inc.) beam. For our experiment we need circularly polarized light, but the SLM accepts only linearly polarized light. Therefore, we place quarter-wave plate after the SLM which adds the circular polarization and does not disturb the optical vortex light mode. After that, the beam focuses through the micro-

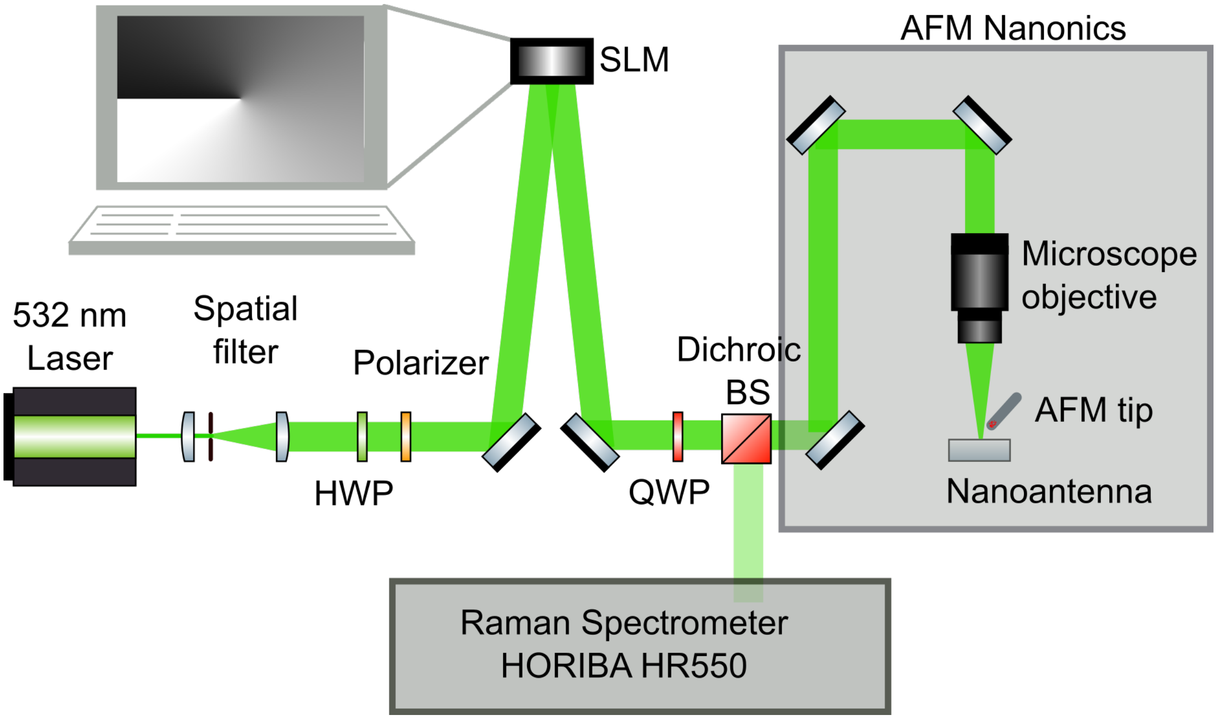

Figure 8.13: Experimental setup with 532 nm continuous wave laser. HWP — half wave plate, QWP -– quarter wave plate, Dichroic BS — dichroic beam splitter that sends Raman signal into the spectrometer.

scope objective (NA 0.45) onto the sample, where we can do both Raman imaging and AFM relief measurement.

Before making any subdiffraction optical field measurements we need to perform a system calibration and define all the initial parameters. First of all, we perform the beam size calibration. We use our standard Olympus microscope objective with numerical aperture (NA) 0.45, focus 532 nm CW laser beam and determine the FWHM size using an optical camera. Figure 8.14 shows the actual picture of Gaussian beam fit with Gaussian function. We fit the optical image with a Gaussian funcion and define the FWHM beam size, which is very close to the beam size measured in the experiment. With the optical camera and Gaussian fit we have beam width FWHM equal to 6 pixels, or 1.4 μm. This is far from the diffraction limit, but close to the ideal image that our objective can give.

After calibrating the experimental setup with Gaussian beam we switch to optical vortex. Fig-

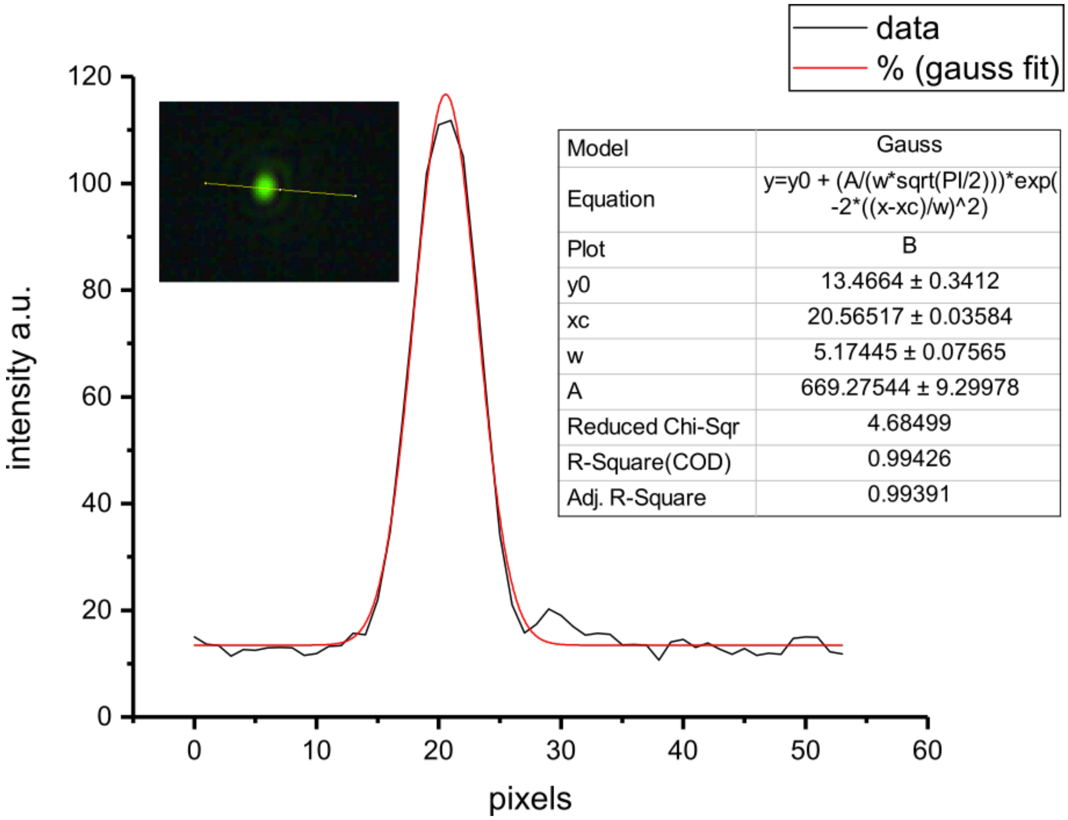

Model	Gauss
Equation	y=y0 + (A/(w*sqrt(PI/2)))*exp(-2*((x-xc)/w)^2)
Plot	B
y0	13.4664 ± 0.3412
xc	20.56517 ± 0.03584
w	5.17445 ± 0.07565
A	669.27544 ± 9.29978
Reduced Chi-Sqr	4.68499
R-Square(COD)	0.99426
Adj. R-Square	0.99391

Figure 8.14: The beam profile data obtained with the optical microscope. Left inset shows the beam picture, right inset depicts all the fitting parameters and errors. The graph shows the actual experimental data and its Gauss fitting.

ure 8.15 shows the optical vortex obtained with optical camera. By definition the optical vortex mode of light occupies larger area than Gaussian beam, which perfectly corresponds to our results. We fit the optical image with the ideal Laguerre-Gauss function and obtain the beam diameter FWHM 12 pixels, or 2.7 μm. As we see in the Fig., the optical vortex beam intensity does not reaches zero on the beam's axis. We assume, that the beam has non zero intensity because of the z-component of the optical field. Z-component arises from the non-flat wavefront at the focal point and can be corrected by adaptive wavefront algorithms, described in detail in previous chapters.

Our experimental setup is designed to be used in two configurations. The antenna-molecule system can be illuminated from above, and we can detect light scattered back to the objective. Alternatively, we can illuminate the antenna-molecule system from below, and detect the transmitted

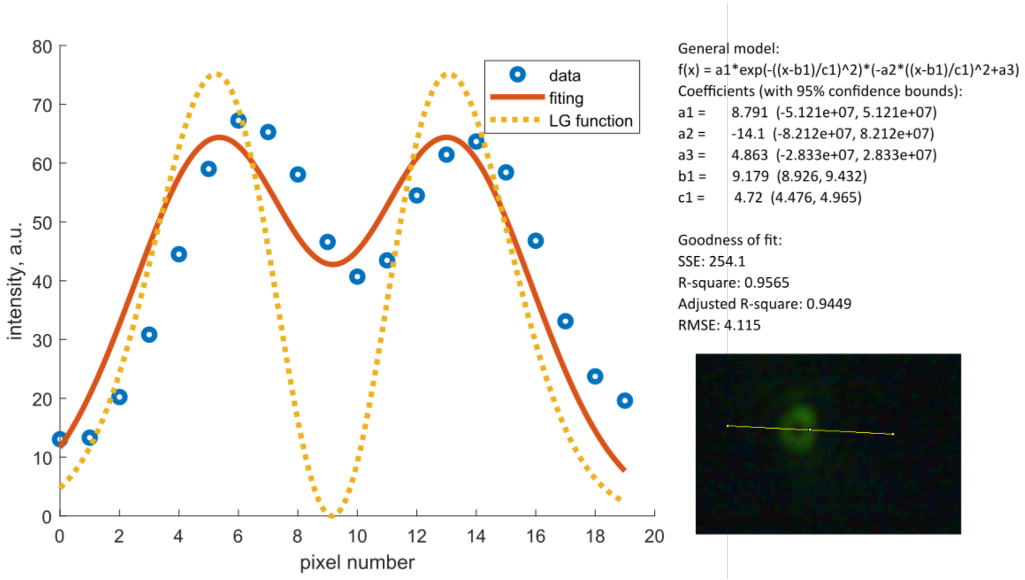

General model:
f(x) = a1*exp(-((x-b1)/c1)^2)*(-a2*((x-b1)/c1)^2+a3)
Coefficients (with 95% confidence bounds):

a1 =	8.791	(-5.121e+07, 5.121e+07)
a2 =	-14.1	(-8.212e+07, 8.212e+07)
a3 =	4.863	(-2.833e+07, 2.833e+07)
b1 =	9.179	(8.926, 9.432)
c1 =	4.72	(4.476, 4.965)

Goodness of fit:
SSE: 254.1
R-square: 0.9565
Adjusted R-square: 0.9449
RMSE: 4.115

Figure 8.15: The optical vortex beam profile data obtained with the optical microscope. Bottom inset shows the optical vortex beam picture, top inset depicts all the fitting parameters and errors. The graph shows the actual experimental data, its Laguerre-Gauss fitting (Gauss beam modulated with Laguerre polynomial), and an ideal Laguerre-Gauss function that has zero intensity on the beam axis.

light. There are some advantages and drawbacks associated with above and below illuminations. Above illumination unavoidably causes the appearance of AFM tip cantilever shadow, which partially covers the nanoantenna. Although the tip is very small and the shadow is unfocused, the glass itself serves as an additional optical element and modifies the incoming laser beam phase profile in an unpredictable way. Illumination from below does not have such a drawback. However, in this case, laser light goes through a slab of glass that reflects 5% of the target light signal back twice: from the back and the front surfaces. In addition, when using the functionalized AFM tip, it is usually more complicated to align the AFM system with the tip on the other side of the objective.

8.4 Tip functionalization and calibration

After we manufacture the nanostructure and build it into our experimental setup, we need to make sure the structure focuses light, conserving its spatial structure and OAM. Field detection technique, which allows us to do this with nanoresolution, was developed by the group of El-Khoury (see Ref.[215]). They use tip-enhanced Raman spectroscopy in order to map the topography of a silver film with very high resolution. For this they cover the AFM tip with Raman-active molecules. These molecules, when engaged with the silver surface, produce enhanced Raman signal, with the enhancement dependent upon the tip-surface distance. As a result, Raman signal shows the thin film topography with several-nanometer resolution. The modification of this method for our situation is the following: instead of mapping a nanotopography of a silver film, we probe the spatial distribution of the optical field with OAM. Similarly, the AFM tip covered by the Raman-active molecules can show variations in Raman signal, which will depend on the local field intensity. This technique, known as functionalized-tip enhanced Raman spectroscopy, was established in our group by Alajlan *et al.* in Ref. [216]. The functionalized tip approach allows us to suppress the background and is ideal for separating electromagnetic and chemical enhancement mechanisms on various substrates. Tip can be functionalized by scanning the surface covered by Raman-active molecules and taking the measurements of electrical field and phase distributions for the beams with and without OAM. The measurements of phase and field oscillations can be also carried out with the apertureless near-field scanning optical microscopy [217, 218] or a similar technique which is able to measure optical fields with nanometer precision [215].

8.4.1 Tip image by deconvolution

The shape of the AFM tip can significantly affect the quality and relief of imaging plane. In the worst case it can totally smear the key features that need to be measured. To avoid this and define a reasonable resolution, we need to know the shape of the tip. For this we obtain an AFM image of the calibration sample, which consists of many nano pillars. The nanopillars have a shape similar to the AFM tip. We analyze the obtained AFM image by doing its deconvolution, keeping in mind known parameters of the calibration sample. As a result, we get a reliable tip shape estimation, which can be confirmed with several different images of the calibration sample. To do this "blind tip shape estimation" we use GWYDDION software Fig. 8.16. Tip shapes from different AFMs that were used for measurements: Horiba AIST and Nanonics.

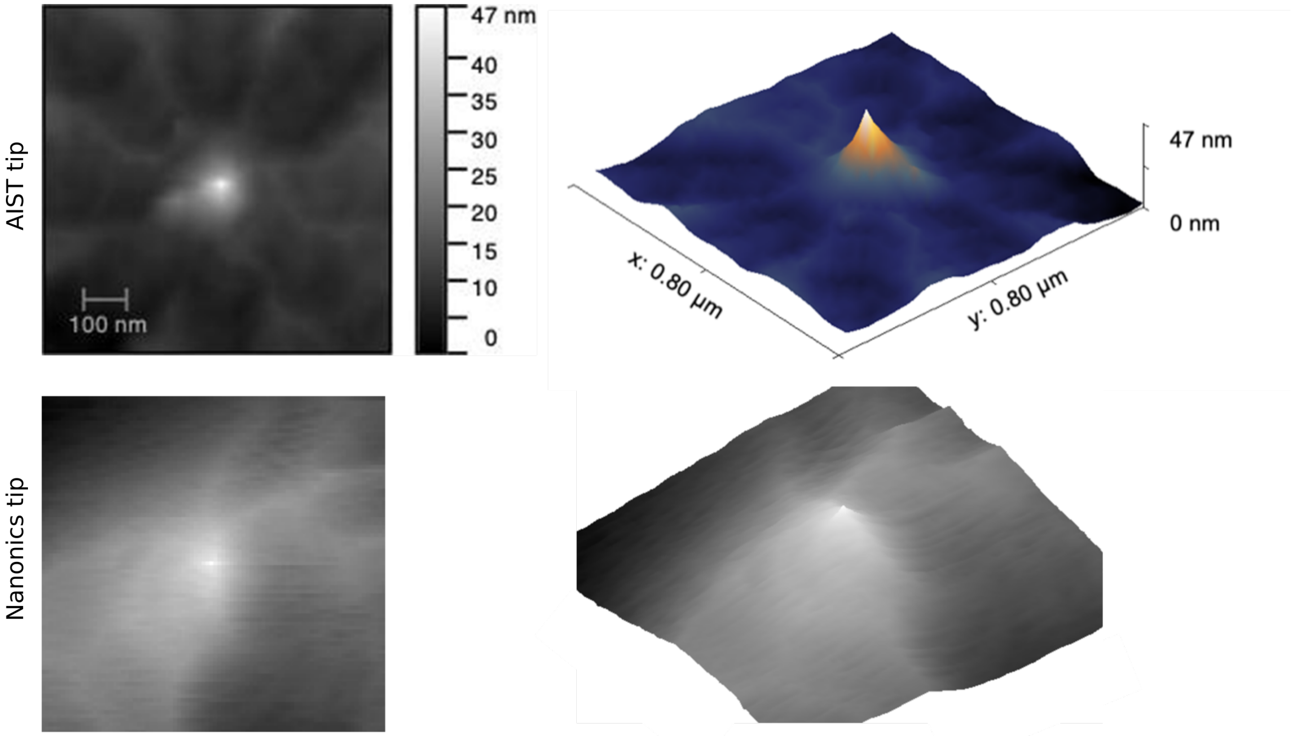

Figure 8.16: Shape of the AFM tips, obtained from the AFM images by "blind tip shape estimation" using GWYDDION software. Top row shows 2D and 3D images of metallic AFM tip of AIST microscope, and the bottom row shows 2D and 3D images of quartz AFM tip of Nanonics microscope. We can see that AIST tip is sharper, therefore it ensures better resolution.

8.4.2 Chiral molecules

To test the developed system we we can use solutions of simple and well-known chiral molecules, e.g. limonene and propylene oxide (epoxypropane), available from Sigma Aldrich. We can drop a small amount in the center of nanostructure and detect the scattered signal difference between right- and left-handed light. However, this method does not give single molecule resolution and does not have a way to extract information about molecule positions.

The commonly used single test object for probing forbidden transitions is a quantum dot. A quantum dot can be designed to have a forbidden transition within the desired wavelength range and their transitions widely studied both theoretically [219, 220] and in the experiment [221], using near-field microscopy. With the extensive studies available we can compare the probability transition rates experimentally with (a) Gaussian beam, (b) diffraction limited optical vortex and (c) with nanosized optical vortex. This study will calibrate the system with a well-studied test object.

Alternatively, we can test and calibrate the system before actually using chiral molecules. We can check its capability to interact with nanodiamonds, since these are relatively easy to grow in small sizes and have many dipole-forbidden magnetic and quadrupole transitions. Nanodiamonds are widely used for nanoscale sensing/imaging techniques that utilize the magnetically-sensitive nitrogen-vacancy (NV) color center [222, 223]. These NV sensors benefit from the quantized nature of single spins [224]. Commercially available nanodiamonds with color centers can serve as high quality test particles for magnetic transitions. Furthermore, a novel method of growing nanodiamonds of higher quality, free from magnetic impurities and strain, was developed by Prof. Hemmer's group at Texas A&M University. These nanodiamonds will serve as test particles to be integrated with plasmonic nanostructures for probing forbidden transitions [225].

When the system is calibrated and shows pronounced results, we move on to the well-developed chemical procedure, called tip biofunctionalization [226, 205]. This procedure involves creating tip-bound sensor molecules, by attaching the biomolecule of interest to the AFM tip through a couple of cross-link molecules, usually linear polymers, e.g. carboxymethylamylose, poly-(N-succinimidyl acrylate), or poly(ethylene glycol). The procedure of attaching amino groups (e.g. mitochondrial uncoupling protein 1 (UCP1), [205]), that are chiral by definition, is called amino-functionalization, and described in details in literature [227]. First, reactive sites are generated on the tip surface. Second, a linear polymer (cross-linker) is attached with one reactive end while reserving the other end for the probe molecule. Then the probe molecule is coupled to the free end of the linear polymer chain. As a result of this procedure the AFM tip will have single protein on its end. We can precisely move the tip to the center of the nanoantenna and detect any absorption or fluorescence signal with the optical vortex light field created by the antenna.

To employ the apparatus for studies of DNA molecules, there are many well-developed options: nanofluidics and combination of antenna with nanopore to DNA translocate through nanopore in the middle of antenna [228]; immobilize and dry the DNA double strand molecule, straighten it on the surface, chop into short pieces and put one in the middle of nanoantenna[229].

8.5 Conclusions

The experimental instrumentation, methods and algorithms, developed in this chapter, allow us to introduce a novel type of spectroscopy and imaging using the electric quadrupole and magnetic transitions. This will give us new information about internal degrees of freedom of the molecules along with what is already known from vibrational and rotational spectroscopy, completing our knowledge about biologically-relevant molecules and opening new possibilities for control of molecular processes. Moreover, probing magnetic transitions with nanodiamonds will allow for accurate magnetic field mapping.

This chapter develops a way to study chirality with the optical vortices, since light with OAM is also left- and right-handed. We use plasmonic nanoantennas designed to preserve the chirality of light, while confining it into the nanometer-sized volume containing the molecules of interest. In this case dipole-forbidden optical transitions will become as strong as allowed ones. This arrangement provides a tool to study the interaction of light with OAM with chiral molecules. Our main goal is to see molecules absorb and/or emit OAM photons. The study of chiral OAM-light-matter interactions in combination with other spectroscopic techniques can potentially become a new tool for the ultimate-precision single-molecule characterization.

Applications of the described technique range from fundamental physics (probing forbidden transitions) to applied physics, biology (chirality), and genetics (DNA sequencing). Mastering this spectroscopic method and developing a technology would make a new range of phenomena accessible to experimental studies.

9. SUMMARY

In this work we discussed the various types of the wavefront shaping of laser beams and their effect on spectroscopic measurements and nonlinear optics processeses. We described how to create optical channels by wavefront shaping to guide plasma. We discussed different methods to implement optical shaping such as SLM, phase plates and the dynamic feedback loops. We developed a novel tool to enhance coherent cascaded Raman scattering in crystals, which will help to create shorter and more energetic coherent white light sources essential for tracing electron dynamics and controlling multiphoton ionization. We proved that spatial wavefront shaping can alter the efficiency of SERS spectroscopy.

We created and developed all necessary instrumentation and built the experimental environment for an ultimately new spectroscopy tool that can be used to discriminate between left- and right-handed chiral molecules on single molecule scale and allow us to study dipole forbidden molecular transitions.

To summarize, we proved the great importance of the spatial beam shaping (wavefront shaping) to the field of microscopy, nonlinear optics, and fundamental physics. New techniques we developed here are powerful and can be applied to real life experiments, and a vast number of future projects can be extended from this research. There are many more mysteries, such as chirality, we tried to address here that are yet to be solved.

REFERENCES

[1] R. Davies and M. Kasper, “Adaptive optics for astronomy,” *Annual Review of Astronomy and Astrophysics*, vol. 50, pp. 305–351, 2012.

[2] F. Merkle, P. Kern, P. Léna, F. Rigaut, J. Fontanella, G. Rousset, C. Boyer, J. Gaffard, and P. Jagourel, “Successful tests of adaptive optics.,” *The Messenger*, vol. 58, pp. 1–4, 1989.

[3] G. D. Love, “Wave-front correction and production of zernike modes with a liquid-crystal spatial light modulator,” *Appl. Opt.*, vol. 36, pp. 1517–1524, Mar 1997.

[4] N. Ji, “Adaptive optical fluorescence microscopy,” *Nature Methods*, vol. 14, no. 4, p. 374, 2017.

[5] M. A. Vorontsov and G. W. Carhart, “Adaptive phase distortion correction in strong speckle-modulation conditions,” *Opt. Lett.*, vol. 27, pp. 2155–2157, Dec 2002.

[6] M. A. Vorontsov, G. W. Carhart, and J. C. Ricklin, “Adaptive phase-distortion correction based on parallel gradient-descent optimization,” *Opt. Lett.*, vol. 22, pp. 907–909, Jun 1997.

[7] I. M. Vellekoop and A. P. Mosk, “Focusing coherent light through opaque strongly scattering media,” *Opt. Lett.*, vol. 32, pp. 2309–2311, Aug 2007.

[8] I. M. Vellekoop, E. Van Putten, A. Lagendijk, and A. Mosk, “Demixing light paths inside disordered metamaterials,” *Optics express*, vol. 16, no. 1, pp. 67–80, 2008.

[9] J. Thompson, B. Hokr, and V. Yakovlev, “Optimization of focusing through scattering media using the continuous sequential algorithm,” *Journal of Modern Optics*, vol. 63, no. 1, pp. 80–84, 2016.

[10] I. M. Vellekoop, “Feedback-based wavefront shaping,” *Optics Express*, vol. 23, no. 9, p. 12189, 2015.

[11] B. H. Hokr, J. N. Bixler, M. T. Cone, J. D. Mason, H. T. Beier, G. D. Noojin, G. I. Petrov, L. a. Golovan, R. J. Thomas, B. a. Rockwell, and V. V. Yakovlev, "Bright emission from a random Raman laser.," *Nature Communications*, vol. 5, p. 4356, 2014.

[12] A. A. Zhdanova, Y. Shen, J. V. Thompson, M. O. Scully, V. V. Yakovlev, and A. V. Sokolov, "Controlled Supercontinua via Spatial Beam Shaping," *arXiv:1705.10457*, 2017.

[13] J. V. Thompson, G. A. Throckmorton, B. H. Hokr, and V. V. Yakovlev, "Wavefront shaping enhanced Raman scattering in a turbid medium," *Optics Letters*, vol. 41, no. 8, pp. 1769–1772, 2016.

[14] J. V. Thompson, B. H. Hokr, G. A. Throckmorton, D. Wang, M. O. Scully, and V. V. Yakovlev, "Enhanced second harmonic generation efficiency via wavefront shaping," *ACS Photonics*, vol. 4, no. 7, pp. 1790–1796, 2017.

[15] O. Tzang, A. M. Caravaca-Aguirre, K. Wagner, and R. Piestun, "Adaptive wavefront shaping for controlling nonlinear multimode interactions in optical fibres," *Nature Photonics*, p. 1, 2018.

[16] X. Xu, H. Liu, and L. V. Wang, "Time-reversed ultrasonically encoded optical focusing into scattering media," *Nature photonics*, vol. 5, no. 3, p. 154, 2011.

[17] A. Wright, S. Poland, J. Girkin, C. Freudiger, C. Evans, and X. Xie, "Adaptive optics for enhanced signal in cars microscopy," *Optics express*, vol. 15, no. 26, pp. 18209–18219, 2007.

[18] M. Fleischmann, P. Hendra, and A. McQuillan, "Chemical physics letters," *J*, vol. 26, p. 163, 1974.

[19] G. C. Schatz, M. A. Young, and R. P. Van Duyne, "Electromagnetic mechanism of sers," in *Surface-enhanced Raman scattering*, pp. 19–45, Springer, 2006.

[20] T. R. Jensen, M. L. Duval, K. L. Kelly, A. A. Lazarides, G. C. Schatz, and R. P. Van Duyne, "Nanosphere lithography: effect of the external dielectric medium on the surface plasmon

resonance spectrum of a periodic array of silver nanoparticles," *The Journal of Physical Chemistry B*, vol. 103, no. 45, pp. 9846–9853, 1999.

[21] M. D. Malinsky, K. L. Kelly, G. C. Schatz, and R. P. Van Duyne, "Chain length dependence and sensing capabilities of the localized surface plasmon resonance of silver nanoparticles chemically modified with alkanethiol self-assembled monolayers," *Journal of the American Chemical Society*, vol. 123, no. 7, pp. 1471–1482, 2001.

[22] L. J. Sherry, S.-H. Chang, G. C. Schatz, R. P. Van Duyne, B. J. Wiley, and Y. Xia, "Localized surface plasmon resonance spectroscopy of single silver nanocubes," *Nano letters*, vol. 5, no. 10, pp. 2034–2038, 2005.

[23] K. Kneipp, Y. Wang, H. Kneipp, L. T. Perelman, I. Itzkan, R. R. Dasari, and M. S. Feld, "Single molecule detection using surface-enhanced Raman scattering (SERS)," *Physical Review Letters*, vol. 78, no. 9, p. 1667, 1997.

[24] J. Liao, X. Wang, W. Sun, Y. Tan, D. Kong, Y. Nie, J. Qi, H. Jia, J. Liu, J. Yang, *et al.*, "Analysis of femtosecond optical vortex beam generated by direct wave-front modulation," *Optical Engineering*, vol. 52, no. 10, p. 106102, 2013.

[25] H. Ma, Z. Liu, H. Wu, X. Xu, and J. Chen, "Adaptive correction of vortex laser beam in a closed-loop system with phase only liquid crystal spatial light modulator," *Optics Communications*, vol. 285, no. 6, pp. 859–863, 2012.

[26] W. Lee, X.-C. Yuan, and K. Dholakia, "Experimental observation of optical vortex evolution in a gaussian beam with an embedded fractional phase step," *Optics Communications*, vol. 239, no. 1-3, pp. 129–135, 2004.

[27] M. Padgett, J. Courtial, and L. Allen, "Light's orbital angular momentum," *Physics Today*, vol. 57, no. 5, pp. 35–40, 2004.

[28] M. Zhi, K. Wang, X. Hua, H. Schuessler, J. Strohaber, and A. V. Sokolov, "Generation of femtosecond optical vortices by molecular modulation in a Raman-active crystal," *Optics Express*, vol. 21, no. 23, pp. 27750–27758, 2013.

[29] J. Strohaber, M. Zhi, A. V. Sokolov, A. A. Kolomenskii, G. G. Paulus, and H. A. Schuessler, "Coherent transfer of optical orbital angular momentum in multi-order Raman sideband generation," *Opt. Lett.*, vol. 37, no. 16, pp. 3411–3413, 2012.

[30] K. Dholakia, N. Simpson, M. Padgett, and L. Allen, "Second-harmonic generation and the orbital angular momentum of light," *Physical Review A*, vol. 54, no. 5, p. R3742, 1996.

[31] J. F. Nye and M. V. Berry, "Dislocations in wave trains," *Proceedings of the Royal Society of London. A. Mathematical and Physical Sciences*, vol. 336, no. 1605, pp. 165–190, 1974.

[32] A. M. Yao and M. J. Padgett, "Orbital angular momentum: origins, behavior and applications," *Advances in Optics and Photonics*, vol. 3, no. 2, pp. 161–204, 2011.

[33] H. He, M. Friese, N. Heckenberg, and H. Rubinsztein-Dunlop, "Direct observation of transfer of angular momentum to absorptive particles from a laser beam with a phase singularity," *Physical review letters*, vol. 75, no. 5, p. 826, 1995.

[34] A. M. Akulshin, R. J. McLean, E. E. Mikhailov, and I. Novikova, "Distinguishing nonlinear processes in atomic media via orbital angular momentum transfer," *Optics letters*, vol. 40, no. 6, pp. 1109–1112, 2015.

[35] F. M. Fazal and S. M. Block, "Optical tweezers study life under tension," *Nature photonics*, vol. 5, no. 6, p. 318, 2011.

[36] M. J. Padgett, "Light in a twist: optical angular momentum," *Proceedings of SPIE*, vol. 8637, p. 863702, 2013.

[37] D. G. Grier, "A revolution in optical manipulation," *Nature*, vol. 424, pp. 810–816, 2003.

[38] S. W. Hell and J. Wichmann, "Breaking the diffraction resolution limit by stimulated emission: stimulated-emission-depletion fluorescence microscopy," *Optics letters*, vol. 19, no. 11, pp. 780–782, 1994.

[39] T. A. Klar, E. Engel, and S. W. Hell, “Breaking abbe’s diffraction resolution limit in fluorescence microscopy with stimulated emission depletion beams of various shapes,” *Physical Review E*, vol. 64, no. 6, p. 066613, 2001.

[40] G. A. Swartzlander, “Peering into darkness with a vortex spatial filter,” *Optics Letters*, vol. 26, no. 8, pp. 497–499, 2001.

[41] G. Foo, D. M. Palacios, and G. A. Swartzlander Jr, “Optical vortex coronagraph,” *Optics Letters*, vol. 30, no. 24, pp. 3308–3310, 2005.

[42] A. Mair, A. Vaziri, G. Weihs, and A. Zeilinger, “Entanglement of the orbital angular momentum states of photons,” *Nature*, vol. 412, no. 6844, p. 313, 2001.

[43] G. Gibson, J. Courtial, M. J. Padgett, M. Vasnetsov, V. Pas’ko, S. M. Barnett, and S. Franke-Arnold, “Free-space information transfer using light beams carrying orbital angular momentum,” *Optics express*, vol. 12, no. 22, pp. 5448–5456, 2004.

[44] C.-S. Guo, L.-L. Lu, and H.-T. Wang, “Characterizing topological charge of optical vortices by using an annular aperture,” *Optics Letters*, vol. 34, no. 23, pp. 3686–3688, 2009.

[45] Y. Peng, X.-T. Gan, P. Ju, Y.-D. Wang, and J.-L. Zhao, “Measuring Topological Charges of Optical Vortices with Multi-Singularity Using a Cylindrical Lens,” *Chinese Physics Letters*, vol. 32, no. 2, p. 024201, 2015.

[46] M. Harris, C. Hill, P. Tapster, and J. Vaughan, “Laser modes with helical wave fronts,” *Physical Review A*, vol. 49, no. 4, p. 3119, 1994.

[47] P. Vaity, J. Banerji, and R. Singh, “Measuring the topological charge of an optical vortex by using a tilted convex lens,” *Physics Letters A*, vol. 377, pp. 1154–1156, jun 2013.

[48] W. Buono, L. Moraes, J. Huguenin, C. Souza, and A. Khoury, “Arbitrary orbital angular momentum addition in second harmonic generation,” *New Journal of Physics*, vol. 16, no. 9, p. 093041, 2014.

[49] M. Shutova, A. A. Zhdanova, and A. V. Sokolov, “Detection of mixed oam states via vortex breakup,” *Physics Letters A*, vol. 381, no. 4, pp. 408–412, 2017.

[50] A. A. Zhdanova, M. Shutova, A. Bahari, and A. V. Sokolov, “Topological charge algebra of optical vortices in nonlinear interactions,” *Optics Express*, vol. 23, no. 26, pp. 34109–34117, 2015.

[51] M. Shutova, A. D. Shutov, and A. V. Sokolov, “Spectroscopic sensing enhanced by quantum molecular coherence and by plasmonic nanoantennas,” in *Optical, Opto-Atomic, and Entanglement-Enhanced Precision Metrology II*, vol. 11296, p. 1129605, International Society for Optics and Photonics, 2020.

[52] R. W. Heeres and V. Zwiller, “Subwavelength focusing of light with orbital angular momentum,” *Nano letters*, vol. 14, no. 8, pp. 4598–4601, 2014.

[53] T. Arikawa, S. Morimoto, and K. Tanaka, “Focusing light with orbital angular momentum by circular array antenna,” *Optics Express*, vol. 25, no. 12, pp. 13728–13735, 2017.

[54] M. Shutova, Z. Liege, A. Goltsov, A. Morozov, and A. V. Sokolov, “Binary phase plate for high-intensity non-diffracting hollow beam structure,” *JOSA B*, vol. 36, no. 5, pp. 1313–1319, 2019.

[55] J. Vaughan and D. Willetts, “Interference properties of a light beam having a helical wave surface,” *Optics Communications*, vol. 30, no. 3, pp. 263–267, 1979.

[56] E. Abramochkin and V. Volostnikov, “Beam transformations and nontransformed beams,” *Optics Communications*, vol. 83, no. 1-2, pp. 123–135, 1991.

[57] V. Kruglov and R. Vlasov, “Spiral self-trapping propagation of optical beams in media with cubic nonlinearity,” *Physics Letters A*, vol. 111, no. 8-9, pp. 401–404, 1985.

[58] M. V. Vasnetsov and K. Staliunas, *Optical Vortices (Horizons in World Physics Volume 228)*. Nova Science Publishers, Inc., 1999.

[59] L. Allen, M. J. Padgett, and M. Babiker, "The Orbital Angular Momentum Of Light," *Progress in Optics*, vol. 39, pp. 291–372, 1999.

[60] A. Bekshaev, M. Soskin, and M. Vasnetsov, "Paraxial light beams with angular momentum," *arXiv preprint arXiv:0801.2309*, 2008.

[61] J. W. Simmons and M. J. Guttmann, "States, waves, and photons: A modern introduction to light.," *States, waves, and photons: A modern introduction to light., by Simmons, JW; Guttmann, MJ. Reading, MA (USA): Addison-Wesley, 279 p.*, 1970.

[62] R. C. Devlin, A. Ambrosio, D. Wintz, S. L. Oscurato, A. Y. Zhu, M. Khorasaninejad, J. Oh, P. Maddalena, and F. Capasso, "Spin-to-orbital angular momentum conversion in dielectric metasurfaces," *Optics express*, vol. 25, no. 1, pp. 377–393, 2017.

[63] K. T. McDonald, "Bessel beams," *arXiv preprint physics/0006046*, 2000.

[64] R. Jáuregui, "Rotational effects of twisted light on atoms beyond the paraxial approximation," *Physical Review A*, vol. 70, no. 3, p. 033415, 2004.

[65] A. Alexandrescu, E. Di Fabrizio, and D. Cojoc, "Electronic and centre of mass transitions driven by laguerre–gaussian beams," *Journal of Optics B: Quantum and Semiclassical Optics*, vol. 7, no. 4, p. 87, 2005.

[66] M. Babiker, C. R. Bennett, D. L. Andrews, and L. C. Dávila Romero, "Orbital angular momentum exchange in the interaction of twisted light with molecules," *Physical Review Letters*, vol. 89, no. 14, p. 143601, 2002.

[67] R. Jáuregui, "Control of atomic transition rates via laser-light shaping," *Physical Review A*, vol. 91, no. 4, p. 043842, 2015.

[68] A. Afanasev, C. E. Carlson, C. T. Schmiegelow, J. Schulz, F. Schmidt-Kaler, and M. Solyanik, "Experimental verification of position-dependent angular-momentum selection rules for absorption of twisted light by a bound electron," *New Journal of Physics*, vol. 20, no. 2, p. 023032, 2018.

[69] C. T. Schmiegelow, J. Schulz, H. Kaufmann, T. Ruster, U. G. Poschinger, and F. Schmidt-Kaler, "Transfer of optical orbital angular momentum to a bound electron," *Nature communications*, vol. 7, p. 12998, 2016.

[70] R. P. Cameron, J. B. Götte, S. M. Barnett, and A. M. Yao, "Chirality and the angular momentum of light," *Phil. Trans. R. Soc. A*, vol. 375, no. 2087, p. 20150433, 2017.

[71] K. A. Forbes and D. L. Andrews, "Spin-orbit interactions and chiroptical effects engaging orbital angular momentum of twisted light in chiral and achiral media," *Physical Review A*, vol. 99, no. 2, p. 023837, 2019.

[72] D. L. Andrews, L. D. Romero, and M. Babiker, "On optical vortex interactions with chiral matter," *Optics communications*, vol. 237, no. 1-3, pp. 133–139, 2004.

[73] F. Araoka, T. Verbiest, K. Clays, and A. Persoons, "Interactions of twisted light with chiral molecules: An experimental investigation," *Physical Review A*, vol. 71, no. 5, p. 055401, 2005.

[74] K. A. Forbes and D. L. Andrews, "Enhanced optical activity using the orbital angular momentum of structured light," *Physical Review Research*, vol. 1, no. 3, p. 033080, 2019.

[75] R. W. Boyd, *Nonlinear optics*. Academic press, 2003.

[76] I. Mariyenko, J. Strohaber, and C. Uiterwaal, "Creation of optical vortices in femtosecond pulses," *Optics express*, vol. 13, no. 19, pp. 7599–7608, 2005.

[77] F. Lenzini, S. Residori, F. Arecchi, and U. Bortolozzo, "Optical vortex interaction and generation via nonlinear wave mixing," *Physical Review A*, vol. 84, no. 6, p. 061801, 2011.

[78] A. V. Sokolov and S. E. Harris, "Ultrashort pulse generation by molecular modulation," *Journal of Optics B-Quantum and Semiclassical Optics*, vol. 5, no. 1, pp. R1–R26, 2003.

[79] M. Zhi, *Broadband coherent light generation in Raman-active crystals driven by femtosecond laser fields*. Texas A&M University, 2007.

[80] A. V. Sokolov, M. Y. Shverdin, D. R. Walker, D. D. Yavuz §, a. M. Burzo, G. Y. Yin, and S. E. Harris, "Generation and control of femtosecond pulses by molecular modulation," *Journal of Modern Optics*, vol. 52, no. 2-3, pp. 285–304, 2005.

[81] N. Bozinovic, S. Golowich, P. Kristensen, and S. Ramachandran, "Control of orbital angular momentum of light with optical fibers," *Optics letters*, vol. 37, no. 13, pp. 2451–2453, 2012.

[82] A. M. Amaral, E. L. Falcão-Filho, and C. B. de Araújo, "Characterization of topological charge and orbital angular momentum of shaped optical vortices," *Optics express*, vol. 22, no. 24, pp. 30315–30324, 2014.

[83] T. Roger, J. J. Heitz, E. M. Wright, and D. Faccio, "Non-collinear interaction of photons with orbital angular momentum," *Scientific reports*, vol. 3, p. 3491, 2013.

[84] G. Molina-Terriza, J. P. Torres, and L. Torner, "Orbital angular momentum of photons in noncollinear parametric downconversion," *Optics Communications*, vol. 228, pp. 155–160, 2003.

[85] D. Persuy, M. Ziegler, O. Crégut, K. Kheng, M. Gallart, B. Hönerlage, and P. Gilliot, "Four-wave mixing in quantum wells using femtosecond pulses with laguerre-gauss modes," *Physical Review B*, vol. 92, no. 11, p. 115312, 2015.

[86] M. Zhi and A. V. Sokolov, "Broadband generation in a Raman crystal driven by a pair of time-delayed linearly chirped pulses," *New Journal of Physics*, vol. 10, p. 025032, feb 2008.

[87] R. Trebino, K. W. DeLong, D. N. Fittinghoff, J. N. Sweetser, M. A. Krumbügel, B. A. Richman, and D. J. Kane, "Measuring ultrashort laser pulses in the time-frequency domain using frequency-resolved optical gating," *Review of Scientific Instruments*, vol. 68, no. 9, pp. 3277–3295, 1997.

[88] R. L. Phillips and L. C. Andrews, "Spot size and divergence for Laguerre Gaussian beams of any order," *Applied Optics*, vol. 22, no. 5, pp. 643–644, 1983.

[89] S. G. Reddy, S. Prabhakar, A. Kumar, J. Banerji, and R. Singh, "Higher order optical vortices and formation of speckles," *Optics letters*, vol. 39, no. 15, pp. 4364–4367, 2014.

[90] H. Ma, H. Hu, W. Xie, and X. Xu, “Study on the generation of a vortex laser beam by using phase-only liquid crystal spatial light modulator,” *Optical Engineering*, vol. 52, no. 9, p. 091721, 2013.

[91] K. Bezuhanov, A. Dreischuh, G. G. Paulus, M. G. Schätzel, and H. Walther, “Vortices in femtosecond laser fields,” *Optics Letters*, vol. 29, no. 16, pp. 1942–1944, 2004.

[92] S. B. Cavalcanti, G. P. Agrawal, and M. Yu, “Noise amplification in dispersive nonlinear media,” *Physical Review A*, vol. 51, no. 5, pp. 4086–4092, 1995.

[93] M. S. Kirilenko and S. N. Khonina, “Information transmission using optical vortices,” *Optical Memory and Neural Networks*, vol. 22, no. 2, pp. 81–89, 2013.

[94] S. N. Khonina, N. L. Kazanskiy, and V. A. Soifer, “Optical Vortices in a Fiber : Mode Division Multiplexing and Multimode Self-Imaging,” *Recent Progress in Optical Fiber Research*, pp. 327–352, 2012.

[95] S. Berdagué and P. Facq, “Mode division multiplexing in optical fibers.,” *Applied Optics*, vol. 21, no. 11, pp. 1950–1955, 1982.

[96] K. T. Gahagan and G. A. Swartzlander, “Optical vortex trapping of particles,” *Optics Letters*, vol. 21, no. 11, pp. 827–829, 1996.

[97] M. Dienerowitz, M. Mazilu, and K. Dholakia, “Optical manipulation of nanoparticles: a review,” *Journal of Nanophotonics*, vol. 2, no. September, pp. 1–32, 2008.

[98] D. P. Ghai, S. Vyas, P. Senthilkumaran, and R. S. Sirohi, “Detection of phase singularity using a lateral shear interferometer,” *Optics and Lasers in Engineering*, vol. 46, no. 6, pp. 419–423, 2008.

[99] H. I. Sztul and R. R. Alfano, “Double-slit interference with Laguerre-Gaussian beams,” *Optics Letters*, vol. 31, no. 7, pp. 999–1001, 2006.

[100] A. G. White, C. P. Smith, N. R. Heckenberg, H. Rubinsztein-Dunlop, R. McDuff, C. O. Weiss, and C. Tamm, "Interferometric measurements of phase singularities in the output of a visible laser," *Journal of Modern Optics*, vol. 38, no. 12, pp. 2531–2541, 1991.

[101] L. Yongxin, T. Hua, P. Jixiong, and L. Baida, "Detecting the topological charge of vortex beams using an annular triangle aperture," *Optics and Laser Technology*, vol. 43, no. 7, pp. 1233–1236, 2011.

[102] S. N. Khonina, V. V. Kotlyar, V. a. Soifer, K. Jefimovs, P. Pääkkönen, and J. Turunen, "Astigmatic Bessel laser beams," *Journal of Modern Optics*, vol. 51, no. 5, pp. 677–686, 2004.

[103] V. V. Kotlyar, S. N. Khonina, A. a. Almazov, V. a. Soifer, K. Jefimovs, and J. Turunen, "Elliptic Laguerre-Gaussian beams.," *Journal of the Optical Society of America A, Optics, image science, and vision*, vol. 23, no. 1, pp. 43–56, 2006.

[104] A. A. Almazov, S. N. Khonina, and V. V. Kotlyar, "How the tilt of a phase diffraction optical element affects the properties of shaped laser beams matched with a basis of angular harmonics," *Journal of Optical Technology*, vol. 73, no. 9, pp. 633–639, 2006.

[105] M. W. Beijersbergen, L. Allen, H. E. L. O. van der Veen, and J. P. Woerdman, "Astigmatic laser mode converters and transfer of orbital angular momentum," *Optics Communications*, vol. 96, pp. 123–132, 1993.

[106] V. Denisenko, V. Shvedov, A. S. Desyatnikov, D. N. Neshev, W. Krolikowski, A. Volyar, M. Soskin, and Y. S. Kivshar, "Determination of topological charges of polychromatic optical vortices.," *Optics Express*, vol. 17, no. 26, pp. 23374–23379, 2009.

[107] T. R. Harvey and B. J. McMorran, "A Stern-Gerlach-like approach to electron orbital angular momentum measurement," *arXiv:1606.0361*, 2016.

[108] V. Jarutis, A. Matijošius, V. Smilgevičius, and A. Stabinis, "Second harmonic generation of higher-order Bessel beams," *Optics Communications*, vol. 185, no. 1-3, pp. 159–169, 2000.

[109] A. V. Gorbach and D. V. Skryabin, “Cascaded generation of multiply charged optical vortices and spatiotemporal helical beams in a Raman medium,” *Physical Review Letters*, vol. 98, no. 24, pp. 1–4, 2007.

[110] J. Strohaber, J. Abul, M. Richardson, F. Zhu, A. A. Kolomenskii, and H. A. Schuessler, “Cascade Raman sideband generation and orbital angular momentum relations for paraxial beam modes,” *Optics Express*, vol. 23, no. 17, p. 22463, 2015.

[111] P. Hansinger, G. Maleshkov, I. L. Garanovich, D. V. Skryabin, D. N. Neshev, A. Dreischuh, and G. G. Paulus, “White light generated by femtosecond optical vortex beams,” *Journal of the Optical Society of America B*, vol. 33, no. 4, pp. 681–690, 2016.

[112] A. Bekshaev, M. Soskin, and M. Vasnetsov, “Paraxial Light Beams with Angular Momentum,” *arXiv:0801.2309*, 2008.

[113] D. Rozas, C. Law, and G. Swartzlander, “Propagation dynamics of optical vortices,” *Journal of the Optical Society of America B*, vol. 17, no. 12, pp. 9818–27, 1997.

[114] S. Khonina and V. Kotlyar, “Generation and selection of laser beams represented by a superposition of two angular harmonics,” *Journal of Modern Optics*, vol. 51, no. 5, pp. 761–773, 2004.

[115] S. N. Khonina, V. V. Kotlyar, V. A. Soifer, P. Pääkkönen, J. Simonen, and J. Turunen, “An analysis of the angular momentum of a light field in terms of angular harmonics,” *Journal of Modern Optics*, vol. 48, no. 10, pp. 1543–1557, 2001.

[116] S. N. Khonina, V. V. Kotlyar, V. A. Soifer, P. Paakkonen, and J. Turunen, “Measuring the light field orbital angular momentum using DOE,” *Optical Memory and Neural Networks*, vol. 9, no. 4, pp. 241–255, 2001.

[117] V. V. Kotlyar, S. N. Khonina, and V. A. Soifer, “Light field decomposition in angular harmonics by means of diffractive optics,” *Journal of Modern Optics*, vol. 45, no. 7, pp. 1495–1506, 1998.

[118] J. Leach, M. Padgett, S. Barnett, S. Franke-Arnold, and J. Courtial, “Measuring the Orbital Angular Momentum of a Single Photon,” *Physical Review Letters*, vol. 88, no. 25, p. 257901, 2002.

[119] A. Y. Bekshaev, M. S. Soskin, and M. V. Vasnetsov, “Transformation of higher-order optical vortices upon focusing by an astigmatic lens,” *Optics Communications*, vol. 241, no. 4-6, pp. 237–247, 2004.

[120] R. S. Sirohi, *A course of experiments with He-Ne Laser.* New Age International, 1991.

[121] S. Baker, I. Walmsley, J. Tisch, and J. Marangos, “Femtosecond to attosecond light pulses from a molecular modulator,” *Nature Photonics*, vol. 5, no. 11, pp. 664–671, 2011.

[122] A. V. Sokolov, D. R. Walker, D. D. Yavuz, G. Y. Yin, and S. E. Harris, “Raman generation by phased and antiphased molecular states,” *Phys. Rev. Lett.*, vol. 85, pp. 562–565, Jul 2000.

[123] A. Zheltikov, “Spectroscopic and quantum-control aspects of ultrashort-pulse synthesis through impulsive high-order stimulated Raman scattering,” *Journal of Raman Spectroscopy*, vol. 33, no. 2, pp. 112–120, 2002.

[124] A. Abdolvand, A. Walser, M. Ziemienczuk, T. Nguyen, and P. S. J. Russell, “Generation of a phase-locked Raman frequency comb in gas-filled hollow-core photonic crystal fiber,” *Optics letters*, vol. 37, no. 21, pp. 4362–4364, 2012.

[125] H.-S. Chan, Z.-M. Hsieh, W.-H. Liang, A. Kung, C.-K. Lee, C.-J. Lai, R.-P. Pan, and L.-H. Peng, “Synthesis and measurement of ultrafast waveforms from five discrete optical harmonics,” *Science*, vol. 331, no. 6021, pp. 1165–1168, 2011.

[126] D. D. Yavuz, “Toward synthesis of arbitrary optical waveforms,” *Science*, vol. 331, no. 6021, pp. 1142–1143, 2011.

[127] S. T. Cundiff and A. M. Weiner, “Optical arbitrary waveform generation,” *Nature Photonics*, vol. 4, no. 11, pp. 760–766, 2010.

[128] M. Shapiro and P. Brumer, “Coherent control of molecular dynamics,” *Reports on Progress in Physics*, vol. 66, no. 6, p. 859, 2003.

[129] A. H. Zewail, “Femtochemistry: Atomic-scale dynamics of the chemical bond,” *The Journal of Physical Chemistry A*, vol. 104, no. 24, pp. 5660–5694, 2000.

[130] J. Zheng and M. Katsuragawa, “Freely designable optical frequency conversion in Raman-resonant four-wave-mixing process,” *Scientific reports*, vol. 5, 2015.

[131] C. Ohae, J. Zheng, K. Ito, M. Suzuki, K. Minoshima, and M. Katsuragawa, “Tailored raman-resonant four-wave-mixing processes,” *Optics Express*, vol. 26, no. 2, pp. 1452–1460, 2018.

[132] M. Zhi, X. Wang, and A. V. Sokolov, “Broadband light generation using a relatively weak raman mode in lead tungstate crystal,” *Journal of Modern Optics*, vol. 57, no. 19, pp. 1863–1866, 2010.

[133] J. Liu and T. Kobayashi, “Generation and amplification of tunable multicolored femtosecond laser pulses by using cascaded four-wave mixing in transparent bulk media,” *Sensors*, vol. 10, no. 5, pp. 4296–4341, 2010.

[134] H. Matsuki, K. Inoue, and E. Hanamura, “Multiple coherent anti-Stokes Raman scattering due to phonon grating in KNbO3 induced by crossed beams of two-color femtosecond pulses,” *Physical Review B*, vol. 75, no. 2, p. 024102, 2007.

[135] A. A. Zhdanova, M. Zhi, and A. V. Sokolov, “Coherent Raman generation in solid-state materials using spatial and temporal laser field shaping,” in *Frontiers and Advances in Molecular Spectroscopy*, pp. 395–420, Elsevier, 2018.

[136] N. H. Shon, F. Le Kien, K. Hakuta, and A. V. Sokolov, “Two-dimensional model for femtosecond pulse conversion and compression using high-order stimulated Raman scattering in solid hydrogen,” *Physical Review A*, vol. 65, no. 3, p. 033809, 2002.

[137] F. Le Kien, K. Hakuta, and A. V. Sokolov, “Pulse compression by parametric beating with a prepared Raman coherence,” *Physical Review A*, vol. 66, no. 2, p. 023813, 2002.

[138] M. Zhi, K. Wang, X. Hua, and A. V. Sokolov, "Pulse-shaper-assisted phase control of a coherent broadband spectrum of Raman sidebands," *Optics Letters*, vol. 36, p. 4032, oct 2011.

[139] K. Wang, M. Zhi, X. Hua, and A. V. Sokolov, "Ultrafast waveform synthesis and characterization using coherent Raman sidebands in a reflection scheme," *Optics Express*, vol. 22, no. 18, pp. 21411–21420, 2014.

[140] A. V. Sokolov, D. R. Walker, D. Yavuz, G. Yin, and S. Harris, "Femtosecond light source for phase-controlled multiphoton ionization," *Physical Review Letters*, vol. 87, no. 3, p. 033402, 2001.

[141] J. E. Krist, "Proper: an optical propagation library for idl," in *Optical Modeling and Performance Predictions III*, vol. 6675, p. 66750P, International Society for Optics and Photonics, 2007.

[142] A. Siegman, *Lasers*. University Science Books, 1986.

[143] R. Chipaux and M. Géléoc, "Optical anisotropy effects in lead tungstate crystals," tech. rep., DAPNIA, 1998.

[144] A. A. Kaminskii, H. J. Eichler, K. ichi Ueda, N. V. Klassen, B. S. Redkin, L. E. Li, J. Findeisen, D. Jaque, J. García-Sole, J. Fernández, and R. Balda, "Properties of Nd3 +/- doped and undoped tetragonal PbWO4, NaY(WO4)2, CaWO4, and undoped monoclinic ZnWO4 and CdWO4 as laser-active and stimulated Raman scattering-active crystals," *Appl. Opt.*, vol. 38, pp. 4533–4547, Jul 1999.

[145] R. Trebino, *Frequency-resolved optical gating: the measurement of ultrashort laser pulses*. Springer Science & Business Media, 2012.

[146] S. Akturk, M. Kimmel, P. O'Shea, and R. Trebino, "Measuring spatial chirp in ultrashort pulses using single-shot Frequency-Resolved Optical Gating.," *Optics Express*, vol. 11, no. 1, pp. 68–78, 2003.

[147] X. Gu, S. Akturk, and R. Trebino, "Spatial chirp in ultrafast optics," *Optics Communications*, vol. 242, no. 4-6, pp. 599–604, 2004.

[148] A. A. Zhdanova, A. Bahari, M. Shutova, and A. V. Sokolov, "Synthesis of ultrafast waveforms using coherent raman sidebands," *arXiv preprint arXiv:1901.11155*, 2019.

[149] J. Arlt and K. Dholakia, "Generation of high-order bessel beams by use of an axicon," *Optics Communications*, vol. 177, no. 1-6, pp. 297–301, 2000.

[150] J. Wang, "Advances in communications using optical vortices," *Photonics Research*, vol. 4, no. 5, pp. B14–B28, 2016.

[151] M. J. Padgett, "Orbital angular momentum 25 years on," *Optics Express*, vol. 25, no. 10, pp. 11265–11274, 2017.

[152] M. Padgett and R. Bowman, "Tweezers with a twist," *Nature Photonics*, vol. 5, no. 6, p. 343, 2011.

[153] A. Ashkin, J. M. Dziedzic, J. Bjorkholm, and S. Chu, "Observation of a single-beam gradient force optical trap for dielectric particles," *Optics letters*, vol. 11, no. 5, pp. 288–290, 1986.

[154] K. C. Neuman and S. M. Block, "Optical trapping," *Review of scientific instruments*, vol. 75, no. 9, pp. 2787–2809, 2004.

[155] W. Yu, Z. Ji, D. Dong, X. Yang, Y. Xiao, Q. Gong, P. Xi, and K. Shi, "Super-resolution deep imaging with hollow bessel beam sted microscopy," *Laser & Photonics Reviews*, vol. 10, no. 1, pp. 147–152, 2016.

[156] B. Hafizi, A. Ganguly, A. Ting, C. Moore, and P. Sprangle, "Analysis of gaussian beam and bessel beam driven laser accelerators," *Physical Review E*, vol. 60, no. 4, p. 4779, 1999.

[157] V. V. Korobkin, L. Y. Polonskiĭ, V. P. Poponin, and L. N. Pyatnitskiĭ, "Focusing of Gaussian and super-Gaussian laser beams by axicons to obtain continuous laser sparks," *Soviet Journal of Quantum Electronics*, vol. 16, no. 2, p. 178, 1986.

[158] C. Durfee III and H. Milchberg, "Light pipe for high intensity laser pulses," *Physical Review Letters*, vol. 71, no. 15, p. 2409, 1993.

[159] A. Morozov, A. Goltsov, Q. Chen, M. Scully, and S. Suckewer, "Ionization assisted self-guiding of femtosecond laser pulses," *Physics of Plasmas*, vol. 25, p. 053110, 5 2018.

[160] J. Vieira, R. Trines, E. Alves, R. Fonseca, J. Mendonça, R. Bingham, P. Norreys, and L. Silva, "High orbital angular momentum harmonic generation," *Physical review letters*, vol. 117, no. 26, p. 265001, 2016.

[161] L. Rego, J. San Román, A. Picón, L. Plaja, and C. Hernández-García, "Nonperturbative twist in the generation of extreme-ultraviolet vortex beams," *Physical review letters*, vol. 117, no. 16, p. 163202, 2016.

[162] N. A. Chaitanya, M. Jabir, J. Banerji, and G. K. Samanta, "Hollow gaussian beam generation through nonlinear interaction of photons with orbital angular momentum," *Scientific reports*, vol. 6, p. 32464, 2016.

[163] A. A. Zhdanova, M. Shutova, A. Bahari, M. Zhi, and A. V. Sokolov, "Topological charge algebra of optical vortices in nonlinear interactions," *Optics express*, vol. 23, no. 26, pp. 34109–34117, 2015.

[164] T. Pezeril, G. Saini, D. Veysset, S. Kooi, P. Fidkowski, R. Radovitzky, and K. A. Nelson, "Direct visualization of laser-driven focusing shock waves," *Physical review letters*, vol. 106, no. 21, p. 214503, 2011.

[165] N. E. Andreev, S. S. Bychkov, V. V. Kotlyar, L. Y. Margolin, L. N. Pyatnitskii, and P. Serafimovich, "Formation of high-power hollow bessel light beams," *Quantum Electronics*, vol. 26, no. 2, pp. 126–130, 1996.

[166] K. Gahagan and G. Swartzlander, "Optical vortex trapping of particles," *Optics letters*, vol. 21, no. 11, pp. 827–829, 1996.

[167] R. Bowman, N. Muller, X. Zambrana-Puyalto, O. Jedrkiewicz, P. Di Trapani, and M. Padgett, “Efficient generation of bessel beam arrays by means of an slm,” *The European Physical Journal Special Topics*, vol. 199, no. 1, pp. 159–166, 2011.

[168] S. Oemrawsingh, J. Van Houwelingen, E. Eliel, J. Woerdman, E. Verstegen, J. Kloosterboer, *et al.*, “Production and characterization of spiral phase plates for optical wavelengths,” *Applied optics*, vol. 43, no. 3, pp. 688–694, 2004.

[169] J. Fan, E. Parra, I. Alexeev, K. Kim, H. Milchberg, L. Y. Margolin, and L. Pyatnitskii, “Tubular plasma generation with a high-power hollow bessel beam,” *Physical Review E*, vol. 62, no. 6, p. R7603, 2000.

[170] S. Franke-Arnold, J. Leach, M. J. Padgett, V. E. Lembessis, D. Ellinas, A. J. Wright, J. M. Girkin, P. Öhberg, and A. S. Arnold, “Optical ferris wheel for ultracold atoms,” *Optics Express*, vol. 15, no. 14, pp. 8619–8625, 2007.

[171] A. Sabatyan and J. Rafighdoost, “Azimuthal phase-shifted zone plates to produce petal-like beams and ring lattice structures,” *JOSA B*, vol. 34, no. 5, pp. 919–923, 2017.

[172] P. García-Martínez, M. M. Sánchez-López, J. A. Davis, D. M. Cottrell, D. Sand, and I. Moreno, “Generation of bessel beam arrays through dammann gratings,” *Applied optics*, vol. 51, no. 9, pp. 1375–1381, 2012.

[173] A. Vasara, J. Turunen, and A. T. Friberg, “Realization of general nondiffracting beams with computer-generated holograms,” *JOSA A*, vol. 6, no. 11, pp. 1748–1754, 1989.

[174] R. Herman and T. Wiggins, “Production and uses of diffractionless beams,” *Journal of the Optical Society of America A*, vol. 8, no. 6, pp. 932–942, 1991.

[175] C. H. Schmitz, K. Uhrig, J. P. Spatz, and J. E. Curtis, “Tuning the orbital angular momentum in optical vortex beams,” *Optics express*, vol. 14, no. 15, pp. 6604–6612, 2006.

[176] S. Khonina, V. Kotlyar, V. Soifer, K. Jefimovs, P. Pääkkönen, and J. Turunen, “Astigmatic Bessel laser beams,” *Journal of Modern Optics*, vol. 51, no. 5, pp. 677–686, 2004.

[177] S. Hayashi, "SERS on random rough silver surfaces: evidence of surface plasmon excitation and the enhancement factor for copper phthalocyanine," *Surface Science*, vol. 158, no. 1-3, pp. 229–237, 1985.

[178] G. McNay, D. Eustace, W. E. Smith, K. Faulds, and D. Graham, "Surface-enhanced Raman scattering (SERS) and surface-enhanced resonance Raman scattering (SERRS): a review of applications," *Applied Spectroscopy*, vol. 65, no. 8, pp. 825–837, 2011.

[179] R. Dornhaus, R. E. Benner, R. K. Chang, and I. Chabay, "Surface plasmon contribution to SERS," *Surface Science*, vol. 101, no. 1-3, pp. 367–373, 1980.

[180] A. D. Shutov, Z. Yi, J. Wang, A. M. Sinyukov, Z. He, C. Tang, J. Chen, E. J. Ocola, J. Laane, A. V. Sokolov, *et al.*, "Giant chemical surface enhancement of coherent raman scattering on MoS2," *ACS Photonics*, vol. 5, no. 12, pp. 4960–4968, 2018.

[181] X. Hua, D. V. Voronine, C. W. Ballmann, A. M. Sinyukov, A. V. Sokolov, and M. O. Scully, "Nature of surface-enhanced coherent Raman scattering," *Phys. Rev. A*, vol. 89, no. 4, p. 043841, 2014.

[182] D. Cialla, A. März, R. Böhme, F. Theil, K. Weber, M. Schmitt, and J. Popp, "Surface-enhanced Raman spectroscopy (SERS): progress and trends," *Analytical and Bioanalytical Chemistry*, vol. 403, no. 1, pp. 27–54, 2012.

[183] E. Le Ru and P. Etchegoin, "Rigorous justification of the |E|4 enhancement factor in surface enhanced Raman spectroscopy," *Chemical Physics Letters*, vol. 423, no. 1-3, pp. 63–66, 2006.

[184] G. Mie, "Articles on the optical characteristics of turbid tubes, especially colloidal metal solutions," *Ann. Phys*, vol. 25, no. 3, pp. 377–445, 1908.

[185] R. G. Freeman, K. C. Grabar, K. J. Allison, R. M. Bright, J. A. Davis, A. P. Guthrie, M. B. Hommer, M. A. Jackson, P. C. Smith, D. G. Walter, *et al.*, "Self-assembled metal colloid monolayers: an approach to SERS substrates," *Science*, vol. 267, no. 5204, pp. 1629–1632, 1995.

[186] V. P. Drachev, M. D. Thoreson, V. Nashine, E. N. Khaliullin, D. Ben-Amotz, V. J. Davisson, and V. M. Shalaev, “Adaptive silver films for surface-enhanced Raman spectroscopy of biomolecules,” *Journal of Raman Spectroscopy: An International Journal for Original Work in all Aspects of Raman Spectroscopy, Including Higher Order Processes, and also Brillouin and Rayleigh Scattering*, vol. 36, no. 6-7, pp. 648–656, 2005.

[187] C. R. Yonzon, C. L. Haynes, X. Zhang, J. T. Walsh, and R. P. Van Duyne, “A glucose biosensor based on surface-enhanced raman scattering: improved partition layer, temporal stability, reversibility, and resistance to serum protein interference,” *Analytical Chemistry*, vol. 76, no. 1, pp. 78–85, 2004.

[188] Z. He, D. V. Voronine, A. M. Sinyukov, Z. N. Liege, B. Birmingham, A. V. Sokolov, Z. Zhang, and M. O. Scully, “Tip-enhanced raman scattering on bulk mos 2 substrate,” *IEEE Journal of Selected Topics in Quantum Electronics*, vol. 23, no. 2, pp. 113–118, 2016.

[189] Z. He, Z. Han, M. Kizer, R. J. Linhardt, X. Wang, A. M. Sinyukov, J. Wang, V. Deckert, A. V. Sokolov, J. Hu, and M. O. Scully, “Tip-enhanced raman imaging of single-stranded dna with single base resolution,” *Journal of the American Chemical Society*, vol. 141, no. 2, pp. 753–757, 2018.

[190] M. Shutova, A. D. Shutov, A. A. Zhdanova, J. V. Thompson, and A. V. Sokolov, “Coherent Raman generation controlled by wavefront shaping,” *Scientific Reports*, vol. 9, 2019.

[191] Y.-X. Ren, R.-D. Lu, and L. Gong, “Tailoring light with a digital micromirror device,” *Annalen Der Physik*, vol. 527, no. 7-8, pp. 447–470, 2015.

[192] A. A. Baker, M. J. Miles, and W. Helbert, “Internal structure of the starch granule revealed by AFM,” *Carbohydrate Research*, vol. 330, no. 2, pp. 249–256, 2001.

[193] W. E. Moerner, “Nobel lecture: Single-molecule spectroscopy, imaging, and photocontrol: Foundations for super-resolution microscopy,” *Reviews of Modern Physics*, vol. 87, pp. 1183–1212, 2015.

[194] J. N. Anker, W. P. Hall, O. Lyandres, N. C. Shah, J. Zhao, and R. P. Van Duyne, "Biosensing with plasmonic nanosensors," *Nature materials*, vol. 7, no. 6, p. 442, 2008.

[195] A. G. Brolo, "Plasmonics for future biosensors," *Nature Photonics*, vol. 6, no. 11, p. 709, 2012.

[196] A. Gopinath, S. V. Boriskina, B. M. Reinhard, and L. Dal Negro, "Deterministic aperiodic arrays of metal nanoparticles for surface-enhanced raman scattering (sers)," *Optics Express*, vol. 17, no. 5, pp. 3741–3753, 2009.

[197] S. Gwo, C.-Y. Wang, H.-Y. Chen, M.-H. Lin, L. Sun, X. Li, W.-L. Chen, Y.-M. Chang, and H. Ahn, "Plasmonic metasurfaces for nonlinear optics and quantitative sers," *Acs Photonics*, vol. 3, no. 8, pp. 1371–1384, 2016.

[198] D. V. Voronine, A. M. Sinyukov, X. Hua, K. Wang, P. K. Jha, E. Munusamy, S. E. Wheeler, G. Welch, A. V. Sokolov, and M. O. Scully, "Time-resolved surface-enhanced coherent sensing of nanoscale molecular complexes," *Scientific reports*, vol. 2, p. 891, 2012.

[199] V. Giannini, A. I. Fernández-Domínguez, S. C. Heck, and S. A. Maier, "Plasmonic nanoantennas: fundamentals and their use in controlling the radiative properties of nanoemitters," *Chemical reviews*, vol. 111, no. 6, pp. 3888–3912, 2011.

[200] L. A. Giannuzzi, *Introduction to focused ion beams: instrumentation, theory, techniques and practice*. Springer Science & Business Media, 2004.

[201] Y. Tang and A. E. Cohen, "Optical chirality and its interaction with matter," *Physical review letters*, vol. 104, no. 16, p. 163901, 2010.

[202] A. Alexandrescu, D. Cojoc, and E. Di Fabrizio, "Mechanism of angular momentum exchange between molecules and laguerre-gaussian beams," *Physical review letters*, vol. 96, no. 24, p. 243001, 2006.

[203] P. Hemmer and C. Gomes, "Single proteins under a diamond spotlight," *Science*, vol. 347, no. 6226, pp. 1072–1073, 2015.

[204] P. Hemmer, "Toward molecular-scale mri," *Science*, vol. 339, no. 6119, pp. 529–530, 2013.

[205] L. Wildling, B. Unterauer, R. Zhu, A. Rupprecht, T. Haselgrubler, C. Rankl, A. Ebner, D. Vater, P. Pollheimer, E. E. Pohl, *et al.*, "Linking of sensor molecules with amino groups to amino-functionalized afm tips," *Bioconjugate chemistry*, vol. 22, no. 6, pp. 1239–1248, 2011.

[206] M. Kasperczyk, S. Person, D. Ananias, L. D. Carlos, and L. Novotny, "Excitation of magnetic dipole transitions at optical frequencies," *Physical review letters*, vol. 114, no. 16, p. 163903, 2015.

[207] J. K. Joung and J. D. Sander, "Talens: a widely applicable technology for targeted genome editing," *Nature reviews Molecular cell biology*, vol. 14, no. 1, p. 49, 2013.

[208] L. Novotny and N. Van Hulst, "Antennas for light," *Nature Photonics*, vol. 5, no. 2, p. 83, 2011.

[209] J. A. Schuller, E. S. Barnard, W. Cai, Y. C. Jun, J. S. White, and M. L. Brongersma, "Plasmonics for extreme light concentration and manipulation," *Nature Materials*, vol. 9, no. 3, p. 193, 2010.

[210] A. Kern and O. J. Martin, "Strong enhancement of forbidden atomic transitions using plasmonic nanostructures," *Physical Review A*, vol. 85, no. 2, p. 022501, 2012.

[211] R. Schirhagl, K. Chang, M. Loretz, and C. L. Degen, "Nitrogen-vacancy centers in diamond: nanoscale sensors for physics and biology," *Annual review of physical chemistry*, vol. 65, pp. 83–105, 2014.

[212] S. Tsesses, E. Ostrovsky, K. Cohen, B. Gjonaj, N. Lindner, and G. Bartal, "Optical skyrmion lattice in evanescent electromagnetic fields," *Science*, vol. 361, no. 6406, pp. 993–996, 2018.

[213] N. Yu and F. Capasso, "Flat optics with designer metasurfaces," *Nature materials*, vol. 13, no. 2, p. 139, 2014.

[214] E. Le Ru and P. Etchegoin, *Principles of Surface-Enhanced Raman Spectroscopy: and related plasmonic effects*. Elsevier, 2008.

[215] A. Bhattarai and P. Z. El-Khoury, "Imaging localized electric fields with nanometer precision through tip-enhanced raman scattering," *Chemical Communications*, vol. 53, no. 53, pp. 7310–7313, 2017.

[216] A. M. Alajlan, D. V. Voronine, A. M. Sinyukov, Z. Zhang, A. V. Sokolov, and M. O. Scully, "Gap-mode enhancement on mos2 probed by functionalized tip-enhanced raman spectroscopy," *Applied Physics Letters*, vol. 109, no. 13, p. 133106, 2016.

[217] E. Betzig, A. Lewis, A. Harootunian, M. Isaacson, and E. Kratschmer, "Near field scanning optical microscopy (nsom): development and biophysical applications," *Biophysical journal*, vol. 49, no. 1, pp. 269–279, 1986.

[218] E. Betzig, G. H. Patterson, R. Sougrat, O. W. Lindwasser, S. Olenych, J. S. Bonifacino, M. W. Davidson, J. Lippincott-Schwartz, and H. F. Hess, "Imaging intracellular fluorescent proteins at nanometer resolution," *Science*, vol. 313, no. 5793, pp. 1642–1645, 2006.

[219] H. Fu and A. Zunger, "Inp quantum dots: Electronic structure, surface effects, and the redshifted emission," *Physical Review B*, vol. 56, no. 3, p. 1496, 1997.

[220] M. Cotrufo and A. Fiore, "Spontaneous emission from dipole-forbidden transitions in semiconductor quantum dots," *Physical Review B*, vol. 92, no. 12, p. 125302, 2015.

[221] T. Kawazoe, K. Kobayashi, J. Lim, Y. Narita, and M. Ohtsu, "Direct observation of optically forbidden energy transfer between cucl quantum cubes via near-field optical spectroscopy," *Physical review letters*, vol. 88, no. 6, p. 067404, 2002.

[222] H. Mamin, M. Kim, M. Sherwood, C. Rettner, K. Ohno, D. Awschalom, and D. Rugar, "Nanoscale nuclear magnetic resonance with a nitrogen-vacancy spin sensor," *Science*, vol. 339, no. 6119, pp. 557–560, 2013.

[223] F. Shi, Q. Zhang, P. Wang, H. Sun, J. Wang, X. Rong, M. Chen, C. Ju, F. Reinhard, H. Chen, J. Wrachtrup, J. Wang, and J. Du, “Single-protein spin resonance spectroscopy under ambient conditions,” *Science*, vol. 347, no. 6226, pp. 1135–1138, 2015.

[224] L. Schlipf, T. Oeckinghaus, K. Xu, D. B. R. Dasari, A. Zappe, F. F. De Oliveira, B. Kern, M. Azarkh, M. Drescher, M. Ternes, K. Kern, J. Wrachtrup, and A. Finkler, “A molecular quantum spin network controlled by a single qubit,” *Science advances*, vol. 3, no. 8, p. e1701116, 2017.

[225] M. Alkahtani, J. Lang, B. Naydenov, F. Jelezko, and P. Hemmer, “Growth of high-purity low-strain fluorescent nanodiamonds,” *ACS Photonics*, vol. 6, no. 5, pp. 1266–1271, 2019.

[226] A. Ebner, L. Wildling, R. Zhu, C. Rankl, T. Haselgrübler, P. Hinterdorfer, and H. J. Gruber, “Functionalization of probe tips and supports for single-molecule recognition force microscopy,” in *STM and AFM Studies on (Bio) Molecular Systems: Unravelling the Nanoworld*, pp. 29–76, Springer, 2008.

[227] A. Ebner, P. Hinterdorfer, and H. J. Gruber, “Comparison of different aminofunctionalization strategies for attachment of single antibodies to afm cantilevers,” *Ultramicroscopy*, vol. 107, no. 10-11, pp. 922–927, 2007.

[228] A. J. Storm, C. Storm, J. Chen, H. Zandbergen, J.-F. Joanny, and C. Dekker, “Fast dna translocation through a solid-state nanopore,” *Nano letters*, vol. 5, no. 7, pp. 1193–1197, 2005.

[229] G. H. Seong, T. Niimi, Y. Yanagida, E. Kobatake, and M. Aizawa, “Single-molecular afm probing of specific dna sequencing using reca-promoted homologous pairing and strand exchange,” *Analytical chemistry*, vol. 72, no. 6, pp. 1288–1293, 2000.

[230] C. J. Addison and A. G. Brolo, “Nanoparticle-containing structures as a substrate for surface-enhanced raman scattering,” *Langmuir*, vol. 22, no. 21, pp. 8696–8702, 2006.

APPENDIX A

SIMULATION OF VARIOUS OAM MIXED STATES WITH TILTED LENS TECHNIQUE (MATLAB REALIZATION)

```
%__________________________lens is present________________%
k = 2*pi/0.000006328; % wavevector
z0 = 0; I = 1i; e = 1;  %equation parameters
z =0.20;            % parameter (distance from waist)
f = 0.2;             % parameter (focal distance)
teta = 0.1;          % parameter (tilting angle)
[x2,y2] = meshgrid(-0.00035:.000001:0.00035,
-0.00035:.000001:0.00035);
c1 = sec(teta);     c2 = cos(teta);
a1 = 1 - z*c1/f;    a2 = 1 - z*c2/f;
d1 = 1 - z0*c1/f;   d2 = 1 - z0*c2/f;
b1 = z0 + z*d1;     b2 = z0 + z*d2;
w1 = sqrt(1/(1/(0.009^2)+1i*k*a1/2/b1));
w2 = sqrt(1/(1/(0.009^2)+1i*k*a2/2/b2));
alfa1 = k*w1^2/2/b1;    beta1 = (k*w1/2/b1)^2 +I*k*d1/2/b1;
alfa2 = k*w2^2/2/b2;    beta2 = (k*w2/2/b2)^2 + I*k*d2/2/b2;
gama = sqrt(w1^2 - w2^2);
A0 = (k*w1*w2*((1i/2)^1))/((b1*b2)^(1/2));
A1 = (k*w1*w2*((1i/2)^2))/((b1*b2)^(1/2));
A2 = (k*w1*w2*((1i/2)^3))/((b1*b2)^(1/2));
A3 = (k*w1*w2*((1i/2)^4))/((b1*b2)^(1/2));
A4 = (k*w1*w2*((1i/2)^5))/((b1*b2)^(1/2));
```

```
herm = (alfa1*x2 + 1i*e*alfa2*y2)/gama;
%_____________________COMPLEX AMPLITUDES _________________%
Field0 = (A0*exp(-beta1*x2.^2 - beta2*y2.^2)
*gama^0).*(1);
Field1 = (A1*exp(-beta1*x2.^2 - beta2*y2.^2)
*gama^1).*(2*herm);
Field2 = (A2*exp(-beta1*x2.^2 - beta2*y2.^2)
*gama^2).*(4*herm.^2 - 2);
Field3 = (A3*exp(-beta1*x2.^2 - beta2*y2.^2)
*gama^3).*(8*herm.^3 -
12*herm);
Field4 = (A4*exp(-beta1*x2.^2 - beta2*y2.^2)
*gama^4).*(16*herm.^4 -
48*herm.^2 + 12);
%_________________________lens is absent_________________%
z =0.20;            % parameter (distance from waist)
teta = 0.01;          % parameter (tilting angle)
c1 = sec(teta);     c2 = cos(teta);
a1 = 1 - z*c1/f;    a2 = 1 - z*c2/f;
d1 = 1 - z0*c1/f;   d2 = 1 - z0*c2/f;
b1 = z0 + z*d1;     b2 = z0 + z*d2;
w1 = sqrt(1/(1/(0.009^2)+1i*k*a1/2/b1));
w2 = sqrt(1/(1/(0.009^2)+1i*k*a2/2/b2));
alfa1 = k*w1^2/2/b1;    beta1 = (k*w1/2/b1)^2
+I*k*d1/2/b1;
alfa2 = k*w2^2/2/b2;    beta2 = (k*w2/2/b2)^2
+ I*k*d2/2/b2;
```

```
gama = sqrt(w1^2 - w2^2);

A0 = (k*w1*w2*((1i/2)^1))/((b1*b2)^(1/2));

A1 = (k*w1*w2*((1i/2)^2))/((b1*b2)^(1/2));

A2 = (k*w1*w2*((1i/2)^3))/((b1*b2)^(1/2));

A3 = (k*w1*w2*((1i/2)^4))/((b1*b2)^(1/2));

A4 = (k*w1*w2*((1i/2)^5))/((b1*b2)^(1/2));

herm = (alfa1*x2 + 1i*e*alfa2*y2)/gama;

%____________________COMPLEX AMPLITUDES __________________%

Field0abs = (A0*exp(-beta1*x2.^2 - beta2*y2.^2)

*gama^0).*(1);

Field1abs = (A1*exp(-beta1*x2.^2 - beta2*y2.^2)

*gama^1).*(2*herm);

Field2abs = (A2*exp(-beta1*x2.^2 - beta2*y2.^2)

*gama^2).*

(4*herm.^2 - 2);

Field3abs = (A3*exp(-beta1*x2.^2 - beta2*y2.^2)

*gama^3).*

(8*herm.^3 - 12*herm);

Field4abs = (A4*exp(-beta1*x2.^2 - beta2*y2.^2)

*gama^4).*(16*herm.^4 - 48*herm.^2 + 12);

%__________________________*.GIF GRAPH________________%

figure

filename2 = '3+4coh+incoh_lens_contour.gif';

[n1] = linspace(1,251,251);

[Q] = linspace(0,0,251);

for NUM = 0:0.1:1

Z = abs(NUM*Field4/abs(max(Field4(:)))).^2
```

```
+abs((1-NUM)*Field3/
abs(max(Field3(:)))).^2;
%Z = abs(NUM*Field4/abs(max(Field4(:)))
+(1-NUM)*Field3/
abs(max(Field3(:)))).^2;
Z = Z(226:476,226:476);
    for i = 0:250
    Q(i+1) = Z((i+1), (i+1));
    end
M = max(Q);
Q = Q./M;
plot(n1,Q);
xlim([0 250]);
ylim([0 1]);
set(gca,'xtick',[])
set(gca,'ytick',[0 0.2 0.4 0.6 0.8 1])
ylabel('Relative intensity')
xlabel('x=y transverse coordinate')
str = sprintf('Incoherent add. %0.1f LG_0_3 +
%0.1f LG_0_4',(1-NUM),NUM);
title(str);
xlim([0 250]);
drawnow
frame = getframe(1);
im = frame2im(frame);
[C,map] = rgb2ind(im,256);
if NUM == 0;
```

```
imwrite(C,map,filename2,'gif','LoopCount'
,Inf,'DelayTime',1);
else
imwrite(C,map,filename2,'gif','WriteMode',
'append','DelayTime',1);
end
end
%________________________CONTOUR PLOT________________%
figure;
[n] = linspace(1,251,251);
[Q] = linspace(0,0,251);
NUM = 0;
Z = (abs(Field4/abs(max(Field4(:)))).^2);
% Z = abs(NUM*Field0/abs(max(Field0(:)))).^2
+abs((1-NUM)*Field1/
abs(max(Field1(:)))).^2;
% Z = abs(NUM*Field0/abs(max(Field0(:)))+(1-NUM)*Field1/
abs(max(Field1(:)))).^2;
Z = Z(226:476,226:476);
    for i = 0:250
    Q(i+1) = Z((i+1), (i+1));
    end
M = max(Q);
Q = Q./M;
plot(n,Q, 'LineWidth',2);
xlim([0 250]); set(gca,'xtick',[]); set(gca,'ytick',[]);
str = sprintf('Pure LG_0_4'); title(str);
```

```
%_______________________ 2D map view_______________________%
figure;
NUM = 0.5;
% Z1 = abs(NUM*Field0abs/abs(max(Field0abs(:)))).^2
+abs((1-NUM)*
Field1abs/abs(max(Field1abs(:)))).^2;
 Z1 = abs(NUM*Field2abs/abs(max(Field2abs(:)))+(1-NUM)
 *Field3abs/
 abs(max(Field3abs(:)))).^2;
 surf(Z1,'EdgeColor','None');
view(2);
xlim([100 600]); ylim([100 600])
```

APPENDIX B

GENERATING LCOS SLM PHASE MASKS FOR OVS (MATLAB REALIZATION)

```
%-------------READ ME---------------------
% this program generates the BMP file with the OV phase-mask
%for SLM Hamamatsu. It has a flexibility to change depth of
%modulation, ranndomly %move the center of OV (singularity
%point)
%and rotate the %pahase mask. Moreover the program can cat
%the rechtangular pieces from generated mask.
% INSTRUCTIONS
% adjust PARAMETERS below
%(read the comments in the PARAMETERS section)
% press "run" button
% mask.bmp file will be saved to the file path that you
%put under the function "strcat"
(you can upload it into SLM software when it is generated)
% profit
dim1 = 300; %600 SLM Hamamatsu resolution
dim2 = 396; %792 SLM Hamamatsu resolution
param1 = 112; % number of pixels to move the singularity point
param2 = 110; % number of pixels to move the singularity point
angle = 0; % angle of rotation
x1=0; y1=0; x2=600; y2=792; %cutting square coordinate points
initial_mask = ones(2*dim1+param1, 2*dim2+param2);
% initializes the matrix that becomes the bitmap.
```

```
coef1 = 3;  % SLM depth coeff
coef2 = 8;  % SLM depth coeff
for i=1:dim2
    for j=1:dim1
        initial_mask(j, i) = −atan((i-dim2)/(j−dim1));
    end
    for j=dim1:2*dim1
        initial_mask(j, i) = −atan((i-dim2)/(j−dim1))+pi;
    end
end
for i=dim2+1:2*dim2
   for j=1:dim1
      initial_mask(j, i) = −atan((i-dim2)/(j−dim1));
   end
   for j=dim1:2*dim1
      initial_mask(j, i) = −atan((i-dim2)/(j−dim1))+pi;
   end
end
modulated_mask = (initial_mask+coef1)/coef2;
modulated_mask = imrotate(modulated_mask,angle);
modulated_mask = imcrop(modulated_mask,[x1 y1 x2 y2]);
full_filename = strcat('C:\ADDRESS\', num2str(param1),
'-', num2str(param2),'_', num2str(x1), 'x',num2str(y1),'_',
num2str(x2),'x', num2str(y2),'.bmp');
imwrite(modulated_mask, full_filename);
```

APPENDIX C

GENERATING LCOS SLM PHASE MASKS BINARY PHASE PLATES (MATLAB REALIZATION)

```
%-------------READ ME---------------------
% this program generates the BMP file with the custom
phase-mask for SLM Hamamatsu
% INSTRUCTIONS
% add current folder to path in MATLAB!!! this is important for
saving mask_N.bmp file
% adjust PARAMETERS below
(read the comments in the PARAMETERS section)
% press "run" button
% mask_N.bmp file will be saved to the current folder
(you can upload it into SLM software when it is generated)
% profit
%------------ PARAMETERS------------------
N = 40;
% the number of sectors divided by 2. the total
%number of sectors is 2*N
depth_black = 0;
% modulation depth of zero phase sectors.
%Range: 0 < depth_black < 1
depth_white = 0.5;
% modulation depth of Pi phase sectors
%Range: 0 < depth_white < 1
```

```
% FOR depth_black and depth_white:
% 0   gives 0    phase addition
% 0.5 gives Pi   phase addition
% 1   gives 2*Pi phase addition
% scales linearly
%------------ CODE------------------
phase_mask = zeros(600, 792);
% initialize the matrix that becomes the bitmap.
for i=1:396,
    for j=1:300,
        phase_mask(j, i) = -atan((i-396)/(j-300));
    end
    for j=300:600,
        phase_mask(j, i) = -atan((i-396)/(j-300))+pi;
    end
end
for i=397:792,
   for j=1:300,
      phase_mask(j, i) = -atan((i-396)/(j-300));
   end
   for j=300:600,
      phase_mask(j, i) = -atan((i-396)/(j-300))+pi;
   end
end
figure         % show each new mask as a separate figure
image_map = imagesc(phase_mask);
% image of the mask on the screen
```

```
map = [depth_black, depth_black, depth_black;
%custom  colormap
depth_white, depth_white, depth_white];
mapN = repmat(map,N,1);
colormap(mapN);
fmt = ’.bmp’;
% saved file format
full_filename = sprintf(’mask_N=%d%s’ ,2*N, fmt);
% filename
set(gca,’XTick’,[])
% remove the ticks in the x axis
set(gca,’YTick’,[])
% remove the ticks in the y axis
set(gca,’Position’,[0 0 1 1])
% rake the axes occupy the hole figure
r = 250;
% set bmp file resolution
set(gcf, ’PaperUnits’, ’inches’, ’PaperPosition’,
[0 0 1320 1000]/r);
print(full_filename, gcf, ’-dbmp’);
% save bmp file into the current path folder
```

APPENDIX D

CHEMICAL SYNTHESIS OF GOLD NANOPARTICLES

Random rough gold surfaces can be easily synthesized without much efforts and expenses [230]. For this, we need, firstly, to synthesize gold nanoparticles (NP), secondly, prepare glass sybstrates for NP deposition, and finally, glue NP to glass and make sure they aggregate. All glassware used for this needs to be thoroughly cleaned with the procedure, described, for instance, in Ref. [230]. Here we present chemical algorithm to synthesize NPs:

- Boil with stirring 500mL of 1mM solution of $HAuCl_4$ (available from Sigma-Aldrich), Fig. D.1a;
- add 50mL of 38.8 mM of sodium citrate and continue heating and stirring for 10 more minutes, Fig. D.1b;
- stop heating and continue stirring for 15 more minutes;
- keep in refrigerator up to 1 year.

After synthesis, we need to create golf NPs aggregations on the glass surface, for this:

- cut glass slides onto small pieces that fits under the microscope or AFM; clean them in with 95% ehtanol (10 minutes), deionized water (10 minutes), piranha solution (10 minutes); rinse with water and MeOH;
- put clean glass slides into the MPTMS solution (5% v/v MPTMS in MeOH), leave for 12 hours;
- remove slides from MPTMS solution and rinse with MeOH and water;
- put glass slides into the a solution of gold NPs and leave for 24 hours Fig. D.1c;

- remove glass slides from NP solution and rinse with water Fig. D.1d.

Figure D.1 shows the process of gold NP synthesis and gluing on the glass. By following the above description, 10nm size particles can be generated. As a result we get NP aggregations, that will give us many hot spots for SERS measurements. A new layer of gold NPs can be added on top of the previous one, if needed, following the procedure from Ref. [230].

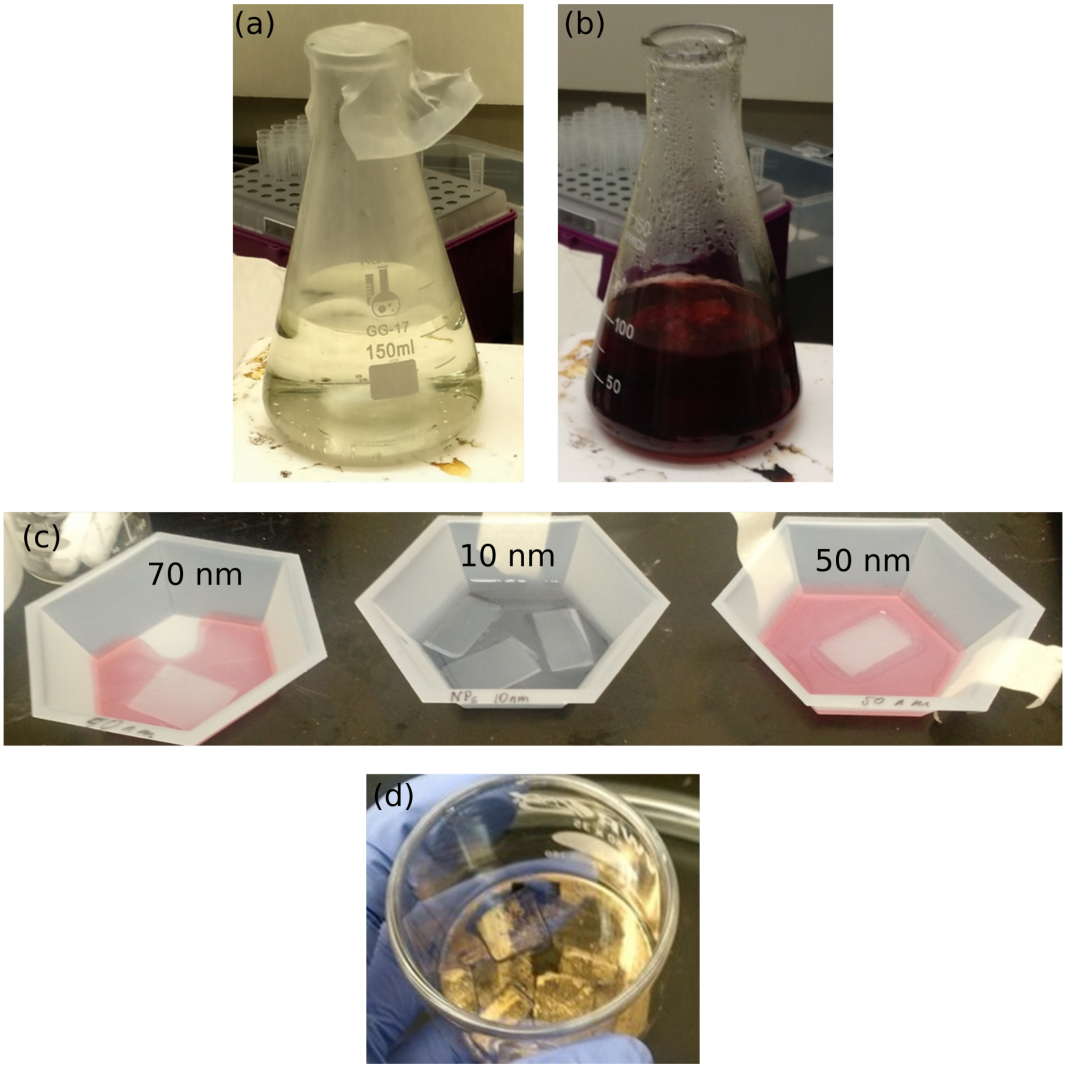

Figure D.1: Process of synthesising gold NPs. **(a):** heated 1mM solution of HAuCl$_4$ (sligtly yellow in color. **(a):** fresh synthesized solution of 10nm NPs. **(c):**derivatized glass sildes, soaked in NPs solutions of different sized. Numbers in the picture show the size of NPs. The NPs synthesized in (a) and (b) are in the middle. **(d):** resultant rought gold nanosurfaces.